MEMORIAL
UNIVERSITY

Autonomous real-time infrared detection of sub-surface vessels for unmanned aircraft systems

by

© **Jordan Peckham**

A thesis submitted to the School of Graduate
Studies in partial fulfillment of the requirements for
the degree of

Doctor of Philosophy

Faculty of Engineering & Applied Science

Memorial University

May 2019

St. John's, Newfoundland and Labrador, Canada

Abstract

The threat of small self-propelled semi-submersible vessels cannot be understated; payloads from drugs to weapons of mass destruction could be housed in these small, inconspicuous vessels. With a current apprehension rate of approximately 10%, a method resulting in increased interdiction of this illegal traffic is required for national security both in the ports along the coastlines of Canada, as well as the rest of North America. A smart, autonomous payload containing an infrared imaging device, designed for use in small unmanned aircraft systems for the specific mission of detecting self-propelled semi-submersibles over the vast ocean coastline will address the current security needs.

Thermal imagery of the disturbed colder water layers, driven to the surface by the vessel will allow for the detection of this traffic using long wave infrared technology. Infrared signatures of ship wakes are highly variable in both persistence and temperature contrast as compared to the surrounding surface water, thus infrared imaging devices with a high resolution, a high responsivity, and a very low minimum resolvable temperature will be required to provide high quality imagery for airborne detection of the thermal wake.

A theoretical understanding of the physics associated with the energy collected by the infrared sensor and the resulting infrared images is provided. Explanation of the factors affecting the resulting image with respect to the camera properties are detailed. A variety of examples of airborne thermal images are presented, with detailed explanations of the imaged scenes based on theory and sensor characteristics provided in the previous sections.

Infrared images taken over the Atlantic and Pacific oceans from manned and unmanned aircraft platforms are presented. Temperature measurements taken using Vemco Minilog II temperature loggers confirmed the thermal stratification of the upper 5 meters of the water. Thermal scarring due to upwelled colder water to the

surface was noted during the day time under normal conditions, with temperature differences found to be consistent with the measured temperature profile. A custom gimbal system, with corresponding ground control station for real-time, visual feedback is presented.

An algorithm for the detection of submerged vessel ship wakes using a LWIR camera, specifically for a small unmanned aircraft, with limited power, space, and computing power is developed. A time sequential processing method is presented to reduce the required computing, while allowing high frame rate, real-time operation. Moreover, a windowed triple-vote method is continually applied to ensure that the detection mode is correctly set by the algorithm, while ignoring unexpected targets in the image. A simple background estimation method is presented to remove any non-uniformity in the captured images, resulting in a high detection rate with low false alarms. Finally, a complete, mission-ready payload system is prepared for small UA platforms, with an accuracy rate greater than 97% for the detection of self-propelled semi-submersible vessels.

Table of contents

List of tables

List of figures

x

List of abbreviations

ADS-B	Automatic Dependant Surveillance-Broadcast
ADSS	Analysts Detection Support System
AIS	Automatic Identification System
BH	Bottom Hat
CBP	Customs and Border Protection
CO_2	Carbon Dioxide
DTM	Digital Terrain Model
DTO	Drug Trafficking Organizations
FCM	Fuzzy Clustering Method
FOV	Field of View
GCS	Ground Control Station
H_2O	Water
hFOV	Horizontal Field of View
IMU	Inertial Measurement Unit
iFOV	Instantaneous Field of View
IR	Infrared
LPV	Low-profile Vessels
LWIR	Long-Wave Infrared
MWIR	Medium-Wave Infrared
NETD	Noise Equivalent Temperature Difference
NHT	Normalized Hough Transform
NIR	Near Infrared
NUC	Non-Uniformity Correction
RCS	Radar Cross Section
RMS	Root Mean Square
ROI	Regions of Interest
SAR	Synthetic Aperture Radar
SCR	Signal-to-Clutter Ratio
SPSS	Self-Propelled Semi-Submersible
SWIR	Short-Wave Infrared
TH	Top Hat
UA	Unmanned Aircraft
UAS	Unmanned Aircraft System
vFOV	Vertical Field of View

Chapter 1

Introduction

A reliable method for the detection of small submersibles off the vast North American coast is a necessary requirement. It has been reported that since June of 2017, seven low-profile smuggling vessels have been stopped in the southern corridor between Mexico and the United States [4]. Currently, the estimated rate of detection is slightly above 10% [5], equivalent to 60 vessels containing upwards of ten tonnes of illegal cargo undetected. Interdiction is a national security necessity for the safety and security in the ports along the coastlines of Canada, as well as the rest of North America. A smart payload, created for an unmanned aircraft platform allowing real-time detection of illegal traffic, could result in an increase in the number of detained vessels, while simultaneously reducing the resources required to find these vessels.

1.1 Objectives of Research

The primary objective of this study was to develop a real-time payload system, containing an infrared (IR) imaging device, specially designed for use in small unmanned aircraft (UA) systems for the specific mission of detecting self-propelled semi-submersibles (SPSS) over the vast ocean coastline. To properly create the system,

the following objectives must be completed:

- compare different thermal bands of IR imaging operation, in particular, medium wave infrared (MWIR) and long wave infrared (LWIR), to ensure that the selected technology is best for this application,

- identify the conditions associated with thermal wake development and persistence,

- confirm the temperature stratification of the ocean water during testing and compare to the expected thermal profiles,

- develop a reliable, real-time algorithm to detect a vessel based on its thermal wake pattern, and

- fabricate a mission-ready aircraft payload, including a ground control station (GCS).

1.2   Problem Statement

Detection of partially submerged targets, containing illicit cargo currently engages air- and ground-based assets and support, while still yielding a nominal detection and interception rate. The proposed payload system will result in an increase in the number of interdicted semi-submersible vessels along the North American coastline through the detection of the thermal wake patterns.

1.3   Technical Challenges

The deployment platform imposes restrictions on the available payload size and power, while still requiring full frame rate, real-time operation of the system.

A SPSS can travel at both day and night, up to 100 nautical miles off-shore to evade detection. In order to interdict the illegal traffic, this 100 nautical mile corridor must be patrolled 24/7, with the suspicious activity reported in a timely manner for effective interdiction. This extended range off shore does not allow practical relaying of real-time high-resolution video back to the on-shore GCS. Also, there is an altitude restriction on the UA to ensure altitude separation from manned traffic above, and for it to operate below cloud so that it can see or be seen by other manned traffic.

The above mentioned challenges are met by deploying autonomous sensor payloads over multiple unmanned aircraft in synchronized flight. Autonomous sensors address the video bandwidth limitation, and reduce the workload of the human GCS operators. Multiple synchronized aerial platforms via Automatic Dependent Surveillance-Broadcast (ADS-B) technology extend distance and increase swath of the surveillance corridor.

1.4   Contributions

This thesis, and the related publications, are the first known reports of thermal wake-based detection of SPSS. Several additions to the current literature and knowledge were developed in this work, including;

- The infrared sensor selection for the application of thermal wake detection is explored in Chapter 3, comparing data collected for medium-wave and long-wave infrared imaging devices from a low altitude aircraft platform. Section 3.4.2 provides specific comparisons, and demonstrates the capabilities for thermal wake detection for each sensor modality. A detailed comparison of MWIR and LWIR sensors over the ocean with correlated optical data for thermal wake detection and ship detection is uncommon in literature.

- Long wave infrared data is captured and presented from two different sensors, the FLIR Photon640 and FLIR A65. This data is compared as captured (Chapter 4), as well as after processing for detection of thermal wake patterns (Chapter 5).

- Chapter 4 demonstrates persistent thermal wake patterns, including cold (Section 4.3.1) and warm (Section 4.3.2) wake patterns, correlated to the recorded environmental conditions. The presence of the thermal wakes is supported with temperature measurements in the upper stratified layers of the ocean waters.

- A diverse set of variables are used for data collection. Thermal wake patterns are recorded using multiple sensors, over two different oceans, from two different countries.

- A real-time algorithm for a small unmanned aircraft platform to detect SPSS by thermal wake detection (Chapter 5). This is the initial publication of this concept.

- A time sequential processing system is disclosed to preserve real-time operation with limited processing (Chapter 5).

- A windowed triple-vote system using multiple frames to continually detect the detection mode of the algorithm is developed to increase the robustness of the algorithm (Chapter 5).

- Data sets for three different platforms, using two different LWIR imagers, over two oceans, were used to produce a dependable, real-time algorithm with nominal false and missed detections under the varied scenarios.

- A complete, mission-ready system is achieved, including both hardware and software packages.

1.5   Organization

This thesis is organized as follows: Chapter 2 provides an overview of the literature with regards to infrared technology and ocean-based sensing systems previously reported. Chapter 3 presents a comparison between medium and long wave infrared imagery for ocean-based sensing, and provides an overview of the physics related to infrared imaging devices, based mainly around passive detectors; MWIR and LWIR. Further, the process for the selection of an infrared sensor for ocean-based imaging is presented, including a comparison of medium-wave and long-wave images. Chapter 4 introduces the development of a real-time image processing algorithm for deployment on a small unmanned aircraft system, including thermal wake patterns in long wave infrared images, captured with a FLIR Photon640 long wave infrared imager. Image processing techniques are compared to accentuate these wake patterns for the observer. The results from an algorithm, designed to detect the thermal wake patterns from a small unmanned aerial platform with limited payload capacity are presented for both warm and cold water wake patterns. Chapter 5 presents the real-time detection algorithm applied to multiple sets of long wave infrared data. The development of the algorithm is outlined, comparing the Hough and Radon transform. A real-time algorithm for a 30 Hz imager is reported, with a low false detection rate, and few missed detections, as well as a robust system to account for sudden, unexpected changes in the collected images. The final chapter contains a summary of this thesis, outlines other potential areas of application of the technology developed, and presents an overview of future work related to this project.

Chapter 2

Background

There are currently no reports of the development of real-time algorithms for the detection of self-propelled semi-submersibles (SPSS). In 2006, when authorities reported the first detection of a SPSS in the eastern Pacific ocean, containing nearly 10,000 pounds of cocaine, multi-agency partnerships and assets were deployed as a countermeasure [6]. These low-profile SPSS vessels are designed to elude detection, with a sharp bow to cut through the water, an elongated body to transport high-value cargo, and only the single mast of the conning tower sticking out of the water [4]. An increased concern is legitimate, with the possibility of these SPSS being a national and global threat very possible. Small UA platforms equipped with a payload system to detect the discernible thermal wake trails would correspond to elevated detection rate.

Thermal imagery of the disturbed colder water layers, driven to the surface by the vessel will allow for the detection and therefore the interdiction of the illegal traffic. A completely autonomous system, including on-board processing for the smart recognition of the radar eluding, low profile vessels is required. This smart system could potentially be coupled with airborne automatic identification system (AIS) to

aid in the discrimination of legal and illegal marine traffic. Further, the ability to have multiple unmanned aircraft systems monitoring adjacent areas would aid in the follow-up mission to decrease false alarm rates and increase the percentage of detected illegal vessels.

Infrared imaging devices with a high resolution, a high responsivity, and a very low minimum resolvable temperature are required to provide high quality imagery for airborne detection of the thermal wake. IR signatures of ship wakes are highly variable in both persistence and temperature contrast as compared to the surrounding surface water, depending on both meteorological and oceanographic parameters [7]. These systems will require retrofitting to both increase durability, and reduce weight for housing in small UA. Advances and availability of current computer technology required for the smart on-board processing of the captured data will allow the real-time analysis of the captured imagery.

An unmanned aircraft with an integrated payload allowing the automatic detection of illegal traffic will greatly reduce the required resources for the detection of these SPSS, as well as increase the number of interdicted vessels. The threat of these vessels cannot be understated; payloads from drugs to weapons of mass destruction could be housed in these small SPSS. An increased detection of this illegal traffic is required for national security both in the ports along the coastlines of Canada, as well as the rest of North America.

There is no reported work on development of smart IR systems for detection of the thermal wakes of submarines. However, integration of IR cameras into commercially available computer vision technologies are used in applications such as quality control applications [8], oil slick thickness detection [9], and critical temperature measurements of machinery [10] to name a few. In these applications, IR imagers have

proven to be very effective, boasting multiple benefits over other technologies, including boosting efficiency and reducing costs. In particular, surveillance imaging systems with detection and tracking capabilities over complex terrain have been developed and have been demonstrated to be successful [11–13].

2.1   Self-Propelled Semi-Submersibles (SPSS)

The category of self-propelled semi-submersibles includes both semi-submersible vessels, which are capable of ballasting to a depth near the surface to decrease their surface profile, as well as low-profile vessels (LPV), more simply defined as a boat with a minimum radar cross-section [14]. These SPSS are expendable and cost-effective in contrast to fully submersible vessels, or submarines, which are more advanced, requiring significantly increased cost, effort, and skill to create [15].

First generation SPSS were sealed, unmanned platforms towed behind powered watercraft and readily expendable to avoid interdiction by law enforcement [15]. However, the performance specifications in more recently apprehended vessels are greatly improved, capable of speeds up to 13 knots, and travel range of upwards of 4000 kilometers with a cargo capacity up to 20,000 pounds. These self propelled semi-submersibles measure between 10 - 25 meters in length and 3 - 4 meters in width, with a protruding freeboard approximately 50 cm above the water line, and a propeller 3 - 4 meters below the surface. The SPSS maintain minimal visual signature and are equipped with equipment such as external camouflage, and self-cooling exhaust systems to elude detection [6]. The main benefit to a drug trafficking organization (DTO) in using semi-submersible vessels is that they are difficult to detect, and allow numerous smaller payloads which increases the probability of delivery [15]. Figure 2.1 presents a render of the Bigfoot II SPSS, which was captured 550 kilometers off the
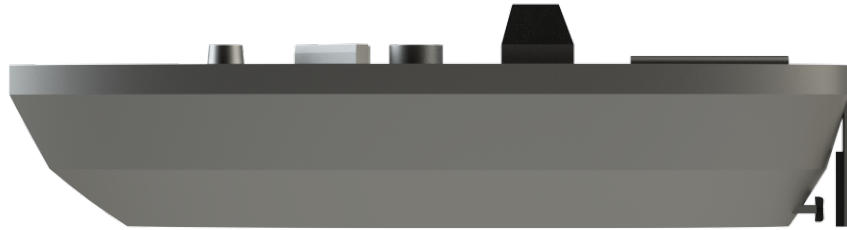
(a)
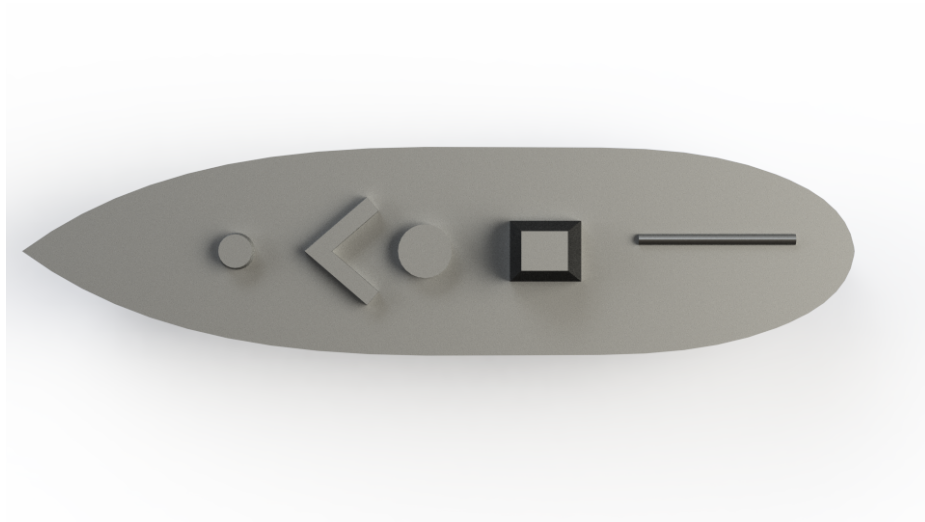
(b)

Figure 2.1: a) Side and b) top views of a rendered SPSS based on the reported design of the Bigfoot II which was 18 meters in length, carrying 12,800 pounds of cocaine when captured 550 kilometers off the coast of Mexico.

coast of Mexico by the U.S.S McInerney. When the crew boarded the vessel, they found 4 members plus 12,800 pounds of cocaine, worth \$107 million [5].

Continually increased use of SPSS resulted in efforts to increase the interdiction in the U.S., including the creation of the Drug Trafficking Vessel Interdiction Act in October of 2008, which gave the Coast Guard the authority to detain operators or travelers in an unregistered submersible vessel, including if no contraband is seized, for example if the vessel is scuttled. The legislation allows for a person convicted to receive up to 15 years in prison and a 1 million dollar fine [16]. During the same time period, Customs and Border Protection (CBP) equipped its P-3 aircraft with SeaVue maritime surveillance equipment in an attempt to better detect and track SPSS platforms [15].

In a document approved for public release in February of 2009 it states [15]:

> A key characteristic of a U.S. effort to deter or defeat the SPSS threat is that it must be multilateral; the U.S. simply does not have the manpower, the requisite number of detection and monitoring platforms, nor enough intelligence sources necessary to ensure unilateral success.

Between the months of August and October in 2011 the US Coast Guard apprehended three SPSS in the Caribbean, each carrying approximately seven tons of cocaine, worth over half a billion dollars total [17–19]. Further, the interdiction of a SPSS off the coast of Nicaragua by two P-3 Orions as part of the Joint Inter-agency Task Force-South (JIATF-S) ceased 14,000 pounds of cocaine [20].

2.2 Airborne Detection Systems

Airborne data collection is a large industry, including satellites, single engine piloted planes, and balloons. Specific to unmanned aircraft systems (UAS), current exemptions applied by governing bodies is allowing expansion of unmanned aircraft for near-range coastal monitoring, iceberg tracking, and pipeline management, to name a few. Although small unmanned aircraft can be used for collecting information, practical reports on their application are sparse and newly emerging. The registration of images acquired by sensors of many modalities is necessary for many applications such as image fusion, surveillance, and target detection and registration, since the information gained is of a complementary nature [21]. Particular to this work, airborne surveillance has proven to be important and applicable to a wide range of applications. Current common practice for UA platforms is to treat the UA as a sensor carrying platform, and transmit data to a ground station for analysis, since the on-board intelligence is lacking for data interpretation [12].

2.2.1 SPSS Detection

No reports of self-propelled semi-submersible detection algorithms are currently available for direct comparison. Reports of thermal wake patterns, created by larger surface bound vessels or submarines are summarized in Section 2.2.2. Similarly, thermal wake patterns created by marine mammals are compiled in Section 2.2.3.

2.2.2 Thermal Wake Patterns

Data from the NASA MASTER imager has demonstrated thermal wake patterns behind large surface traveling ships in band 44 (9.0970 μm) [22]. Garrett *et al.* demonstrated that the thermal signatures of oleyl-alcohol-treated ship wakes, to mimic organic material from ship effluent, generated under the same conditions were more intense and persistent than the untreated wake. It was also demonstrated that the thermal wake temperature was nearly the same as that of the water at the keel [7]. Stewart *et al.* created a numerical model of the thermal wake caused by the turbulent water motion behind a ship. It was reported that the modelled wake patterns agreed with experimental data, including the warm water wake during night due to a lack of surface heating [23]. Zhang *et al.* provided a theoretic basis for IR detection of the submerged vessels, and demonstrated in a wave tank as much as a 3^oC temperature differential of the wake, equivalent to the temperature difference of the stratified water [24,25]. Further theoretical support was also reported by Wu *et al.* [26] and Zhang *et al.* [27]. Wu *et al.* presented IR images of the cold water wake, finding a persistence of 145 seconds of the cold water wake [26]. Benilov *et al.* presented theoretical and experimental results of the detection of moving bodies and divers in IR images. A comparison of medium wave infrared (MWIR) and long wave infrared (LWIR) images of a wake created by a ship revealed a dark wake pattern in the MWIR, and a bright pattern in the LWIR. This was attributed to strong surface reflection in the slick like wake area [28]. For a ship moving at a steady rate, Voropayev *et al.* noted a significant wake contrast for warm surface water with a stratification temperature difference in the first 10 meters of 1^oC [29].

2.2.3 Marine Mammal Detection

The detection of marine mammals has received increased attention in the last decade. Observation of whale temperatures 0.5^oC - 1.0^oC warmer than surrounding sea temperatures, as well as blow temperature 0.3^oC - 4.0^oC higher than the surrounding water demonstrated the ability to detect the marine life using land-based IR imagery. However, no whales were directly detected using IR, and thus Cuyler *et al.* concluded that thermal detection was unreliable [30]. For the purpose of identification of whales based on dorsal sightings, Graber calculated the mean pixel value in sections of approximately 1350 frames, and then removed the mean image from each frame, revealing the dorsal fins. Averaging the pixel value over a number of frames is done to correct for drift, but is only useful in the case of a stationary imager. The frames, after subtraction of the mean image, was then used to create an automatic detection algorithm which differentiated between dorsal fins and other image features based on temperature contrast with the surroundings [31]. Perryman *et al.* used thermal imagery to track the migration of gray whales for three years, reporting that blows were visible both day and night, with decreased probability on poor weather days [32]. Baldacci *et al.* further demonstrated the use of IR imagery to detect blows, as well as body, noting the ineffectiveness of LWIR (8-12 μm) in high humidity conditions [33]. The first observations of the thermal footprint using IR imagery resulting from the tail fluke of a whale was reported by Churnside *et al.* from a twin-engine airplane. They noted trails up to 300 m behind humpback whales, for which they estimated to have a velocity of 2.4 m/s, meaning the thermal trail persisted for about 2 minutes [34].

2.2.4   Other Airborne Measurement Techniques

It has been demonstrated that infrared thermal imaging, coupled with a visible band camera, allowed stream temperature measurements previously unavailable at the extent and resolution that were measured [35]. Jensen *et al.* reported stream temperature measurements for environmental monitoring using a LWIR sensor with a resolution of 640 x 480 on a UA platform. IR temperature measurements were found to be lower when compared with instream measured temperature values, explained as being due to wind blown across the IR imagers lens, as well as potential areas of high humidity attenuating the IR signal. By correcting the thermal images, Jensen *et al.* were able to demonstrate complex temperature profiles, in particular, warmer temperatures in stagnant areas [36].

Lu *et al.* reported an auto-tracking algorithm, developed for UA platforms, for power line inspections, using a combinations of optical, IR, and ultraviolet imaging technologies. The system begins with GPS coordinates of pole towers provided by the ground station. It identifies the two pole towers closest to its position, and creates a vector between the poles for the cameras to follow to ensure that the lines are imaged during the flight [37].

Infrared imaging in vegetation monitoring has also received a great deal of attention. Suzuki *et al.* developed a low cost, high resolution vegetation monitoring system to capture widespread mosaic images [38]. Using infrared and visible cameras widespread mosaic images were presented, with a vegetation index automatically calculated, demonstrating an effective, low-cost vegetation observation application. A machine vision system for UAS to acquire and interpret data in real-time, followed by decision-making is presented in Ref. [12], first reducing the noise in the images through Gauss filtering. Next, each image is segmented into regions, and the size and mean intensity of these regions are selected as features, producing a series of feature

vectors for each image, which are used in a fuzzy classifier to assign a number relating to a region. If a region continues to return a high possibility of being a target, an alarm is created. In particular for training, a series of images where a fire is present were used, reporting approximately 90% of the cases correctly.

Yakimenko *et al.* reported on the development of a UAS shipboard autoland system, leveraging LWIR sensors for ship detection from long range, and feature detection at closer range [39]. LWIR sensors were shown to reduce the complexity of locating the ship in sun glare and dark conditions, in particular for detection of the hot smoke stack or engine. For the landing system, once the hot spots were determined, a running average of each row of pixels was computed, which was then used to subtract from each pixel, to aid in selecting the hot spots. Once found, the hot spots were tracked by computing a bounding box around, and using inertial data to predict the approximate location and size in consecutive images.

2.2.5 Surface-based Vessel Detection

Detection algorithms for surface vehicles have also benefited from the use of IR imagers. Martins *et al.* segmented the sea and sky at the horizon in LWIR images using a Hough transform for detecting linear edges. Since a high contrast exists between the sea water and a human target due to temperature differences, histogram expansion for contrast improvements, then centroid region calculations are carried out [40].

Diana *et al.* reported a clutter removal procedure which estimates the background and striping noise consecutively is implemented. The main feature of the technique is that the noise sources are estimated in a single step [41]. Moreover, using a local directional background removal filter, with a modified mean subtraction filter, a small target detection system to detect targets in the horizontal region is reported. The method presented by Kim *et al.* provides filtering and detection performance, with

high detection rates and low false alarms per image, compared to top-hat filter-based methods in real scenarios [42].

2.2.6 Synthetic Aperture Radar

The remote detection of ships through the detection of their wakes is directly related to national security, navigation safety, and fishing and pollution monitoring [43]. The narrow, V-shaped wake patterns have been reported to extend up to 20 km behind surface-based vessels, and were first reported on images in 1978 from SEASAT, the first satellite designed for remote sensing of the Earth's ocean using synthetic aperture radar (SAR) [44, 45].

The appearance of the ship wake patterns in synthetic aperture radar systems is similar to that of the cold water wakes recorded for semi-submersibles. Significant attention and development has occurred on the detection of ships or ship wake patterns in SAR imagery with an aim of creating an analysts detection support system (ADSS) to guarantee consistency and predictability in the large amounts of data generated in modern SAR systems [46]. Synthetic aperture radar images represent the radar reflectivity of a scene, expressed in terms of the radar cross section (RCS), σ. The distinguishing feature of SAR images as compared to other radar images is a high resolution can be achieved in the azimuth and range direction mathematically by the creation of a synthetic aperture. Moreover, there are different SAR image formation algorithms, related to different modes of operation [46]. It is notable that the thermal wake patterns of the SPSS are not visible in the SAR images since the thermal wake does not create any visible changes in the ocean's surface.

SAR systems have been deployed on both airborne and spaceborne platforms. Generally, airborne platforms are multi-frequency, multi-polarization systems, which result in better image quality. In comparison, a real-aperture radar system on an

air- or spaceborne system yields poor resolution of ship wakes due to the small ratio of the radar aperture length to the distance from the radar to sea, compared to the large effective aperture of a SAR unit [47]. Conversely, spaceborne SAR systems are simpler, but provide a wider spatial coverage, with increased visit frequency, for use in wide area surveillance systems. For this reason, the majority of ship detection systems have been designed for spaceborne satellite systems [46]. Specifically for ship detection, two targets exist, which requires different algorithms. Detection of the ship itself can be beneficial since the ship appears bright in SAR images, and exists when the ship is not moving. Detection of wake patterns is advantageous since the wake pattern is much larger and more distinct than the ship, and wake detection yields a better estimate of the ships location and moving parameters as compared to the ship itself [48].

The recirculating flow behind a moving vessel appears as a single bright or dark line coincident with the ship track at higher wind speeds, or as one or multiple V-shapes at lower wind speeds [49]. These ship wake patterns can be divided into two parts: Kelvin wake patterns and other non-Kelvin wake parts [47, 50]. Kelvin wake patterns, well known in classical fluid dynamics, are due to diverging and transverse waves created by flow around the ships hull. Non-Kelvin wake parts include local waves from the breaking bow, stern waves, a viscous wake from rotational motion flow from the ship boundary layer, and other far reaching manifestations of these features, which comprise the narrow trailing region of the wake [23, 47]. Ship wakes differ based on vessel properties and hydrometeorlogical parameters. Therefore, knowledge of the resulting ship wake allows an estimate of the moving ship parameters such as velocity and direction [51], as well as estimates of hull characteristics such as length, width, volume, and other offsets [52]. A detailed analysis of ship wakes and the resulting radar images is presented in Ref. [47].

The detection and registration of ship wakes in SAR has received a great deal of attention in order to improve the probability of detection and reduce the false detection of vessels. Transformation algorithms, such as Radon transform, which accentuate straight line features in an image through integration of image intensity along all directions in the 2D image space have proven to be most successful in wake recognition. This integration process also tends to cancel noise in images, resulting in a greater signal-to-noise ratio in the transform image as compared to the original [53]. It is estimated that the combination of recent advances in SAR technology, an increase in the number of available SAR platforms, and observable growth in automatic ship wake detection systems could make real-time detection of ship from space possible in the next 5 years [43]. Currently, ADSS which automatically detect ship wakes are being used as an analysts aid due to the large amount of data collected in short periods of time, the large amount of open ocean in the captured imagery, and the potential to guarantee consistency [46].

An automatic ship and ship wake detection algorithm, reporting a 7-8 % missed ship rate, and 15 % missed wake rate, and 0 % false detection rate was reported in Ref. [54]. The system is specifically designed for coastal regions with eddies, land front, waves, and swells. Therefore, land regions are first masked using a digital terrain model (DTM), then an adaptive filter is used to detect ship targets by connecting pixels if they have much higher values then the background. The detection of the ship feature is used as a part of the detection algorithm, but also the detected ship pixel values are replaced with background values, so the ship is homogeneous with the background. Finally, the Radon transform is used to accentuate straight line features in the SAR images. Chen *et al.* presented a method called ellipse normalize Radon transform to detect the dark lines of the turbulent wake in SAR images [48]. This method combines the key features of the Radon transform with the localization

abilities of the contourlet transform, which reduces the speckle noise and removes the large scale change in the background. The detection algorithm first removes any islands or other land formations using geography information so that individual dark lines can be detected in a gliding window. The contourlet transform despeckles the images and then the Radon transform searches for dark lines using the ellipse normalization scheme. This method was shown to work well for estimation of ship wakes in SAR images, as well as detection of weak lines in noisy background. However, the algorithm requires external information to remove the additional noise, and is limited in field due to processing images window-by-window. Another method using the gliding-box algorithm, employing a Radon transform-based algorithm, resulting in a improved linear feature detection method was presented by Du *et al.* [55]. The box of dimensions s x s glides on an overlaid lattice in the image plane of size W x W, where each gliding step is t. In each box, a Radon transform is performed, of which the mean and standard deviation are calculated, which is used to set the detection threshold. This method was reported to have a higher detection accuracy than the standard Radon transform, in particular with a better estimate of line length, which could not be achieved with the conventional Radon transform. A radon transform-based method with morphological processing was presented in Ref. [56], reporting a robust detection algorithm, in particular in a noisy background. Courmontage [57] provides a detailed report on a new process for ship wake detection in SAR images, combining the Radon transform and a stochastic matched filtering method to interpolate the image in a rotating reference system. As opposed to several reports which utilize the Radon transform to remove speckle noise, the rotating reference system of interpolated images is instead used for the Radon transform to compute the interpolations of the SAR image to properly estimate the ship wake. This method is reported to improve the signal-to-noise ratio after processing since there is no sinusoidal curves corresponding

the speckle noise in the Radon domain, resulting in an improvement in ship wake detection [57].

Jiaqiu *et al.* presented a ship wake detection algorithm based on a normalized Hough transform, of a particular length, such that it does not require preprocessing of the image to remove noise, and does not apply the transform across the entire image as in Radon transform algorithms [51]. The proposed algorithm is based on a signal-to-clutter ratio (SCR) enhancement to sub-divide the image and normalized Hough transform (NHT) for wake detection.

Barni *et al.* presented an algorithm to detect oil spills in SAR images, where a non-linear filter is applied to reduce the speckle noise, followed by fuzzy clustering method (FCM) to create a preliminary partition in the image by assigning each pixel a value within a membership function [58]. The FCM assigns a value between 0 and 1 based on how much of the pixel belongs to a surface cover class, allowing the algorithm to deal with complex situations very well. After applying the FCM, the clusters are merged based on clustering in a map using a Sobel operator.

Synthetic Aperture Radar has proven very useful and efficient in identifying and quantifying oil spills. Oil has a high thermal conductivity and low heat capacitance, such that oil spills heat quickly, becoming warmer than surrounding sea water in the day, and losing heat much faster, becoming cooler than water during the night. However, SAR images suffer from a poor signal-to-noise ratio due to sea moisture, surface roughness, and difference in surface roughness. Alli *et al.* presented an adaptive system based on a fuzzy logic control algorithm to limit the amount of noise in the SAR system [59]. The filter first estimated a fuzzy derivative, such that it would be less sensitive to local variations due to structures such as edges. Next, the membership functions were adapted to the noise level to perform a smoothing. Barni *et al.* described a three step algorithm to segment oil spills from marine backgrounds in SAR

data from SEASAT and ERS-1 [58]. Using a non-linear filter, the speckle noise was reduced. Six different filters were compared, noting that the sigma and Kuan filters produced the best results. Next, using fuzzy clustering to deal with the complex situations of cover class mixture and vague boundaries, which are common in remote sensing data, a preliminary partition is produced. Finally, an edge driven cluster merging technique is carried out to refine the segmentation from the fuzzy clustering. In Ref [60], de-noising and enhancement of oil slicks in SAR data by speckle reducing anisotropic diffusion was reported. This method is shown to be quite beneficial in reducing noise compared other filters. Fjortoft *et al.* presented a segmentation scheme for SAR data based on edge detection and region growing [61]. By computing an edge strength map from the ratio of exponentially weighted averages, the difference in the weighted averages were computed on each side of the pixel from a normalized ratio. Watershed thresholding was used to obtain closed boundaries. The false detections from the watershed were then reduced by merging regions whose mean values are not significantly different. Chaudhuri *et al.* took a statistical approach to automatic detection of general disturbances in the ocean. Local statistical-based enhancement techniques were used to enhance the disturbance features of the ocean's surface. Segmentation based on feature occurrence convergence partitions the image into target and no target localizations [62].

Chapter 3

Comparison of Medium and Long Wave Infrared Imaging for Ocean-Based Sensing

3.1 Introduction

The infrared region of the electromagnetic spectrum refers to a wide range of wavelengths between 740 nm and 300 μm, much of which is not useful for ground- or sea-based imaging due to atmospheric absorption. The remaining high-transmission bands are generally broken into four categories [63]:

- Near Infrared (NIR) 0.75 - 1.4 μm,

- Short-Wave Infrared (SWIR) 1.4 - 3 μm,

- Medium-Wave Infrared (MWIR) 3 - 8 μm, and

- Long-Wave Infrared (LWIR) 8 - 15 μm.

MWIR and LWIR imaging systems can operate completely passively, with no external illumination since the imager senses the energy directly radiated from the object.

Medium wave infrared and long wave infrared devices can also be split into two separate classifications based on the detector. Medium wave infrared imagers use photon detectors, in which the radiation is absorbed within the material through interaction with electrons causing a change in the electronic energy distribution in the output. Long wave infrared imagers employ thermal detectors, where the incident radiation is absorbed, and results in a change in the temperature of the detector material [64]. Photon detectors boast many benefits over thermal detectors, including a lower signal-to-noise ratio, and a very fast response. However, in general, these detectors are heavier and more expensive, mainly due to cooling requirements of the semiconductor photodetectors. The slower and less-sensitive thermal detectors, operate at room temperature and are much lighter and more rugged.

Currently, infrared imaging devices are being used in fields ranging from environmental monitoring, to building and home inspections, as well as medicine, agriculture, surveillance, and fire detection, to name a few. Airborne data collection is a large industry, with an increasing number of reports from unmanned and manned platforms of infrared data collection and applications. Using a long wave infrared camera, stream temperature measurements were recorded from an unmanned aircraft platform. Complex temperature profiles were reported, including warmer water in stagnant areas after corrections to the data for wind blown across the imagers lens, and areas of high humidity [36]. Coupling of infrared thermal imaging with an electro-optical imager allowed for determination of stream temperature measurements, previously unavailable to the extent and resolution that were measured, demonstrating the benefits of thermal imaging for environmental monitoring [35]. Long wave infrared imaging has

been demonstrated to solve the challenges associated with oil spill detection in water due to the uniform emissions in the long wave infrared band, and contrast of oil with surrounding water [65]. Finally, use of infrared imagery for the detection and recognition of large vessels has been demonstrated, reporting an increased detection compared to optical imaging technology [66, 67].

Several works have been published on the detection of large marine mammals; observation of whales with temperatures 0.5 - 1.0^{o}C warmer than surrounding sea temperatures, as well as blow temperature 0.3 - 4.0^{o}C warmer than the surrounding water, demonstrating the ability to detect the marine life using land-based IR imagery [30]. Tracking of the migration of grey whales for three years demonstrated that blows were visible both day and night, with a decreased probability of spotting blows on poor weather days [32]. Further demonstration of the use of infrared imagery to detect whales based on spray patterns and body temperature was reported, noting the ineffectiveness of LWIR in high humidity conditions [33]. The first observations of a thermal footprint, due to mixing of the stratified water, resulting from the tail fluke of a whale was noted from a twin-engine airplane using IR imagery. It was reported that trails up to 300 m behind humpback whales, for which they estimated to have a velocity of 2.4 m/s, were found. Under these conditions it was calculated that the thermal trail persisted for about 2 minutes [34]. A comparison of MWIR and LWIR of a wake created by a ship revealed a dark wake pattern in the MWIR, and a bright pattern in the LWIR. This was attributed to strong surface reflection in the slick-like wake area. It was reported that for a ship moving at a steady rate, in the presence of surface heating which creates a temperature stratification in the top 10 meters of 1°C, the wake contrast will be significant [29]. An image processing algorithm to detect illegal sub-surface vessels based on the thermal wake scarring in the long wave infrared region was reported, reporting a low false detection rate, and the potential

for real-time performance [68].

This Chapter provides an overview of the physics related to infrared imaging devices, based mainly around passive detectors; MWIR and LWIR. Further, the process for the selection of an infrared sensor for ocean-based imaging is presented, including a comparison of medium-wave and long-wave images.

3.2 Theory

A thermal imager converts energy in the infrared region of the electromagnetic spectrum into a visual representation of the temperature profile of a scene. The total contributions of radiation of the thermal profile of a scene are a result of an object emitting radiation, as well as reacting to incident radiation by reflecting or absorbing some portion of it.

3.2.1 Measurement Process

Conservation of energy requires that the sum of the absorbed, transmitted, and reflected energy be equal to the incident energy, described with the coefficients of absorption, α, reflection, ρ, and transmission, τ, as [63]

$$\alpha + \rho + \tau = 1. \tag{3.1}$$

A perfect blackbody is a perfect absorber of energy, such that $\alpha = 1$, and therefore $\rho = \tau = 0$.

Planck's Law describes the radiative properties of a perfect blackbody in terms of the spectral exitance, M_λ, as a function of temperature, T, and wavelength, λ, such

that

$$M_\lambda(\lambda, T) \;=\; \frac{2\pi hc^2}{\lambda^5}\left(\frac{1}{e^{hc/\lambda k_B T} - 1}\right) \tag{3.2}$$

where h is Planck's constant, c is the speed of light, and k_B is Boltzmann's constant [69]. The wavelength of peak exitance, λ_{max}, determined by differentiating Equation 3.2 with respect to λ, (with $M_\lambda{=}0$) is found to be

$$\lambda_{max} \;=\; \frac{hc}{5k_B T} \;=\; \frac{2897.885}{T} \; [\mu m \cdot K] \tag{3.3}$$

known as the Wien displacement law [70]. Further, the Stefan-Boltzmann law gives the total radiant heat energy emitted from a body, found by integrating Equation 3.2 over all wavelengths,

$$W \;=\; \sigma \, T^4 \tag{3.4}$$

where σ is the Stefan-Boltzmann constant [71, 72]. Figure 3.1 presents Planck's Law for different temperature values between 273 - 1000 K, along with calculated values for the wavelength of peak exitance and total radiant exitance corresponding to the curves. As the temperature increases, the wavelength of peak exitance decreases, while the total power emitted by the blackbody increases. At 273 K the value of peak exitance is 10.61 μm, whereas at 800 K the value of peak exitance is found to be 3.62 μm, which fall in the LWIR and MWIR range, respectively. Further, the total radiated energy at 800 K is found to be approximately 70 times larger than at 273 K.

To satisfy equilibrium conditions, Kirchoff's Law states that the coefficient of absorption must equal the emissivity, $\alpha \;=\; \varepsilon$, which describes the efficiency with which a blackbody radiates energy. Radiation from a real source is always less than a blackbody, however. In general, most materials studied for practical applications are

assumed to be greybodies, which have a constant scale factor relative to a blackbody [73]. It follows then that for a real surface the emissivity can be defined as [63]

$$\varepsilon = \frac{W_{obj}}{W} \tag{3.5}$$

where W_{obj} is the measured total radiant exitance from a surface, and W is the calculated total radiant exitance of a blackbody at the same temperature.

The radiation energy received by the sensor of an infrared camera is the sum of emitted radiation from the target object, the radiation from the surroundings reflected on the target object, and emitted radiation resulting from absorption of radiation in the atmosphere. It follows that the total radiation received by the sensor can be described as

$$M_{total} = \varepsilon \cdot \tau_{atm} \cdot M_{obj}(T_{obj}) + \rho \cdot \tau_{atm} \cdot M_{surr}(T_{surr}) + \varepsilon \cdot M_{atm}(T_{atm}) \tag{3.6}$$

where τ_{atm} accounts for attenuation in the atmosphere due to absorption and scattering [74]. If the object is an opaque greybody, then $\tau = 0$, and Equation 3.1 simplifies to give

$$\rho = 1 - \varepsilon. \tag{3.7}$$

Further, it is reasonable to assume that atmospheric transmittance is dominated by absorption losses, such that $\varepsilon = 1 - \tau_{atm}$ [63]. Therefore, Equation 3.6 becomes

$$M_{total} = \varepsilon \cdot \tau_{atm} \cdot M_{obj}(T_{obj}) + (1-\varepsilon) \cdot \tau_{atm} \cdot M_{surr}(T_{surr}) + (1-\tau_{atm}) \cdot M_{atm}(T_{atm}). \tag{3.8}$$
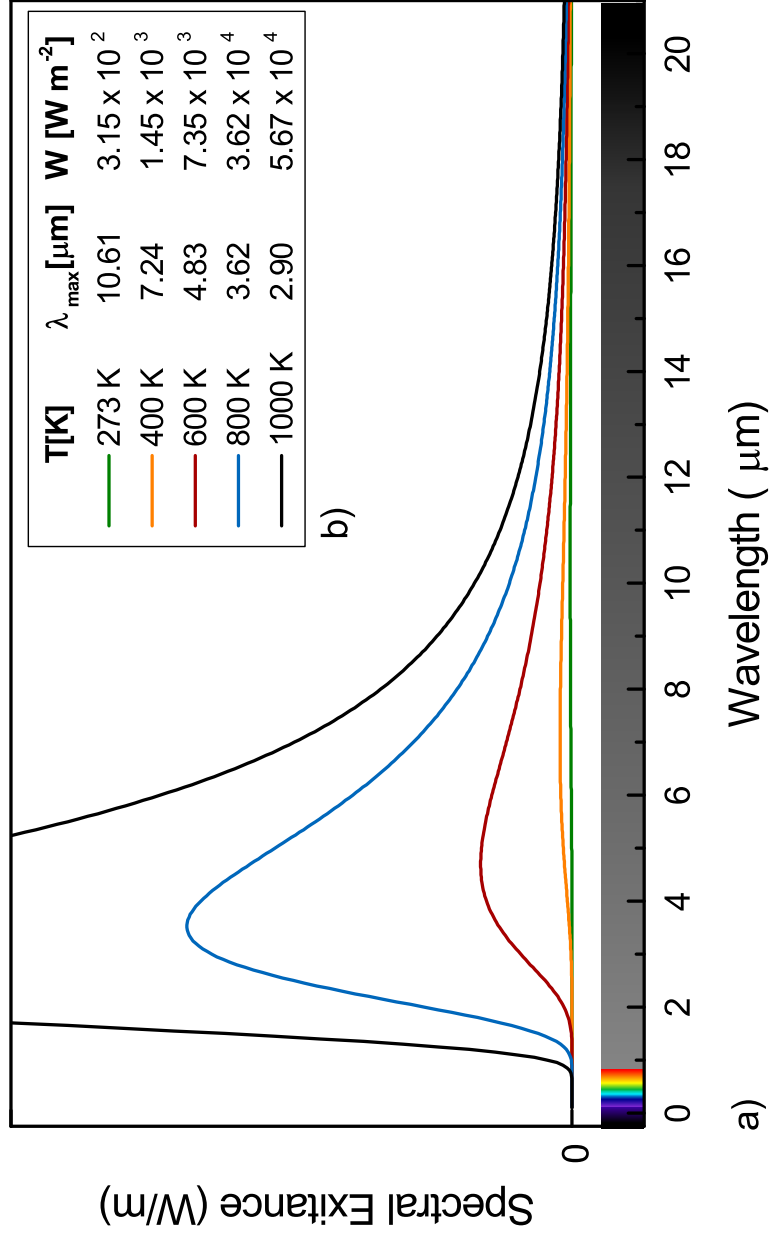
Figure 3.1: a) Illustration of Planck's Law at different temperatures. b) Calculated values of λ_{max} and W for each curve.

3.2.2 Atmospheric Effects

Atmospheric window regions are defined by molecular absorption by atmospheric molecules, primarily CO_2 and H_2O vapor. From Equation 3.8, it becomes obvious that thermal imaging is very sensitive to external influences on the radiation that the camera detects [74]. The absorption of the radiated energy is related to the extinction coefficient, κ, as [63]

$$\alpha(\lambda) = \frac{4\pi\kappa(\lambda)}{\lambda}. \tag{3.9}$$

Figure 3.2 shows the atmospheric transmission of radiation from 0.9 - 5.6 μm and 7 - 26 μm in the skies above Mauna Kea Observatories in Hawaii (Data from Gemini Observatory [2]).

The absorption of a material also governs the penetration depth of the electromagnetic wave into a surface, such that according to the Beer-Lambert law, the intensity, I, decreases as

$$I(d) = I_o e^{-\alpha \cdot d} \tag{3.10}$$

where I_o is the initial intensity, and d is the depth. The penetration depth, δ_p, is simply $\alpha = \delta_p^{-1}$ [75]. The absorption coefficient, α, greatly varies depending on the wavelength (see Figure 3.3). In the visible region of the electromagnetic spectrum (390 nm - 750 nm) the absorption reaches below 0.001 cm^{-1} with penetration depths to almost 1000 m. In this region the transmittance is much larger that zero, as expected as water is a transparent material. Conversely, in the infrared wavelength range (770 nm - 100 μm) water is essentially opaque, with a transmittance of approximately zero. Absorption coefficient values are between 0.1 and 10^4 cm^{-1}, such that infrared radiation is absorbed between 10 μm and 1 m of the water surface [3].

3.3   IR Selection parameters

An understanding of the parameters which affect the resulting data collected by the infrared camera is required to maximize the use for detection, tracking, or other applications.

3.3.1   Spectral Band

The two wavelength windows of importance for thermal imaging are medium wave infrared and long wave infrared. The 5 - 8 μm range is unusable due to absorption by water vapor in the atmosphere, note that $\tau = 0$ in this range in Figure 3.2. Depending on the application, the wavelength range of the sensor has a significant impact on the results. Moreover, LWIR and MWIR differ with respect to atmospheric transmission. MWIR has superior clear weather performance, with a higher transmissivity under high humidity, whereas LWIR performs better in fog and dust conditions, and has a higher tolerance to atmospheric turbulence [76]. By comparison, in a category II fog, in which the visual detection range is 0.61 km, it has been reported that the detection range was 0.54 km and 2.4 km for MWIR and LWIR, respectively [77].

3.3.2   Thermal Resolution

The thermal resolution of the infrared imager is the smallest temperature difference that can be measured. This measure is commonly expressed as the NETD, or noise equivalent temperature difference, determined as the temperature difference which produces a signal equal to the camera's temporal noise [78]. NETD is determined by multiplying the detectors RMS noise by the signal measured over the temperature difference. Currently available uncooled LWIR sensors report a NETD of approximately 30 mK. Cryogenically cooled detectors have an increased sensitivity, resulting in a
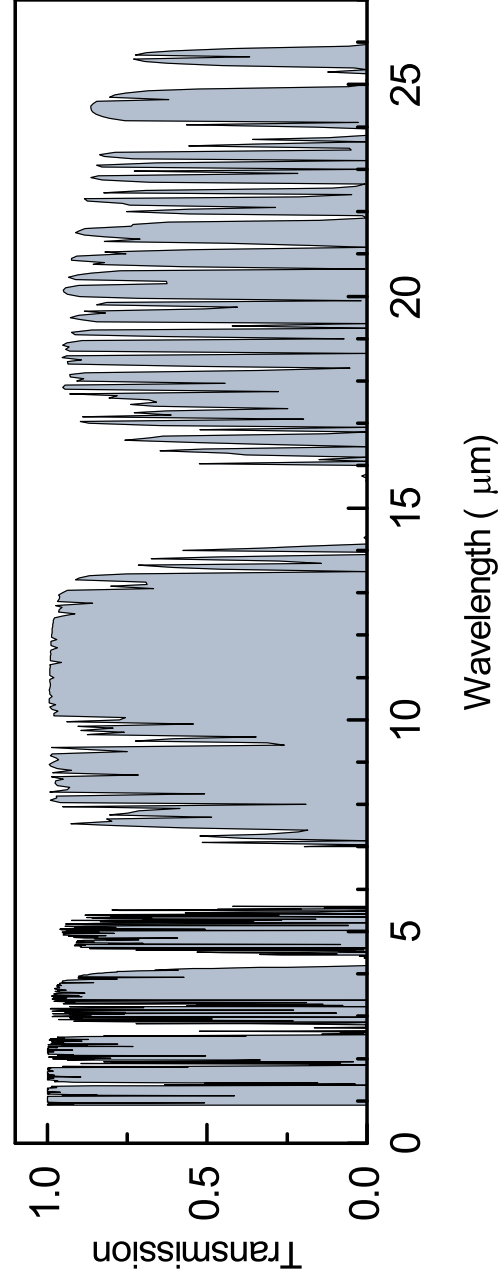
Figure 3.2: Atmospheric transmission plotted for 0.9 - 5.6 μm and 7 - 26 μm. Data collected at the Mauna Kea Observatories, generated using the ATRAN modelling software [1] and provided by the Gemini Observatory [2].
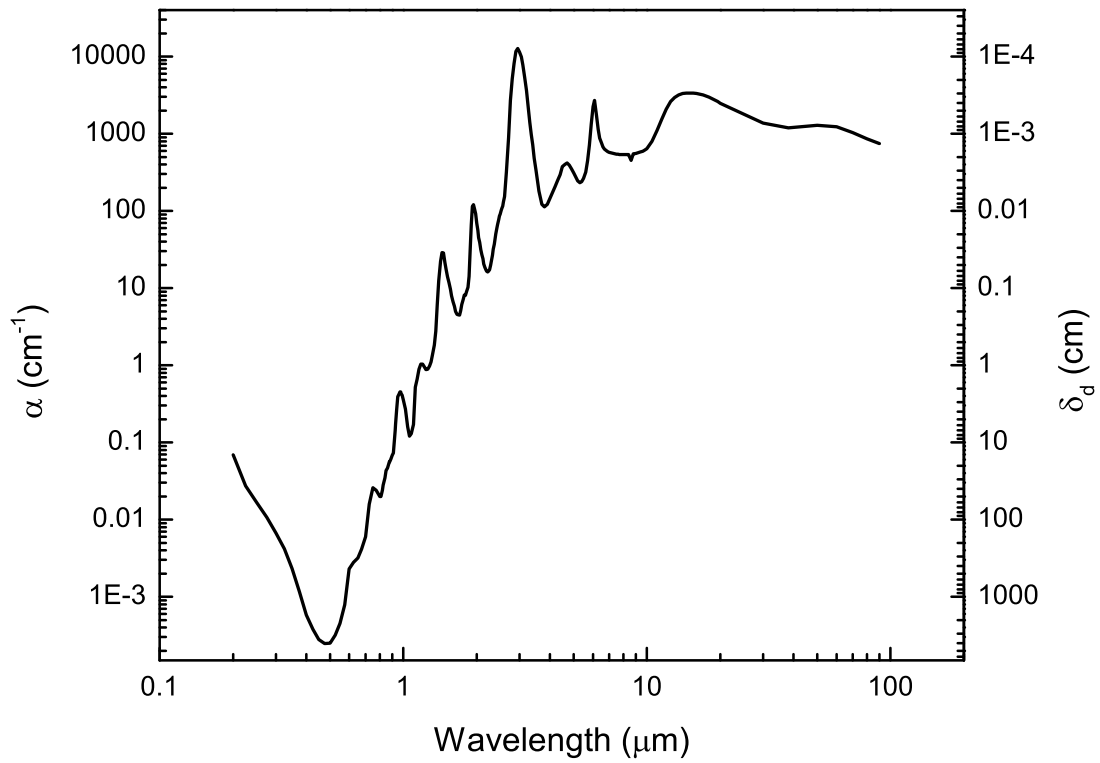
Figure 3.3: Absorption coefficient (α) and penetration depth (δ_p) from 200 nm to 100 μm of water at 298 K [3].

lower NETD value, with currently available cryogenically cooled MWIR and LWIR reporting NETD values less than 20 mK and 25 mK, respectively. Cryogenic cooling becomes a requirement when an increased sensitivity is needed in the wavelength range of the imager [77].

3.3.3 Integration time

The exposure time represents the time required for an infrared camera to capture a single frame of data, commonly also referred to as the exposure time or thermal time constant. It is analogous to the shutter speed of a digital camera, where the opening and closing of the shutter to collect the photons creates a single frame. If an infrared camera is moving quickly, a shorter exposure time is desired since it is less likely to result in image blurring. However, the shorter integration time may result in under-exposure. Longer exposure times allow more collection of the incoming energy from an object, but will result in blurring for a quickly moving frame. In general, there is an inverse relationship between exposure time and sensor sensitivity, where highly sensitive sensors require less time to collect the same image. Moreover, the integration time also affects the frame rate that the infrared imager can record data. With frame rates ranging from 9 Hz, up to 380 Hz, a higher frame rate increases the amount of data collected.

3.3.4 Field of View

The field of view (FOV) is the angular extent of the observable object field, defined by the lens and detector of the imager [74]. The field of view can calculated as

$$FOV \; = \; 2 \cdot d \tan \frac{\theta}{2} \tag{3.11}$$

where d is the distance to the scene, and θ is the angle of view. Figure 3.4 shows the field of view for a imager, where hFOV is the horizontal field of view, vFOV is the vertical field of view, and iFOV is the instantaneous field of view. The spatial resolution of the focal plane array describes the instantaneous field of view. This is the extent of an individual pixel, determined by dividing the FOV by the pixel dimension of the given axis.

The iFOV can be increased by decreasing the distance between the imager and target, or by decreasing the angle of view of the infrared camera. For example, if an infrared imaging device is fixed to an aircraft flying at an altitude of 150 m above sea level, where the lens of the imager has a angle of view of 26° x 20°, the FOV is determined to be 69.3 m x 52.9 m, and the iFOV is calculated to be 10.8 cm/pixel x 10.3 cm/pixel. If θ remains constant, and d is increased to 600 m above sea level, the FOV becomes 277.0 m x 211.6 m, and the iFOV is 43.0 cm/pixel x 41.3 cm/pixel. If instead the angle of view of the IR camera is 14° x 11°, the FOV at 600 m would be 147.3 m x 115.5 m, and the iFOV would be 22.9 cm/pixel x 22.6 cm/pixel. If the object of interest is known, selecting a lens such that the object fills the FOV will result in the best imagery with the most measurement data on the object.
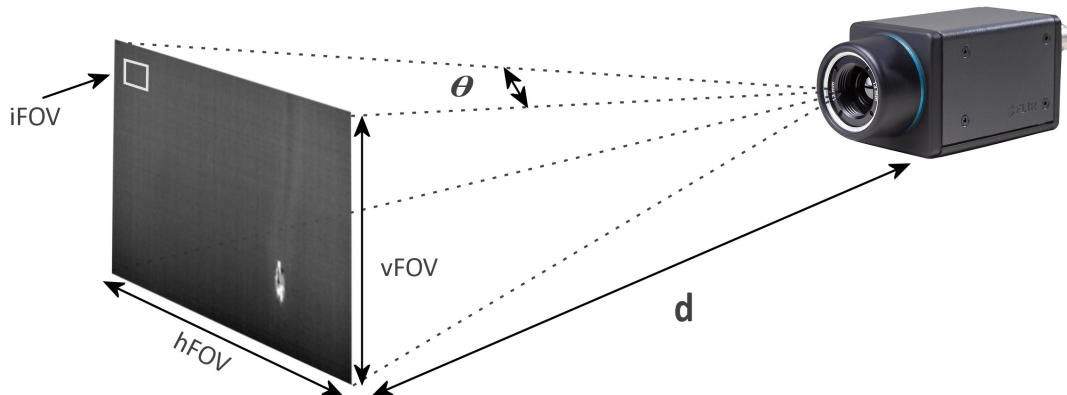
Figure 3.4: Demonstration of the field of view for an infrared camera.

3.3.5   Bit Depth

The total number of intensity values that can be stored for a given scene is dependent on the bit-depth of the recorded data. In general, infrared images are recorded as 8-bit or 14-bit images, and with 2^n available bins, this results in 256 and 16384 individual intensity bins available for the recorded data, respectively. If the NETD of the imager is 50 mK, the range of temperature values available for a 8-bit imager is 12.8 K, whereas for a 14-bit imager is 814.2 K.

3.4   Results & Discussion

3.4.1   Experimental Design

The data presented in this section was collected from a float plane in the channel between Portugal Cove and Bell Island in Newfoundland, Canada. The approximate average speed of the aircraft was 60 knots, with a height above sea level between 150 m and 300 m. On this day, St. John's International Airport reported a mean temperature of 12°C, with a maximum temperature of 15.3^{o}C, and a minimum temperature of 8.6^{o}C. A FLIR Photon640 LWIR camera, a FLIR SC5000 MWIR camera, and a Panasonic video recorder were mounted on a hand-held platform, with approximately 20 cm between each camera. Table 3.1 presents a comparison of the specifications of the thermal imaging devices used. It should be noted that the intensity values of the medium wave infrared images have been adjusted using *imadjust* in MATLAB [79] so the 14-bit data could be viewed.

Table 3.1: Infrared imager comparison for options used during the data collection presented.

Device	FLIR Photon640	FLIR SC5000
IR Range	7.5 - 13.5 μm	2.5 - 5.1 μm
Detector	Vanadium Oxide	Indium Antimonide
Resolution	644 x 512	640 x 512
NETD	50 mK	20 mK
Integration Time	10 ms	1 μs - 20 ms
Frame Rate	9 Hz	60 Hz

3.4.2 Infrared Image Comparison

Figure 3.5 shows a comparison of an optical, medium wave infrared, and long wave infrared image taken from an aerial platform of an approximate 52 m x 15 m ship, travelling with an average speed of 10.2 knots. In both the MWIR and LWIR images, the ship appears lighter than the surrounding water, indicating that the ship temperature is higher. Calculating λ_{max}, assuming that the temperature of the water is approximately 5^oC and the temperature of the ship is 12^oC, Equation 3.3 gives 10.4 μm and 10.2 μm, respectively. The wavelength of maximum exitance for both the ship and the surrounding ocean falls within the LWIR region, indicating that the majority of the radiation in the scene falls in this thermal band as well.

For military and surveillance uses, it has been accepted that MWIR imaging yields the best results for imaging and detection of vehicles, ships, and aircraft due to the increased sensitivity to these objects [64]. The emissivity values for water and steel are 0.96 and 0.16, respectively [80]. By combining Equation 3.4 and Equation 3.5, an equation for the total radiant exitance for a greybody is found, $W_{obj} = \varepsilon\sigma T^4$. Therefore, the total peak exitance for the surrounding ocean water and the ship is found to be 325 W/m^2 and 60 W/m^2, respectively. Based on this calculation the surrounding water could easily be assumed to dominate the energy received by the sensor. However, according to Equation 3.7, an object with a low emissivity value

(a)

(b)

(c)

Figure 3.5: A comparison of a) an optical image with b) a medium wave, and c) a long wave infrared image of a ship.

has a high coefficient of reflectance. Recall from Equation 3.8 that an infrared imager does not receive the temperature of an object, but instead the energy of the scene. For example, a steel sheet with a piece of plastic tape ($\varepsilon = 0.95$) fixed to it have the same measured temperature. If the steel and the plastic are warmed to a higher temperature than the surroundings, the plastic will appear much brighter in the infrared image than the steel. Conversely, if the set is cooled below the temperature of the surroundings, the plastic will appear much darker than the steel. Despite the temperature of both the plastic and the steel being equal, since the emissivity of the plastic is higher, meaning it is an efficient emitter, and the emissivity of steel is low, the plastic will more closely indicate the actual temperature of the steel surface. The radiation received from the steel is a better indicator of the background temperature since the steel is reflecting the background radiation. Therefore, since the surrounding water in Figure 3.5 has a higher emissivity value than the ship, and the surroundings are warmer than the water, the water represents the target temperature better than the ship. Further, the steel ship gives a better indication of the background temperature since it has a high reflectivity value (recall Equation 3.7), and is therefore reflecting the infrared radiation from surrounding sources such as the land and the sun. This idea is further shown in Figure 3.6 of a fiberglass kayak in the ocean. It would be expected that the kayak would be approximately the same temperature as the air/water interface. However, the kayak, with approximate emissivity of 0.75, is much more prominent than the background. Emissivity is not a simple material property, however, especially since factors such as the shape, and viewing angle change the emissivity of an object.

Figure 3.7 presents a set of images of a small boat travelling through the scene. Comparing the medium wave and long wave infrared images, Figures 3.7b and 3.7c, respectively, with the corresponding optical image, the wave patterns seen in the optical image are still found in the medium wave infrared image. Blurring of the
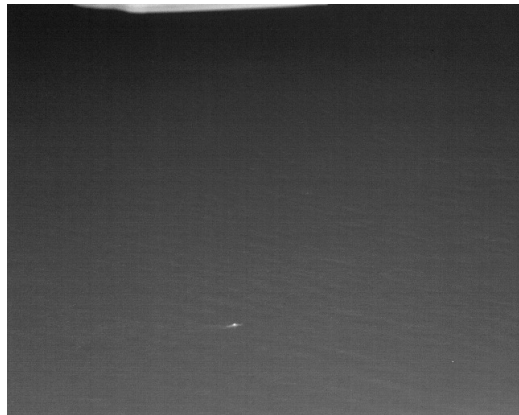
Figure 3.6: A comparison of an a) optical image with b) a medium wave, and c) a long wave infrared image of a kayaker.
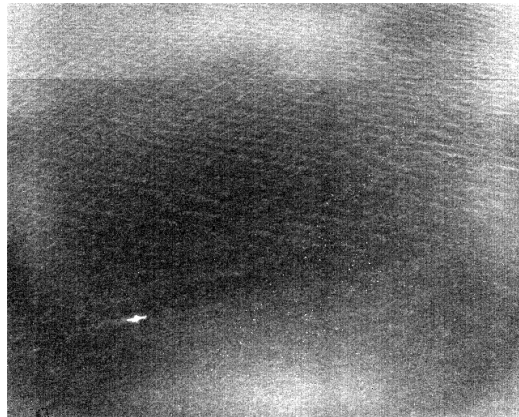
(a)
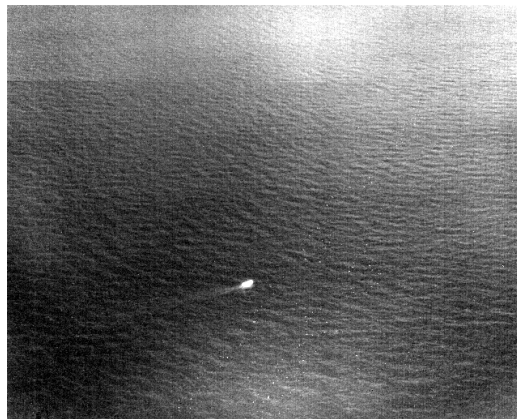
(b)
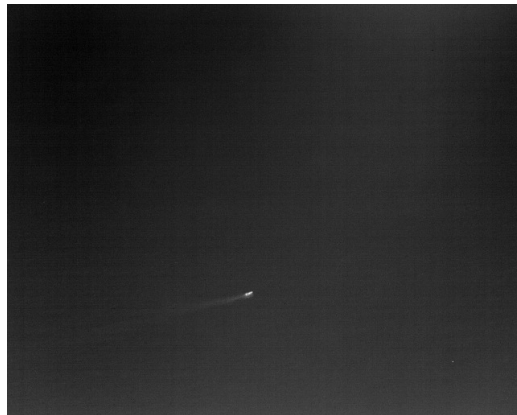
(c)

Figure 3.7: A comparison of a) an optical image with b) a medium wave, and c) a long wave infrared image of a small boat.

image in the long wave infrared image due to a longer integration time is the cause of the reduced sharpness. If we assume that the aircraft speed is 60 knots, and the integration time for a single frame for the FLIR Photon640 is approximately 10 ms, then during the collection of radiation for a single image, the aircraft moves slightly over 30 cm. For comparison, if the FLIR SC5000 has an integration time of 10 μs, then the aircraft movement during the imaging process is approximately 3 mm. If the height above sea level of the infrared imager is 150 m, with a FOV of 26° x 20°, the iFOV is 10.8 cm/pixel x 10.3 cm/pixel. So for each frame of the recorded infrared image for the Photon640, each pixel in the image would actually be an average of a ground area equal to approximately 10 cm x 40 cm. Moreover, if the altitude is increased to 600 m above sea level, the iFOV becomes, 58.6 cm/pixel x 43.0 cm/pixel, then the ocean area averaged during a single frame is larger than 0.3 m^2.

Reflection of sunlight on the ocean surface creates many problems in image processing for detection or tracking in optical and infrared images. Figure 3.8 presents an image set where a small boat is travelling directly through the reflected sunlight. In both the optical and medium wave infrared image, Figure 3.8a and 3.8b, the reflection of the sun saturates approximately half of the imaged scene. In particular, the target in the MWIR image is much less visible than previously seen. However, in the LWIR image, Figure 3.8c, reflected sunlight is not apparent in the image, with the target to background contrast quite good. Solar interference is noted as a problem in visible band and medium wave infrared cameras [65]. In the long wave infrared band, solar rays are diffusely reflected from the water surface. In fact, one of the major advantages of LWIR sensors is the uniform signal in most conditions, both day and night [77].

Reflections from objects has a significant effect on the appearance of a thermal profile [76]. It was demonstrated that for a 17°C object, the received radiation in

(a)

(b)
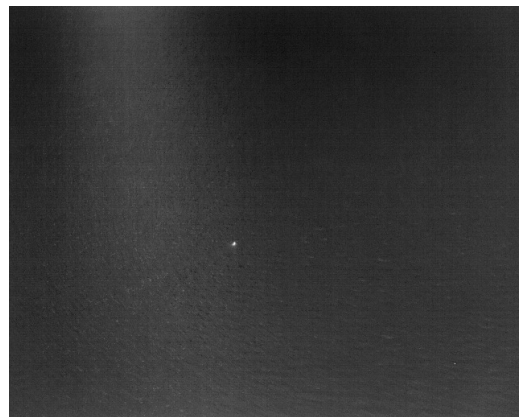
(c)

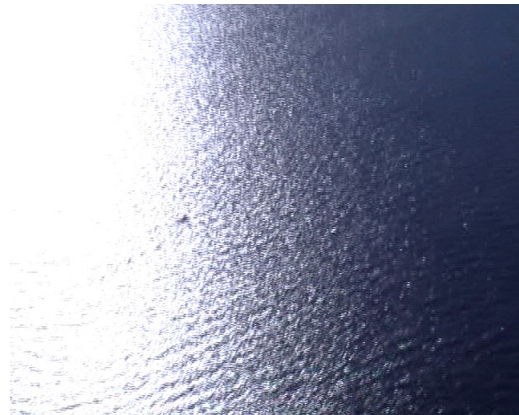Figure 3.8: A comparison of a) an optical image with b) a medium wave, and c) a long wave infrared image of a small boat travelling in an area of direct sunlight reflection on the ocean's surface.

the MWIR band was 24 W/m^2 from reflected solar radiation, and 4.1 W/m^2 from the emission of the blackbody. Conversely, in the LWIR thermal band for the same object, the reflected solar radiation at ground level was 1.5 W/m^2, whereas the emitted radiation was 127 W/m^2. The sunlight is nearly negligible in the LWIR band, whereas in the MWIR band it dominated the received signal [81]. However, the thermal contrast of this scene, arising from temperature variations and differences in emissivity, will be larger for in MWIR [76] (An image demonstrating this concept is shown in Chapter 6). In the medium wave infrared image the pavement, $\varepsilon = 0.90$ - 0.98, has a very high contrast when compared to the surrounding trees and grass, whereas in the long wave infrared image the contrast is not as large.

Figure 3.9 shows an image of a cliff near the edge of the ocean. This is a more complex scene than has been presented in the previous images with respect to the wider temperature range. With distinct levels in the range of [0, 16,383] for a 14-bit image, the number of discrete bins can be much larger than an 8-bit image format. Figure 3.10 presents the histograms of the thermal images in Figure 3.9. The histogram in Figure 3.10a is the original histogram of Figure 3.9b before histogram adjustment. The intensity values range from 4706 to 7935, with all 3229 bins filled. From Table 3.1, the NETD of the SC5000 is 20 mK, which gives an approximate temperature range in the scene of 64.6^{o}C. The large temperature range in this image is due to higher apparent temperatures of objects. It should be noted that for the histograms here, the range of the x axis is [0 65535], which corresponds to a 16-bit image, due to image storage standards. The range of intensity values is better seen in Figure 3.10b. The corresponding histogram for the long wave band image is given in Figure 3.10c. In this case, each of the 255 bins are filled.

(a)

(b)

(c)

Figure 3.9: A comparison of a) an optical image with b) a medium wave, and c) a long wave infrared image of the side of a cliff near the ocean.
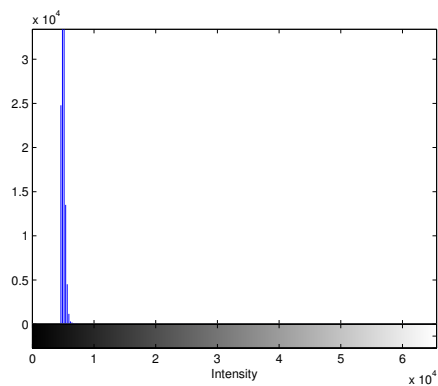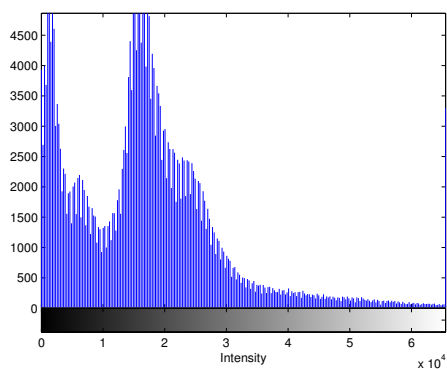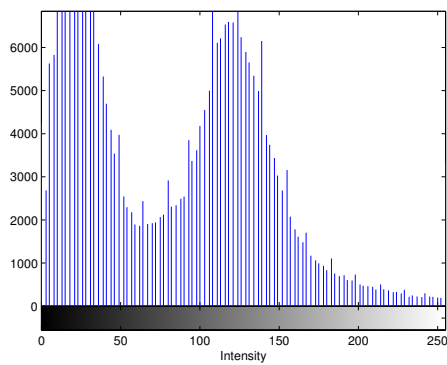
Figure 3.10: A comparison of the histograms of the a) medium wave, b) the adjusted medium wave, and c) the long wave infrared images presented in Figure 3.9.

3.5   Conclusions

The thermodynamic background of infrared thermal imaging was presented. The physical relationship between theoretical blackbodies and real surfaces was described, concluding that the majority of the radiation emitted from the surface of the ocean will be in the LWIR spectrum. Using a radiometric chain technique, an equation for the infrared radiation of a real scene was derived. Thermal infrared imaging devices and the factors which affect the resulting image quality were discussed, relating to the physics of the detectors, platforms, and scenes. The selection of a long wave infrared sensor for the application of thermal wake detection was summarized, comparing data collected for medium-wave and long-wave infrared imaging devices from a low altitude aircraft platform. Notably, since the thermal wake patterns of the semi-submersible vessels are expected to differ in temperature from the surrounding water by less than 1°C, an imager with a low NETD value, less than 50 mK, is required. It was also determined that 8-bit data is sufficient for thermal wake detection.

Chapter 4

Development of an Algorithm to Detect Sub-Surface Vessels Using Infrared Imagery

4.1 Introduction

Detection of surface traveling vessels based on wake patterns in synthetic aperture radar images have been well investigated since these wake patterns were first noted in images from SEASAT in 1978. It has been demonstrated that the detection of wake patterns is advantageous since wake patterns are much larger and more distinct, as compared to the hull of a ship [48]. Further, wake detection yields a better estimate of the ships location, as well as estimates of moving ship parameters and hull characteristics [48, 51, 52]. The detection and registration of ship wakes in synthetic aperture radar has improved the probability of detection and reduced the false detection of vessels. Transformation-based algorithms, such as Radon transform, have proven to be most successful in wake recognition. These algorithms accentuate straight line

features in an image, through integration of the intensity along all directions in the 2D image space. This integration process also tends to cancel noise, resulting in a greater signal-to-noise ratio in the transform image [53]. Currently, Analysts' Detection Support Systems, to automatically detect ship wakes, are being applied to guarantee consistency due to the extensive amount of data collected in short periods of time, and the substantial amount of open ocean in the captured imagery [46].

The density of water is dependent on temperature in a non-linear relation, such that the density increases as temperature decreases, to a maximum density at approximately 0^oC for seawater. This density-temperature relationship, coupled with surface heating and the earth's rotation creates what is known as a permanent thermocline, a water region in which the temperature drastically declines from the surface to about 1000 m, with net temperature differences of up to 20^oC [82]. The disturbance of the propeller rotation and the vessels' hulls in the deeper, colder layers manifests to the surface due to the upward motion of the disturbance, and is further promoted by the upward travel of bubbles within the turbulent cloud [28]. An agreement between numerically modelled and experimental thermal wake patterns created by the turbulent water motion behind a ship during both day and night has been reported [23]. Predictions using numerical simulations found that during the night, a warm water wake, attributed to a lack of surface heating, could exist [23]. Thermal wake temperatures were reported to be approximately the same as that of the water at the keel of the ship [7]. Moreover, a theoretical bases for the infrared detection of a submerged vessel was reported, experimentally confirmed through measurement of a temperature differential of 3^oC of the wake with the surrounding water in a wave tank, equivalent to the temperature stratification in the tank [24, 25]. Further theoretical support for thermal wake detection was also reported [26, 27, 83]. The persistence of the cold water disturbance was noted to exceed 2 minutes [26]. A comparison of mid wave

infrared (MWIR) and long wave infrared (LWIR) images of a wake created by a ship revealed a dark wake pattern in the mid wave infrared image, and a bright pattern in the long wave infrared image. This was attributed to strong surface reflection in the slick-like wake area [28]. For a ship moving at a steady rate with a warm ocean surface layer, and a stratification temperature difference in the first 10 meters of 1°C, the wake contrast was found to be significant [29]. Finally, the first observations of the thermal footprint using infrared imagery resulting from the tail fluke of a whale was reported. It was noted that trails existed up to 300 m behind humpback whales, with an estimated swimming speed of 2.4 m/s, equaling a thermal trail persistence of about 2 minutes [34].

In this work, the development of a real-time image processing algorithm for deployment on a small unmanned aircraft system, in the vast ocean corridor of North America is outlined. The deployment platform imposes restrictions on the available payload size and power, while still requiring full frame rate, real-time operation of the system. Prominent thermal wake patterns in long wave infrared images, captured with a FLIR Photon640 are presented. Cold water scarring of the surface is confirmed during normal day-time operations. Warmer water wake patterns were noted, attributed to a lack of surface heating [68]. Temperature differences were found to be consistent with the measured temperature profile using Vemco Minilog II temperature loggers for each data set. Image processing techniques are compared to accentuate these wake patterns for the observer. Finally, results from a custom algorithm, designed to detect the thermal wake patterns from a small unmanned aerial platform with limited payload capacity are presented for both warm and cold water wake patterns.

4.2 Experimental Design

A FLIR Photon640 camera was installed on the inside of a specialized mount on a Piper Cherokee Six aircraft aimed straight downward. The FLIR Photon640 images were collected in an 8-bit TIFF format at 9 frames per second. The infrared imager was fitted with a 25 mm lens (hFOV 26° x vFOV 20°) [84]. Wake patterns were created by a 7.5 m boat (Everglades 24 243cc) with propeller at approximately 2 m below the surface. This vessel was chosen based on a hull size and propeller depth similar to that reported for self-propelled semi-submersible vessels, which travel just below the surface of the water [15]. Data was collected over two days in San Diego, California in an area over the Pacific ocean due west of Scripps Pier, in the La Jolla area. Images were recorded a minimum of 300 m from the shoreline, and any images of land were removed manually.

Temperature measurements were recorded using five Vemco Minilogger temperature recorders. The loggers were suspended from a large buoy at depths of 0.08 m, 0.51 m, 1.07 m, 2.03 m, and 3.86 m below the surface. The temperature loggers were set to record at one second intervals during each deployment, and the temperature data was averaged over the time in the water after reaching a stable temperature, determined visually as the ranges with a linear slope of approximately zero. Note that the time constant of the mini loggers is 150 s.

4.3 Results & Discussion

4.3.1 Data Set 1

Weather data for this set is presented in Table 4.1, with no notable ambient conditions. Infrared images were recorded at a height of 150 m above sea level. Average

Table 4.1: Ambient weather conditions during data collection periods, from NOAA station 9410170 off Scripps Pier in San Diego, California.

Measurement	Set 1	Set 2
Minimum Temperature	9.4 ^{o}C	11.7 ^{o}C
Maximum Temperature	21.7 ^{o}C	23.9 ^{o}C
Mean Temperature	13.5 ^{o}C	16.3 ^{o}C
Precipitation	No	No
Visibility	14.8 km	14 km

temperature measurements during two times of deployment are shown in Figure 4.1. In Figure 4.1a, a temperature difference of approximately 1°C was found between the surface measurement and the lowest temperature logger at approximately 4 m below the surface. It is also notable that the top two temperature loggers (at 0.08 m and 0.51 m) were approximately the same temperature, with the remaining temperatures measured decreasing with increasing depth, as expected. Figure 4.1b presents the temperature measurements taken with the loggers deployed into the thermal wake behind the boat. As expected, the measured surface temperature is lower than the water just below it. Due to the thermal constant of the temperature loggers, an immediate temperature measurement was not reliable. Instead, these measures were averaged as the wake developed, which could potentially explain the smaller than expected temperature differential at the surface. Figure 4.2 presents a stitched image of the thermal wake-based on the GPS position of each sub-image. The total length of the wake is determined to be over 215 m long, with the width growing from approximately 2 m, to approximately 6 m towards the end of the wake.

A sample image of a wake pattern is shown in Figure 4.3. The mean pixel intensity value in the thermal wake region was 57, and the remaining background mean pixel intensity value was 88. This was determined to be an approximate 1°C temperature
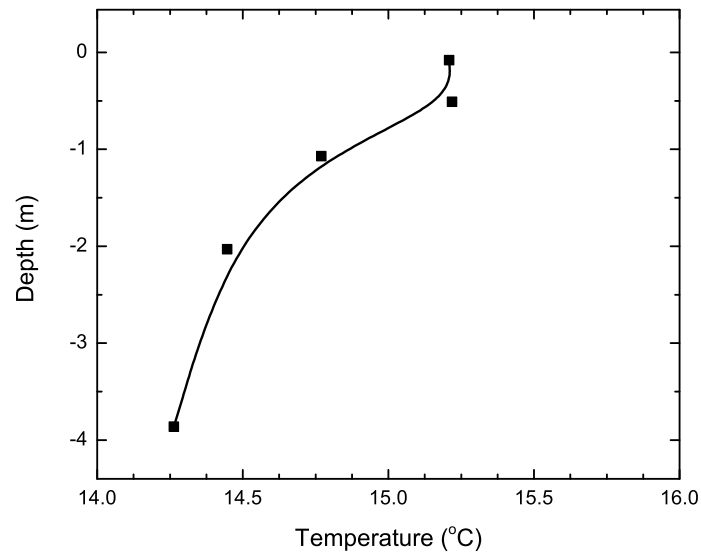
(a)
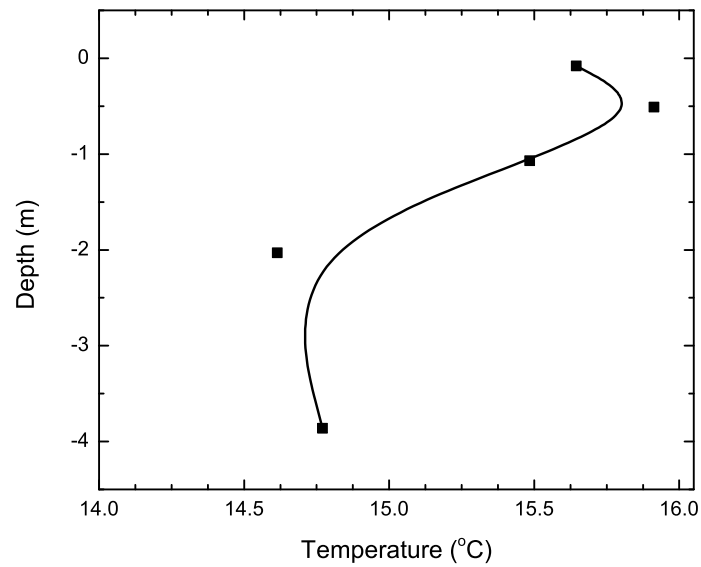
(b)

Figure 4.1: Temperature profile of a) deployment 1 of the Minilog recorders over the side of the stationary boat near moored targets, and b) deployment 2 of the Minilog recorders into the boat's wake during data collection. Trend lines are added to accentuate the data relationship. Note that there is approximately 90 minutes between Deployment 1 and 2.

Figure 4.2: Stitched infrared images of the thermal wake created by a 7.5 m boat travelling on the surface of the ocean at 10 km/hr from 150 m ASL. The wake was found to be 215 m long.
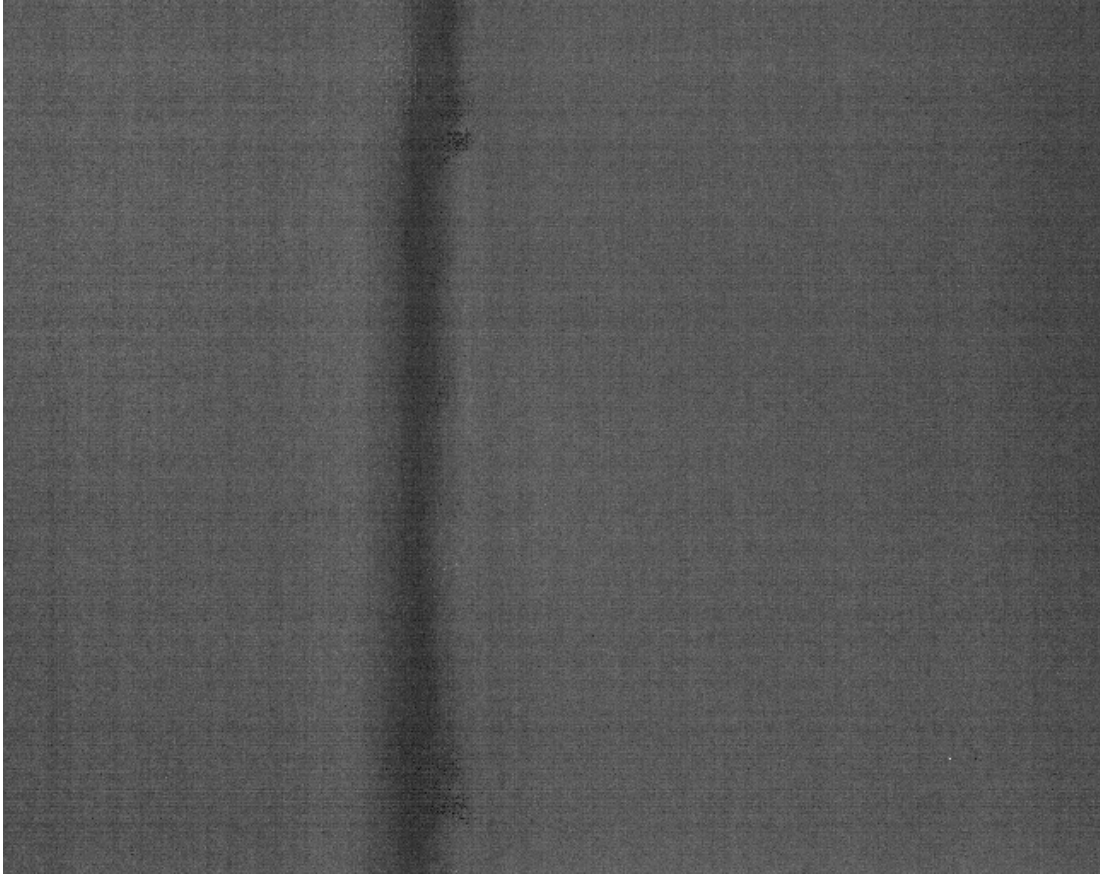
Figure 4.3: Thermal trail from a 24 foot boat collected from 150 m ASL using a LWIR camera. Approximate field of view is 69 m x 52 m.

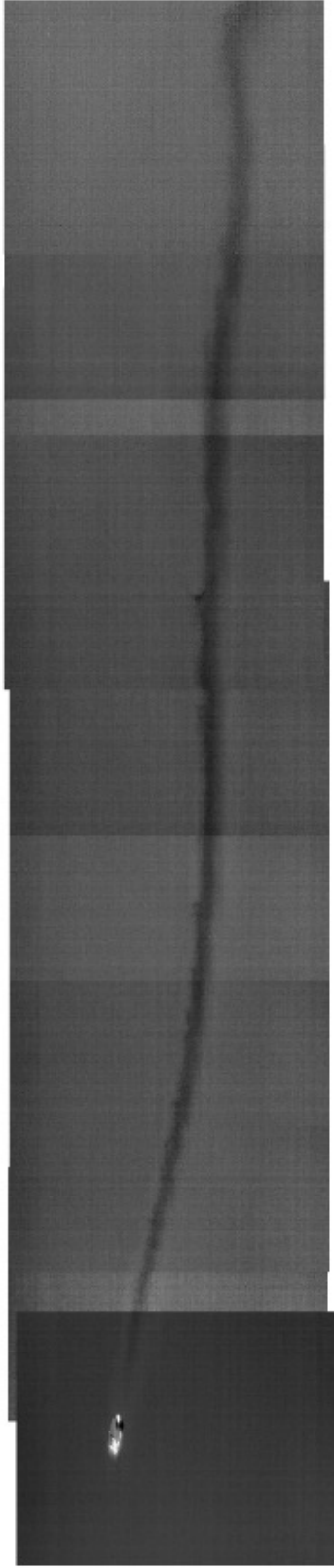difference, which is consistent with the measured range in temperature difference in the top 4 m of water in the testing area, shown in Fig. 4.1. It is also notable that the total range of pixel intensity value in Figure 4.3 is only 35% of the total available pixel intensities in the image. This low contrast is due to the small temperature variation between the thermal wake region and the surrounding water.

4.3.2   Data Set 2

Weather data for this set is presented in Table 4.1. It is notable that a marine layer was present over the area from Del Mar to Mission Bay from early morning until early afternoon, at which time the tests began. The two deployments of the Minilogger recorders are highlighted in Figure 4.4. The logger at the deepest position malfunctioned, resulting in no usable data. In Figures 4.4a and 4.4b the temperature differential between the surface and the lowest logger is much different than was present in Figure 4.1. In particular, Figure 4.4b shows that the surface temperature is 0.2^{o}C colder than the lowest temperature logger.

Figure 4.5a presents an infrared image collected from 600 m above sea level. The thermal scar created by the propeller motion is less distinguishable than presented in the previous section. More importantly, the trail is lighter than the surrounding water, signifying that it is warmer. This can be attributed to the presence of a marine layer through the morning which limited the direct sunlight and therefore the source to heat the surface. Therefore, the differential in temperature in the top 4 meters of the ocean was not large enough to create a significant thermal scar. The presence of a thermal scar warmer than the colder surrounding water was previously predicted through simulation to be possible during the night [23].

In an attempt to further discriminate the warm thermal scar from the surrounding ocean water, two methods were attempted. Figure 4.5b presents the resulting image
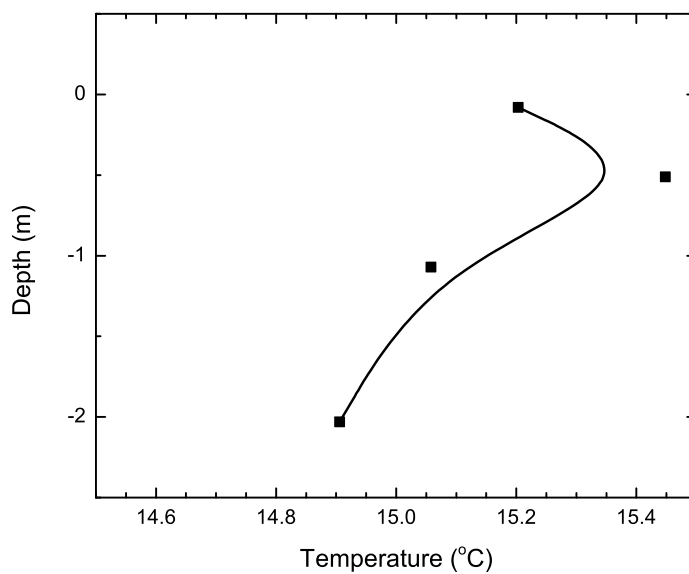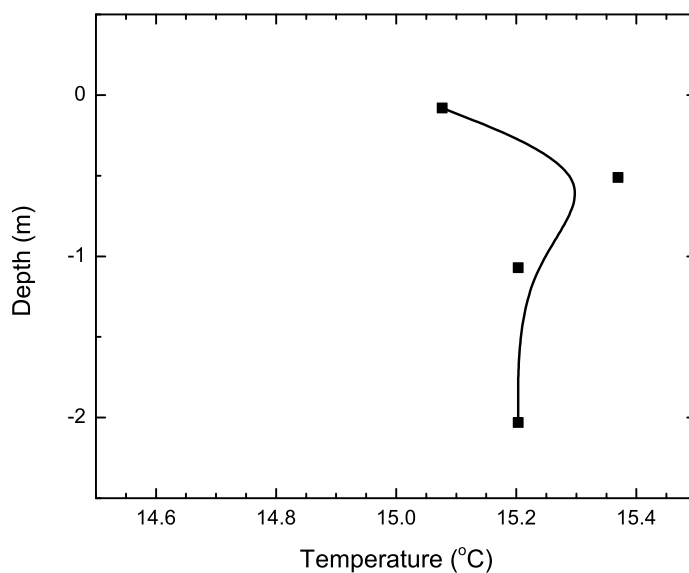
Figure 4.4: Temperature profile of a) deployment 1 of the Minilog recorders over the side of the stationary boat near moored targets b) deployment 2 of the Minilog recorders into the boats wake. Note that there is approximately 30 minutes between Deployment 1 and 2.

where a mean image was calculated from a set 101 images captured around the original image. This mean image was then subtracted from the original image. The resulting image, presented in Figure 4.5b, is shown after a histogram equalization is performed. Figure 4.5c presents the same image as Figure 4.5b cropped from a resolution of 644 x 512 pixels to 161 x 128 pixels for comparison with the images captured at 150 m above sea level. This method results in an image with additional noise compared to the original image. However, the thermal wake pattern in the image is much more accentuated than the original. Further, it should be noted that the thermal wake trail is approximately 50 m, shown in Figure 4.5b.

The second technique averaged the pixels corresponding to the same location, since both the altitude and the speed of the aircraft are known. The original image is shown in Figure 4.5d. By cropping the input images to 161 x 128 pixels, and shifting the frame by the approximated vertical pixel change per frame, an average image was created, presented in Figure 4.5e. Figures 4.5d and 4.5e are then subtracted, to give Figure 4.5f. It is notable that Figure 4.5f is presented after a histogram equalization is performed. Averaging the pixels based on location resulted in an image where the wake is prominent, with little to no noise in the background, shown in Figure 4.5f. The resulting image, however, does not contain a wake pattern as prominent as Figure 4.5f. This is attributed to the fact that the intensity difference between the wake pattern and the surrounding water was small enough that the when the original is subtracted from the averaged image, the further reaching thermal wake was also removed.

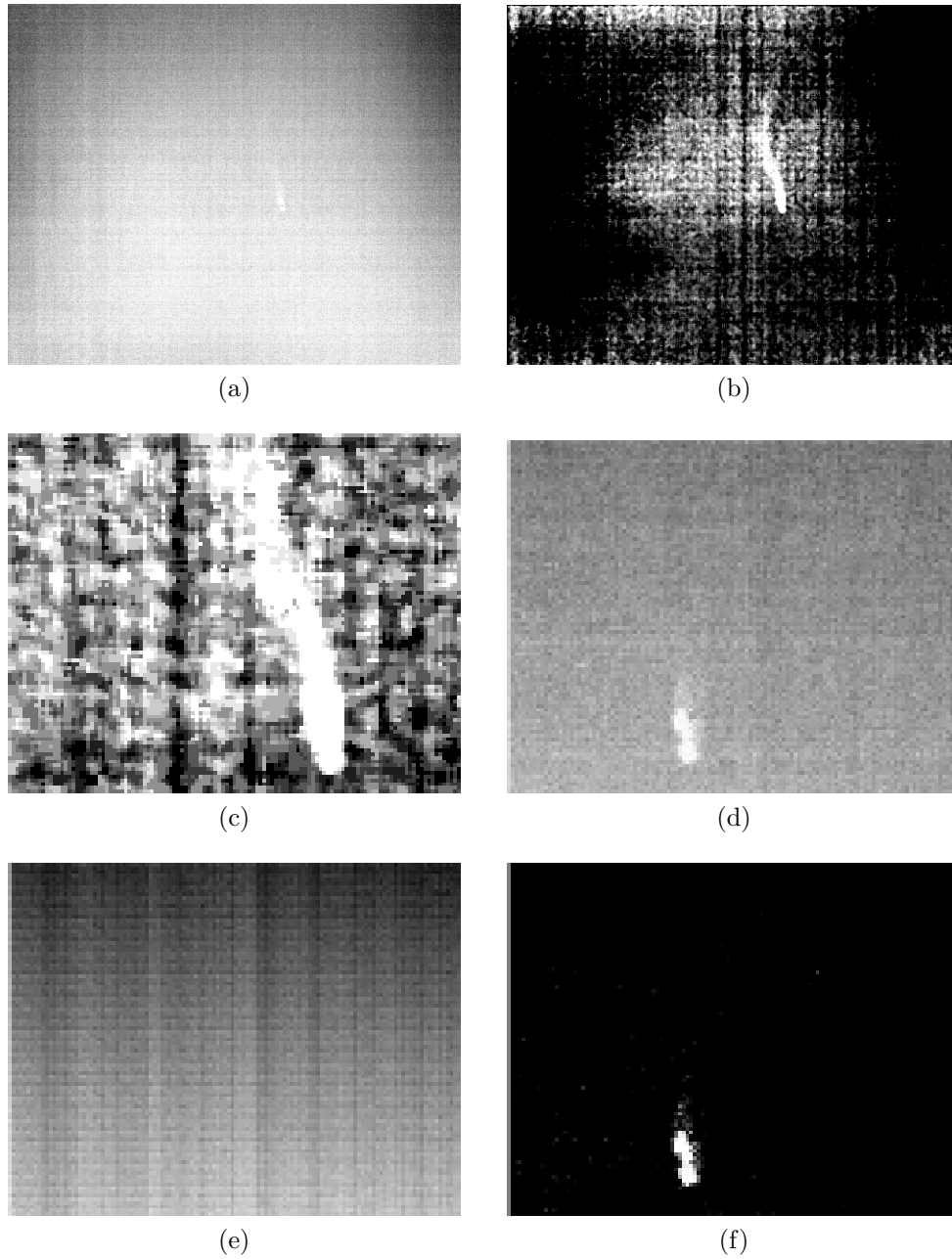Figure 4.5: a) Infrared image of a thermal wake pattern from 600 m ASL (Approximate field of view is 277 m x 212 m.), b) image after subtracting averaged image, c) resulting image cropped to a field of view of approximately 69 m x 52 m. d) Cropped infrared image of a thermal wake pattern, e) resulting image from averaging pixels at the same location over 36 frames, f) image created by subtracting averaged image from original image.

4.4   Real-time Algorithm Development

The current image processing algorithm for implementation on a small unmanned aerial system for detection of thermal wakes is presented in Figure 4.6. The original image is shown in Figure 4.7a. Since the image is taken during the daytime, the inverse of the image is taken, and then a median filter is applied to the entire image to reduce the noise without blurring the edges. Next, in preparation for the creation of a binary image, a global normalized intensity value is computed using Otsu's method. This value is added to a small constant, currently 0.05, to create a binary image, shown in Figure 4.7c. Next, morphological operations are applied to remove the small objects, then to fill any small holes. The result of the morphological processing is presented in Figure 4.7d. Finally, a Hough transform is applied to calculate the longest line in the image, where the Hough parameter space plot is shown in Figure 4.7e, and the longest line segment is represented in Figure 4.7f. Overall, for a single image, this process requires approximately 0.17 seconds to process.

This algorithm has been tested on the data sets described above, which totals 15,223 images, with a false detection rate lower than 10%. The data set with the wake appearing warmer than the surrounding water also performed well. The wake patterns are detected under most cases, using night mode, but not for as many sequential frames. This occurs since the thermal scar is not as prominent in the image, partly due to the smaller temperature differential, but also due to a much higher altitude (600 - 900 m ASL vs 150 m). The wake pattern could also become more distinct with newer infrared technology. A current limitation of this algorithm occurs when other long, straight objects, such as shoreline or piers are present. Further, if more than a single thermal trail occurred within the imagers FOV, the algorithm would only detect the longest thermal trail.
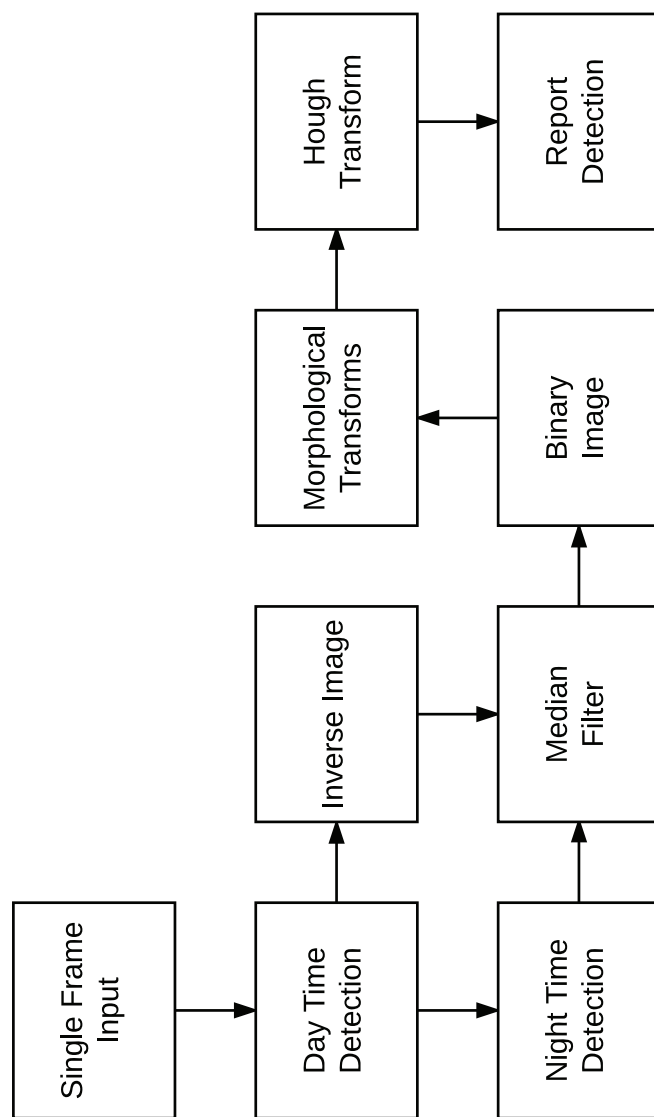
Figure 4.6: The current system algorithm developed for thermal wake detection.

(a)   (b)   (c)

(d)   (e)   (f)

(g)   (h)
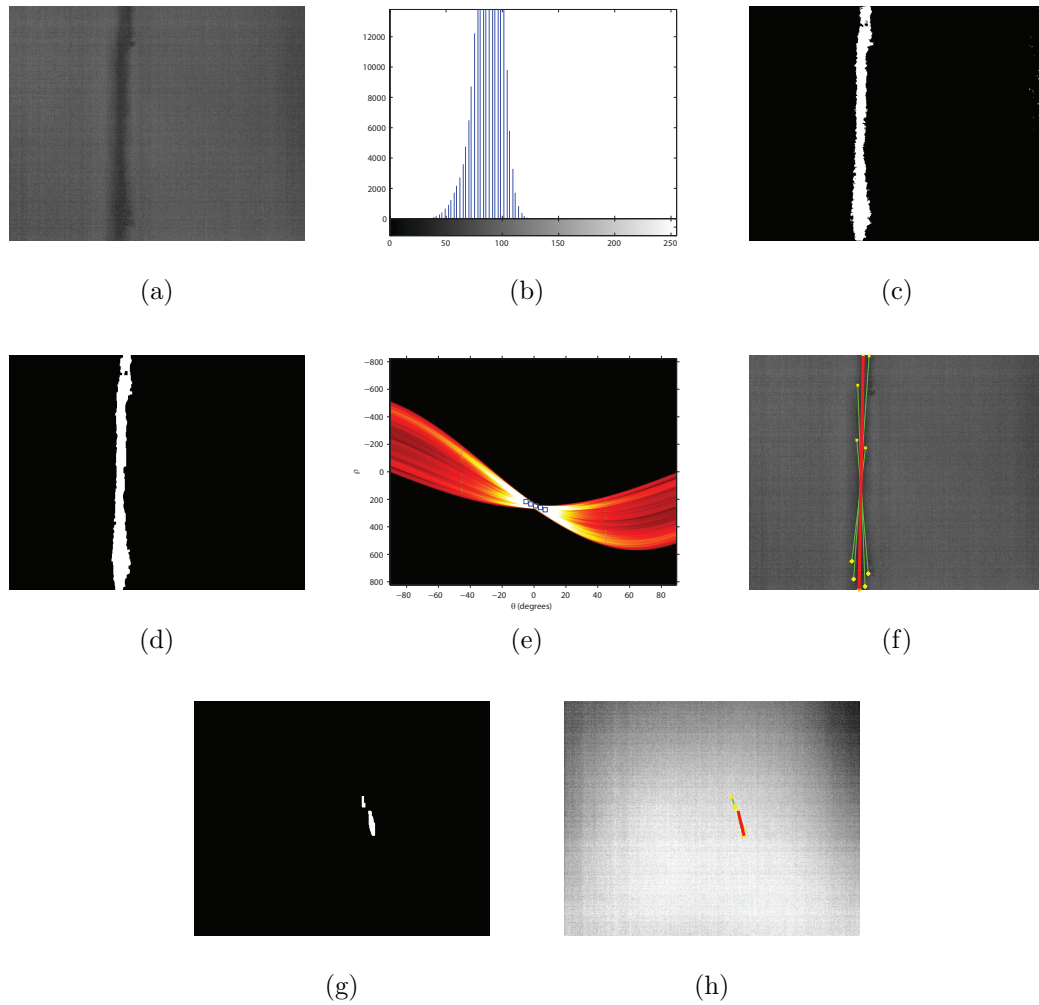
Figure 4.7: A demonstration of images at different stages of the algorithm, where a) presents the original image, b) is the histogram of the original image, c) is the created binary image, d) is the binary image after morphological transforms, e) shows the results of the Hough transform and f) shows the resulting detection. g) Presents the binary image of Figure 4.5a, and h) shows the detected wake pattern of (g).

4.5 Conclusions

The presence of submerged vehicles in the waters of North America poses a major threat. It was demonstrated that temperature measurements in the top 4 m of the ocean water under normal solar heating gave a stratification with a differential of approximately 1°C. Moreover, when deployed into the wake pattern, the surface temperature was found to be lower than the water just below it. Without the availability of solar heating due to ambient conditions, a warm wake pattern was noted, consistent with previously reported predictions from numerical models [23]. Finally, an image processing algorithm using a Hough transform to highlight the longest line segments in the images was presented. It was shown that this algorithm can distinguish the wake patterns from the surrounding water in the long wave infrared images.

Chapter 5

Autonomous real-time infrared detection of sub surface vessels for unmanned aircraft systems

5.1 Introduction

Thermal imagery of the disturbed colder water layers, driven to the surface by the vessel will allow for the detection and interdiction of the semi-submerged illegal traffic. A completely autonomous system, including on-board processing for the smart recognition of a radar eluding, low profile vessels is presented. This smart system could potentially be coupled with airborne automatic identification system to aid in the discrimination of legal and illegal marine traffic. Further, the ability to have multiple UAs monitoring adjacent areas would aid in the follow-up mission to decrease false alarm rates and increase the percentage of detected illegal vessels.

Infrared imaging devices with a high resolution, a high responsivity, and a very low minimum resolvable temperature will be required to provide high quality imagery

for airborne detection of the thermal wake. IR signatures of ship wakes are highly variable in both persistence and temperature contrast as compared to the surrounding surface water, depending on both meteorological and oceanographic parameters [7]. These systems will require further development to both increase durability, and reduce weight for housing in small UA.

An unmanned aircraft with an integrated payload allowing the automatic detection of illegal traffic will greatly reduce the required resources for the detection of these self-propelled semi-submersibles (SPSS), as well as increase the number of interdicted vessels. The threat of these vessels cannot be understated; payloads from drugs to weapons of mass destruction could be housed in these small SPSS. An increased detection of this illegal traffic is required for national security both in the ports along the coastlines of Canada, as well as the rest of North America.

There is no reported work on development of smart IR systems for detection of the thermal wakes of submarines. However, integration of IR devices into commercially available computer vision technologies are used in applications such as quality control applications [8], oil slick thickness detection [9], and critical temperature measurements of machinery [10]. In these applications, IR imagers have proven to be very effective, boasting multiple benefits over other technologies, including boosting efficiency and reducing costs. In particular, surveillance imaging systems with detection and tracking capabilities over complex terrain have been developed and have been demonstrated to be successful [11–13].

5.2 UAS Payload

A payload system to mount a FLIR A65 long wave infrared camera and GoPro Hero2 optical camera for autonomous data collection was developed. An overview of the

Table 5.1: Operating specifications for the FLIR long wave infrared imagers used for data collection in this study.

Device	FLIR A65	FLIR Photon640
IR Range	7.5 - 13.0 μm	7.5 - 13.0 μm
Detector	Vanadium Oxide	Indium Antimonide
Resolution	640 x 512	644 x 512
NETD	50 mK	50 mK
Integration Time	12 ms (typical)	10 ms
Frame Rate	30 Hz	9 Hz

operating specifications for the FLIR A65 are given in Table 5.1. The camera is mounted on an Arris Zhaoyun 3-Axis brushless gimbal with a custom carbon fiber mount for both imagers (see Figure A.1). This customized gimbal was designed to mount to the base of a Mugins 3M H-Tail TBM unmanned aircraft platform in the payload bay using a custom mounting system containing 16 vibration damping balls to reduce the vibration of the gimbal. The gimbal contains a Basecam SimpleBGC controller with an on-board inertial measurement unit (IMU), and allows full control over the tuning and program of the gimbal, as well as stabilization. It is noted that a 113 gram counter-weight was added to the outside edge of the gimbal frame (near the GoPro) to balance the gimbal.

To monitor and control the system during flight, a ground control station was fabricated containing 2.4 and 5.0 GHz links to the aircraft, and a display for real-time feedback. The architecture of the system is presented in Figure 5.1. A Zotac Nano computer was used to store the images collected by the FLIR A65, and the GoPro images were recorded on an SD card on-board the GoPro. Both the GoPro and the FLIR A65 were connected to 5.8 GHz transmitters for monitoring from the ground station. On the ground, two 5.8 GHz receivers received the signals from the air. The first was a dipole antenna attached within the ground station which works in the general flight area, in a spherical radius of 2 - 3 km. The second was a large
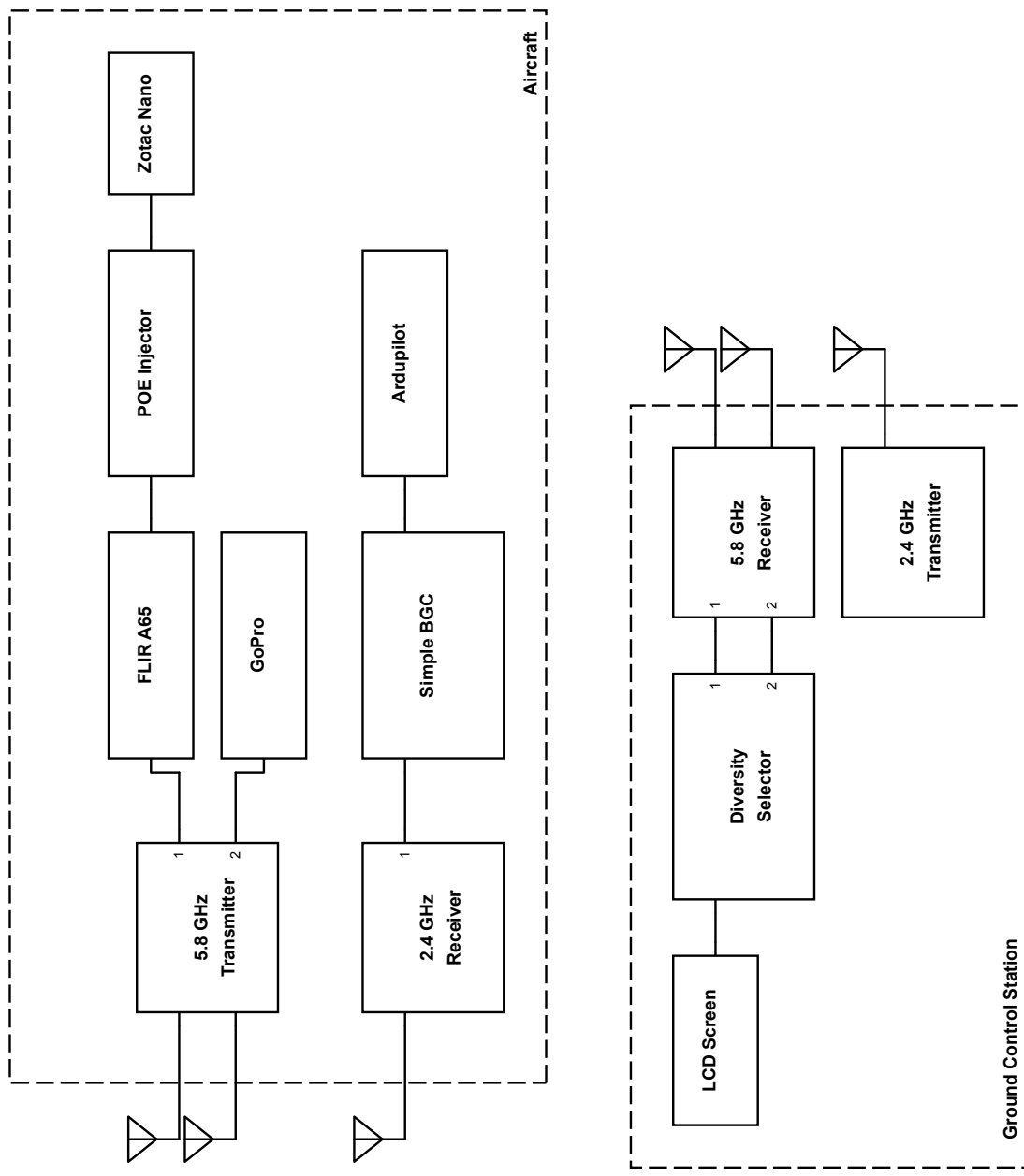
Figure 5.1: System architecture for data collection, camera monitoring, and control.

dish antenna with a 5 degree beam width attached to a telescopic mast, and raised approximately 5 m above the ground pointing in the general flight direction. Both antennas were attached to a diversity system which continually monitors the signal strength, and passed the strongest signal to the ground control station LCD screen. The 2.4 GHz transmitter in the ground station allowed for full control over the 3-axis gimbal during flight, with joystick control over each axis, or simple mode control. The gimbal was generally set to follow mode, in which the on-board IMU maintained a straight down view by compensating for aircraft motion. Finally, the Basecam IMU was connected to the Ardupilot autopilot system and was set up to record the approximate swath and projection of the infrared camera for syncing of flight data, including speed and GPS.

In order to test the system, and reduce the required resources for data collection and system tuning, a custom bracket was created to mount the stabilized gimbal system on a Manfroto tripod. This allows the system to be raised approximately 2 m above the ground. This system allowed for easy transport in a backpack, in particular for data collection in the strait between Bell Island and Portugal Cove, NL. Additional information and images of the systems described in this section are provided in Appendix A.

5.3   Transform Comparison

The extraction of image elements such as lines, edges, and curves is often a key step in image processing algorithms. Of particular interest for line detection is the Hough transform [85], previously reported for wake detection of SPSS [68]. In comparison, the majority of the reports of surface-based ship wake detection in SAR images leverages the Radon transform [86], reporting beneficial results [46]. In the following sections,

Table 5.2: Comparison of the false detection rate of minimally processed thermal wake videos for straight line detection using the Hough and Radon transforms.

Number of frames	Wake Type	LWIR Imager	False Detections Radon	Hough	Missed Detections Radon	Hough
243	Cold	Photon640	21	14	4	4
602	Cold	Photon640	88	79	3	3
186	Warm	Photon640	33	26	12	6
417	Cold	Photon640	20	14	2	2
823	Cold	Photon640	43	41	7	6
1436	Cold	A65	46	32	2	1
1224	Warm	A65	98	112	18	15

a brief introduction to the Radon and Hough transform are given. A comparison of the detection of thermal wake patterns is then summarized. Further theoretical comparison can be found in Appendix B.1.

To compare the Hough and Radon transform for thermal wake patterns, a script in Matlab [87] was created for each transform which subjected each transform to the same image by minimally processing the input data.

A set of seven videos containing thermal wake patterns was created as an input for the transform comparison. The set of test data contained three videos captured from an air-based platform in San Diego, CA as described in Chapter 4 and in Ref. [68], two videos for an air-based platform in Portugal Cove-St. Philips, NL as described in Chapter 3 and Ref. [84], and two videos were captured for a land-based, tripod mounted gimbal in Portugal Cove-St. Philips, NL. Each thermal wake video contained a minimum of 180 frames before and after the wake pattern. A summary of the test data is presented in Table 5.2. Figure 5.2 shows the Hough and Radon parameter space representation of the thermal wake image, as well as the corresponding processed images showing the detected feature.

Before applying the transform to detect the thermal wake pattern, a background estimation was done to remove any system-based noise and thermal non-uniformity

(a)

(b)

(c)
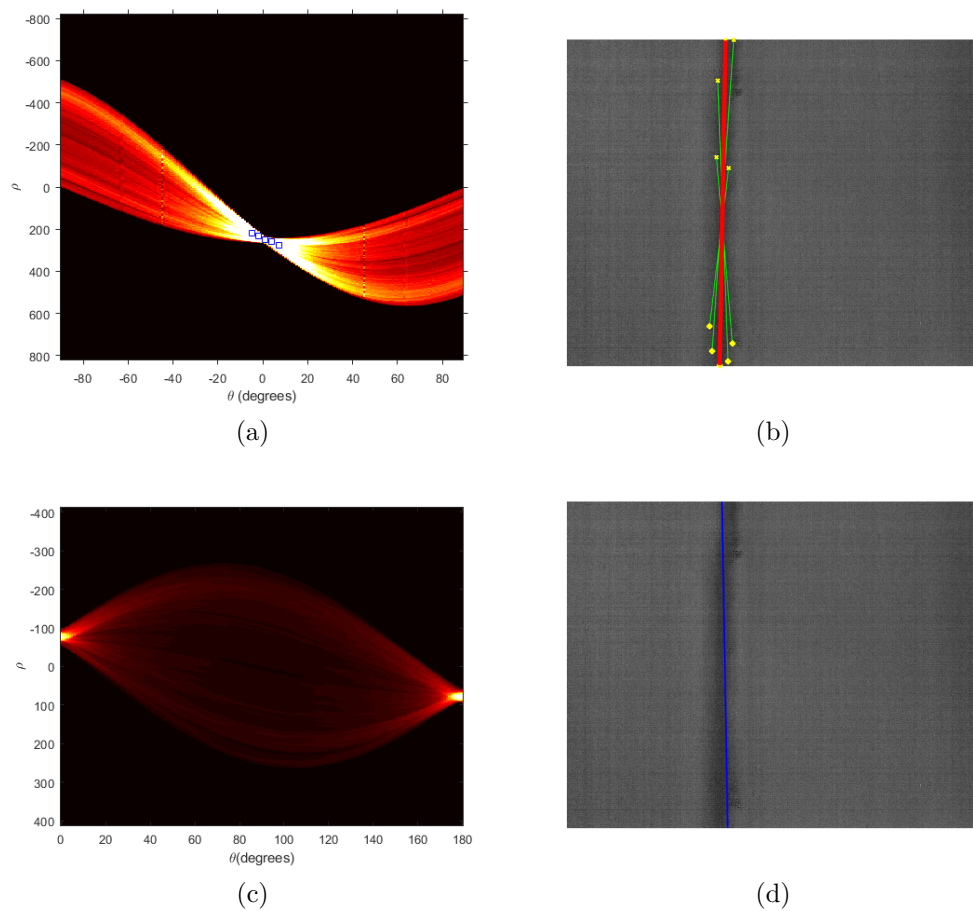
(d)

Figure 5.2: a) Hough parameter space representation of the thermal wake image. The boxes in the center correspond to points associated with the long lines. These lines are superimposed onto the original thermal wake image in b). c) Radon parameter space representation of the thermal wake image. d) Superimposed line corresponding to the detected straight line segment in the original image.

across the imaging system. This is done by averaging the first 30 images of each data set and subtracting the input image from the background estimation image. A median filter with a 5 x 5 neighborhood was applied to each image to remove salt and pepper noise in the image, before creating a binary image. Finally, a morphological open, to smooth contours and remove any small areas of noise, followed by a close was applied, to eliminate any openings.

The number of false detections and missed detections for the Radon and Hough transform for the data set is shown in Table 5.2, showing the Hough transform performed equal to or better than the Radon transform on the minimally pre-processed image in every trial except one. This data was determined manually by recording the output image and reviewing them.

A false detection was defined as a straight line segment being found in an image where no thermal wake pattern exists. The majority of the frames causing false detections were due to changes in the scene, such as a temperature non-uniformity in the ocean surface which would not be removed in the background removal step. The Radon transform showed a higher number of false detections, in particular in images where the amount of noise, in particular around the edges increased. It is expected that this could be removed with additional pre-processing, but was more susceptible to false detections due to noise than the Hough transform. For the warm water wake patterns the rate of false detections was also much higher. Using the Radon transform this false detection rate was 12.9% for warm wakes, compared to 7.7% for cold water wakes. Similarly, applying the Hough transform, this rate was 11.6% versus 6.4% for cold water wakes. This is attributed to additional noise in the image due to the smaller temperature difference between the surrounding ocean water and the wake pattern as compared to the warm water wake patterns. Finally, the percentage of false detections decreased for long wave infrared (LWIR) images recorded with the

FLIR A65, 5.6%, as compared to the percentage recorded with the FLIR Photon640, 9.2%. In general, less salt and pepper type noise was observed in the data for the A65 as compared to the Photon640.

A missed detection is a frame which does contain a thermal wake pattern that is not detected. Table 5.2 reveals that the number of missed detections is much lower than the number of false detections. Moreover, the majority of the missed detections were observed when the body of the vessel creating the wake pattern entered the frame. This caused a drastic shift in the thresholding value to create the binary image, as well as reduced the contrast in the image between the surrounding ocean water and the thermal wake pattern.

5.4   Real-time Algorithm Overview

The current image processing algorithm for detection of thermal wakes is presented in Figure 5.3. The input frame is initially subject to a time-sequential processing step, which routes the image to one of the pre-processing stages of the algorithm, or the detection procedure, to ensure that the algorithm can perform in real-time. More than 95% of the frames are used in the detection algorithm, while the remaining frames ensure the detection is robust and accurate.

5.4.1   Windowed Triple-Vote

The first pre-processing step of the algorithm sets the detection mode of the algorithm based on the expectation of a warm wake pattern or cold wake pattern, potentially inverting the grayscale image, adopting a mutli-frame windowed triple-vote process. This process is represented schematically in Figure 5.4, and in sequence with the real-time processing algorithm in Figure 5.3 (block $p1$). For each frame, the mean pixel
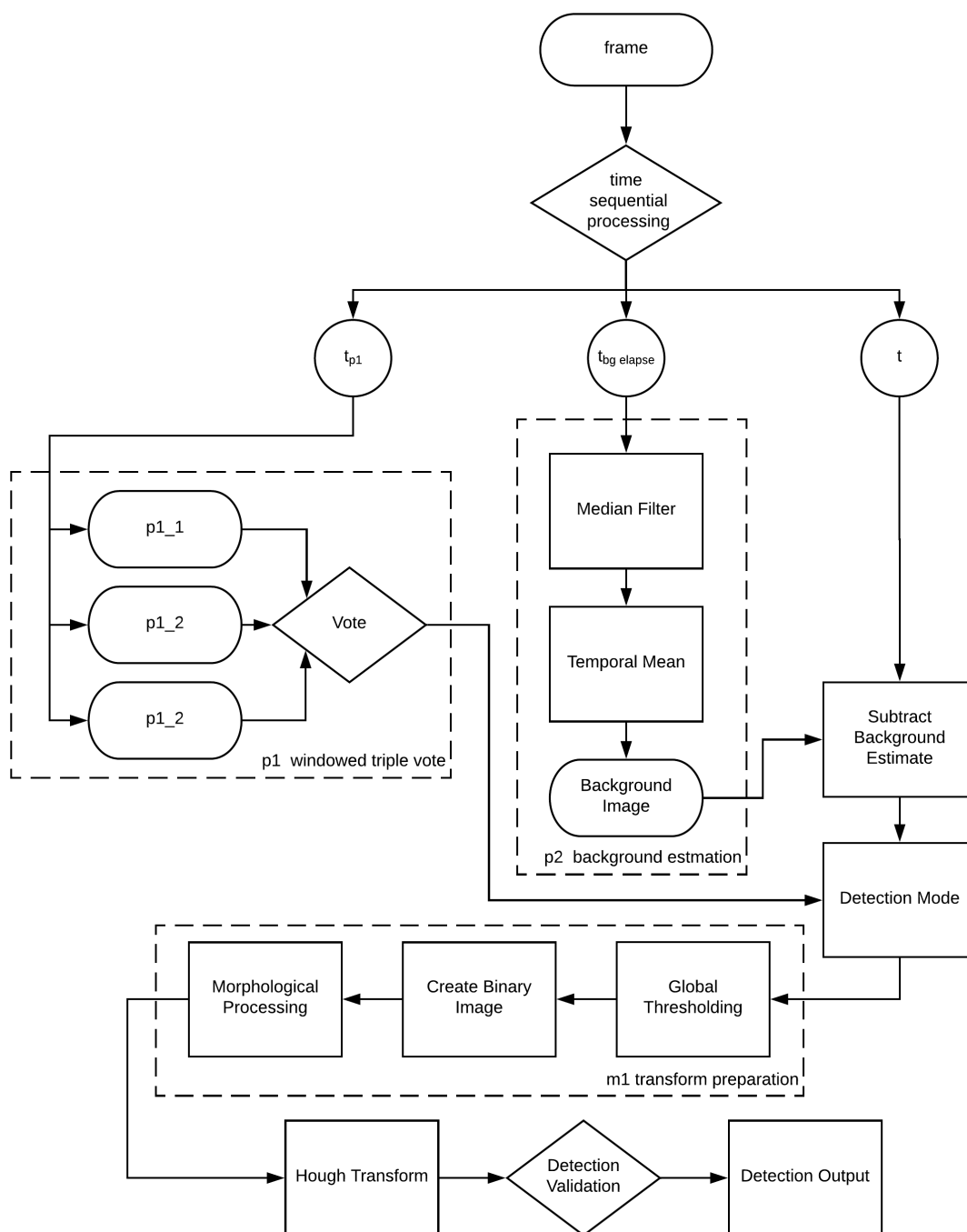
Figure 5.3: Schematic overview of the real-time infrared detection algorithm.
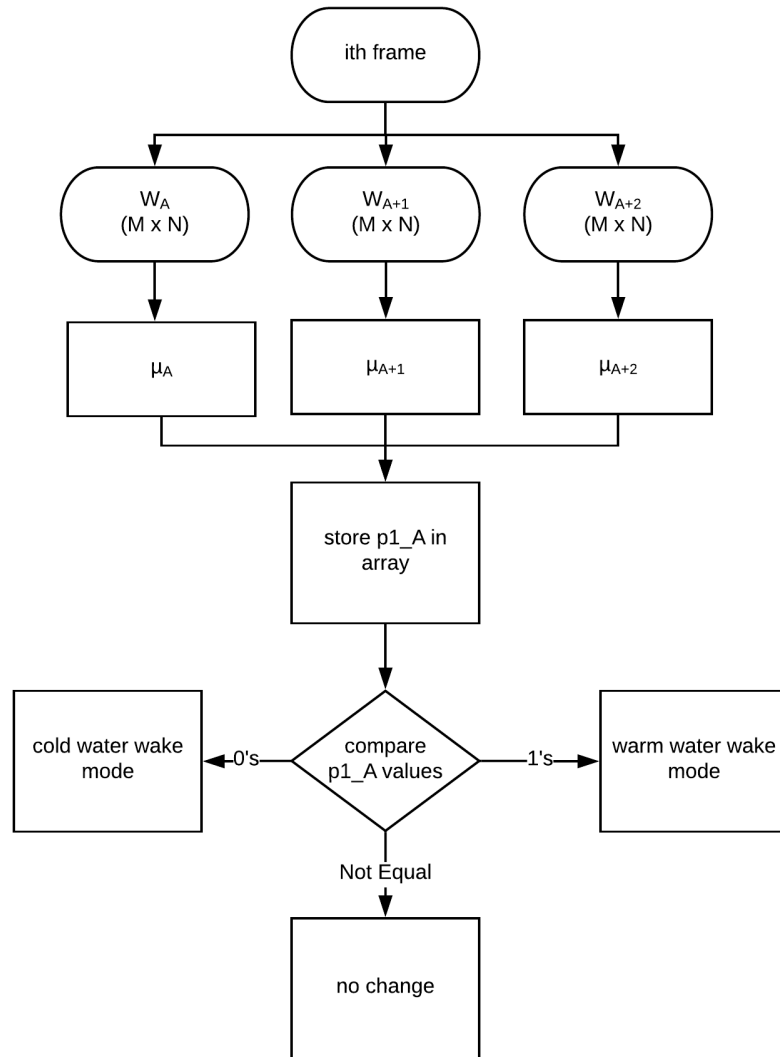
Figure 5.4: Schematic of the pre-processing step of the algorithm which determines the detection mode using a windowed triple-vote method in three frames spaced by time t_{p1}.

value, or average intensity, is determined in three window locations in the image as

$$\mu_A \;=\; \frac{1}{M \cdot N} \sum_{x=0}^{M-1} \sum_{y=0}^{N-1} W_A(x,y) \tag{5.1}$$

where M is the number of pixels in the x-direction, N is the number of pixels in the y-direction, A represents the window number, and W_A is the intensity value of the (x,y) pixel. The calculated values for μ_1, μ_2, and μ_3 are then used in the following equality

$$p1_A = \begin{cases} 0, & \text{if } \mu_A + \mu_{A+1} + \mu_{A+2} \leq I_{\mu_i} \\[2mm] 1, & \text{if } \mu_A + \mu_{A+1} + \mu_{A+2} > I_{\mu_i}, \end{cases} \tag{5.2}$$

where the resulting value, 0 or 1, is stored in a pre-allocated array. A value of $I_{\mu_i} = 500$ was determined by comparing the average intensity of the full set of images for warm wake and cold wake patterns (summarized in Table 5.2). The values for warm wake and cold wake trails were averaged, defining an upper and lower bound for the I_{μ_i} constant. A value within the range was determined, weighted closer to the cold wake average from the range intermediate value due to the confidence based on the grouping of the cold wake intensity values.

In order to increase the robustness of the pre-processing step to varying sea conditions, the appearance of a ship body, or other unexpected targets, a voting procedure is implemented over a set of non-consecutive frames, where the result of Equation 5.2 must be equal for all frames, $p1_A = p1_{A+1} = p1_{A+2}$, for the detection algorithm mode to change. If any value is not equal to the other values, the detection mode remains at the previous detection mode. This pre-processing repeats every t_{p1} seconds.

For the FLIR A65 infrared imager, a window size of 100 x 100 pixels is used for each window to reduce the number of pixels to less than 10% of the full image

pixels. The pre-processing is completed for frames 1, 11, and 21 for every 900 frames (equivalent to $t_{p1} = 30$ seconds).

5.4.2 Background Estimation

The next step of the pre-processing phase of the thermal wake detection algorithm is generating a background model for subtraction from each frame, to correct for gradients in the infrared image due to heating on the lens or sensor of the imaging device (see Figure 5.3). Moreover, the generated background model must also take care to not include the target, which would subsequently be subtracted from the current frame. It is also notable that infrared imaging devices do generally correct for gradients across the sensor by performing a non-uniformity correction (NUC) which was found to work well for the FLIR A65 imager. However, for the FLIR Photon640 LWIR device, the gradients towards the corners of the sensor caused numerous false detections, and required correction.

To generate a background image, a set of frames are used, where each frame is spaced by the number of frames in time $t_{bg-elapse}$, or $p2_j = t_{bg-elapse} \cdot fps$. This process is represented schematically in Figure 5.3, block $p2$. Typically a value of $t_{bg-elapse} = 1$ seconds has been found to yield a good background estimate. A consequence to this method, however, is that the intensity of the background image may differ from the frame that it is subtracted from due to the movement of the aircraft, changes in the reflected sunlight, or other environmental conditions. This change in intensity causes additional errors and false detections. To solve this problem, the background estimate is continually updated at a rate of $t_{bg-update}$. To create the background estimate, the temporal mean of the frames is calculated after application of a median filter with a small square structuring element to remove noise. Moreover, to ensure the estimated background image does not remove the target, a minimum of 3

frames is used with $t_{bg-update}$ >10 seconds.

5.4.3 Transform Preparation

The formerly described pre-processing steps are used to setup the frames for the majority of the processing, thermal wake detection. Global thresholding is applied to the input frame, with the background removal applied, to remove the remaining image background and isolate regions of interest (ROI). The global thresholding selects pixels in the image if the intensity is above a threshold computed as

$$T_i \; = \; \mu + k\sigma \tag{5.3}$$

where μ is the mean of the pixel intensities, σ is the standard deviation of the pixel intensities, and k is a heuristic constant. The global thresholding step is used to create a binary image. The final step in the transform preparation stage of the algorithm, shown in Figure 5.3, block $m1$, is a set of morphological operations to remove any additional noise, smooth the final contours, and close any open spaces in the ROI. The initial morphological processing steps leverage the length of the wake pattern in the frame, applying a linear structuring element seventy percent of the vertical pixel dimension, merging any break and eliminating small holes. However, the length of this morphological close may fuse additional, shorter lines due to additional noise causing false detections. Therefore, the angles at which the morphological close are registered, and used to define a range for a morphological opening with a linear structuring element with a length of twenty-five percent of the vertical pixel dimension of the frame. This handling of additional noise also allows the heuristic constant, k, of the global thresholding to be smaller, allowing the algorithm the ability to detect wake patterns of lower contrast to the surrounding water. Next, a smaller

two-dimensional morphological opening is applied to smooth contours, and break or eliminate thin connections, followed by a morphological close to fill any holes and gaps in any contours. At this point in the algorithm, a frame containing a thermal wake pattern contains a channel of white pixels, surrounded by all black. Now that the pre-processing and frame preparation are complete, the Hough transform is applied to find the longest straight line segment, corresponding to the thermal wake pattern of a vessel.

5.5   Results and Discussion

In development of the thermal wake algorithm, the requirement of real-time operation in a small unmanned aircraft, with restricted power and space, bounded an upper limit to the processing time for each frame. As discussed in the previous section, detection on frames during the pre-processing steps is sacrificed. This time-sequential processing ensures that the most available processing is available for each pre-processing step. The algorithm was developed for a mini PC containing 4 GB of RAM, and an Intel i3 processor, using infrared images for the FLIR A65 camera with a resolution of 640 x 512, as reported in Table 5.1. The maximum processing time was determined as $t_{max} = 1/fps$, where $fps = 30$ Hz for the FLIR A65, and therefore $t_{max} = 0.033 \ s$.

5.5.1   Windowed Triple-Vote

The pre-processing step to determine the detection mode used 3 individual sectors of the image to improve the robustness of the algorithm by using a windowed triple-vote process, where two votes are conducted, the first within the image and the second for multiple images spaced in time. Using 3 sectors within the image ensures that the presence of a thermal wake pattern, or other thermal discontinuities, such as land

masses that do not span the entire image do not change the detection mode of the image. Overall, calculating the mean pixel value in three 100 x 100 pixel sectors in an image takes a longer time than processing the entire image, 0.01329 seconds and 0.015756 seconds respectively, but still falls below t_{max}. Moreover, comparing 3 image votes continuously ensures that the detection mode is correct. Figure 5.5a represents a LWIR image containing additional noise caused by temperature discontinuities, found in a set of 32 consecutive frames in the same data set containing a cold wake pattern. Applying the windowed vote process, the average intensity for the three windows is 64, 75, and 101, where the third value corresponds to the window region containing the majority of the higher pixel values. Using the multi-frame windowed vote process, the discontinuity in temperature did not affect the mode of operation. As a second example, Figure 5.5b presents a frame where an image of a ship is captured. The average intensity values for the three windows here are calculated to be 38, 40, and 40, comparable to the values in the previous frames where no ship was present.

5.5.2   Background Estimation

The resulting image generated from a set of 5 frames from the background estimate block of the real-time processing algorithm is presented in Figure 5.6, comparing the background image created where a median filter with a 3 x 3 structuring element is applied to each image before the temporal mean (Figure 5.6a) to the background estimate created by applying the median filter to the the temporal mean image (Figure 5.6b). To compare the resulting background estimates Figure 5.6b is subtracted from Figure 5.6a, shown in Figure 5.6c, showing the resulting noise remaining in the image. It is notable that all images required a histogram equalization to redistribute the intensity values in the image for better viewing. Block $p2$ take 0.020308 seconds to complete each run, having the frames saved to the memory so they do not have to be
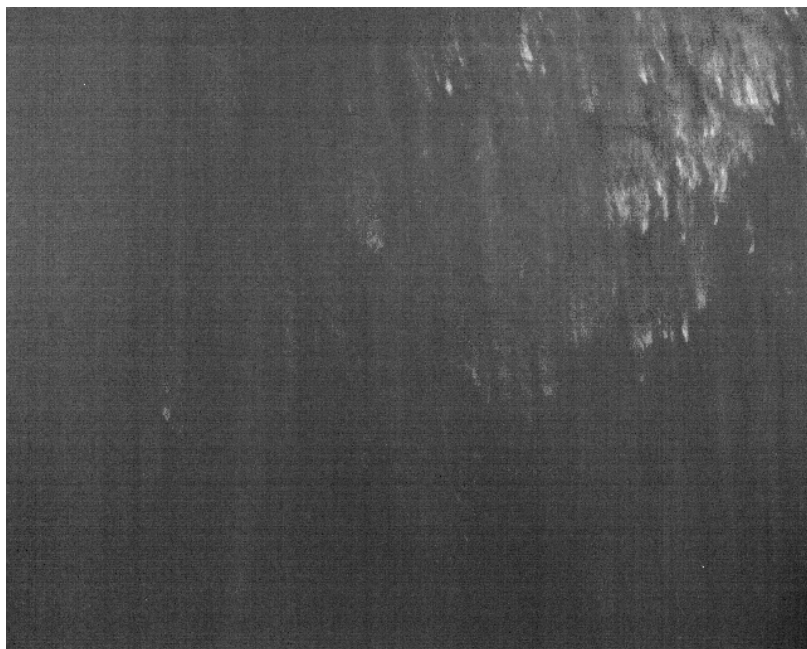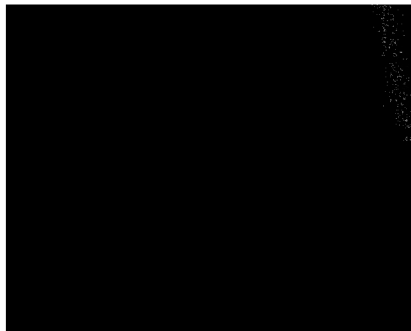
(a)

(b)

Figure 5.5: Examples of noise captured in the LWIR data requiring a method such as the multi-frame windowed vote process to ensure that the detection mode of the algorithm is correct. a) Scattered thermal discontinuity of an unknown source, and b) the hull of a ship.

(a)

(b)

(c)

Figure 5.6: Comparison of background estimation model results. a) Resulting background estimate when a median filter with a 3x3 structuring element is applied to each image, b) resulting background estimate when a median filter is applied after the temporal mean image is created. c) Subtraction of the image in b) from the image in a). A histogram equalization is performed on all images to visually show the background estimates.

written each time.

A background estimation technique for thermal images was reported in Reference [88], applying a median filter to 3 x 3 pixels before determining the temporal average. Jeon *et al.* report false background estimations when human targets are present in the image sequence, but otherwise robust background estimation to changes through multiple environmental conditions. In this method, however, the camera is stationary, such that the temporal average is of the same location for each pixel, as opposed to the moving platform of the UA that the thermal imager is mounted on for the reported thermal wake detection algorithm. However, assuming the surface temperature of the ocean is approximately constant within a region, and the imager noise is at the same location for each pixel, the methods become analogous if the number of frames used for the background estimation have a decreased amount of elapsed time between them to account for more abrupt changes in the background temperatures. Wang *et al.* reported a background estimation method for dim and small targets in infrared images for diverse and unique background scenes based on a total variation regularization and principal component pursuit method, reporting superior detection under various background conditions, including detection of a small ship in the sea [89]. For detection of ship bodies which exist in a small number of the thermal imager pixels, a method like the formerly mentioned could be beneficial. However, for the long thermal wake patterns observed here, a memory intensive process does not benefit the detection of the thermal wake patterns.

5.5.3   Transform Preparation

The final preparation stage before applying the Hough transform requires generating a binary image and removing any additional noise. A global threshold is applied to the frame once the background is removed as described in Equation 5.2, followed by

morphological processing to create a binary image with only large connected regions. Figure 5.7 shows a series of frames from different data sets of successful detections of cold and warm thermal wake patterns. Similarly, Figure 5.8 shows a set of images of missed or false detections. Figure 5.8a shows an example of a LWIR image in which the metallic body of the ship enters the frame, and the temperature range in the scene changes from a few degrees, to approximately 15°C, resulting in less contrast between the thermal wake pattern and the surrounding water. Noting that the sensor is capable of recording 8-bit data, each gray level would be roughly equivalent to the NETD of the sensor, 50 mK (see Table 5.1). Moreover, for SPSS detection, the body of the vessel is expected to be below the surface. Figure 5.8b demonstrates the second type of missed detection, due to a wake that is near the end of its persistence time, and barely detectable above the surrounding noise.

5.5.4   Hough Transform

The presence of false detections in the real-time thermal wake detection algorithm decreased when changing from the older FLIR Photon640 imager, to the FLIR A65 LWIR imaging device. In general, the algorithm is well tuned to discern low contrast wake patterns from the surrounding ocean water from the global thresholding and morphological processing steps in the algorithm. However, quick changes in background noise, notably due to heating of the imager lens or sensor were a notable source of false detections. An example of this error is shown in Figure 5.8c, where the quickly changing edge thermal discontinuity caused a series of false detection ahead of the background estimate updating. However, changing sensors to a newer model with updated uniformity correction algorithms significantly decreased these false detections. Table 5.3 presents an overview of the number of frames that thermal wakes were detected, the number of false detections among those detections, and the number
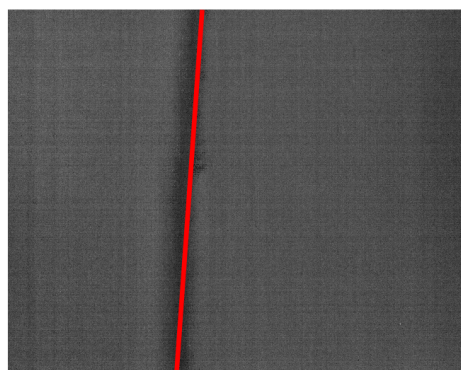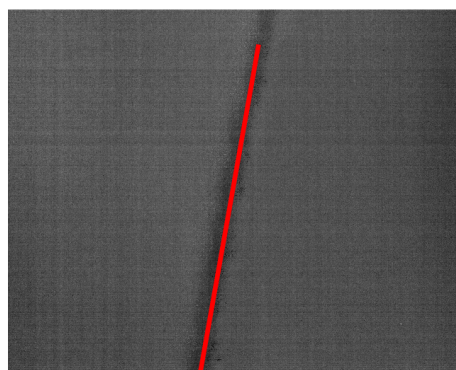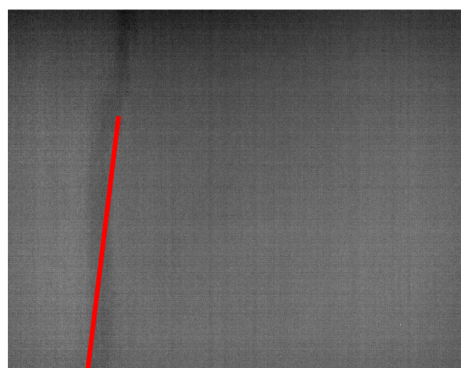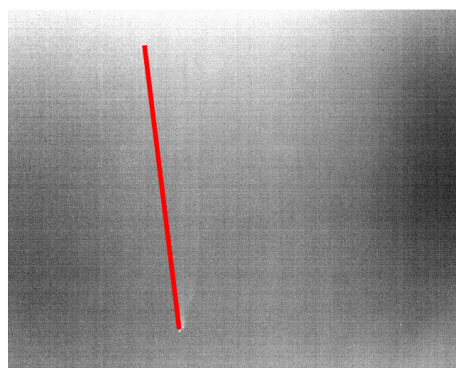
Figure 5.7: Examples of successful detections of a) cold wake pattern using FLIR Photon640, b) cold wake pattern using FLIR Photon640, c) cold wake pattern using FLIR A65, and d) warm wake pattern using FLIR Photon640.
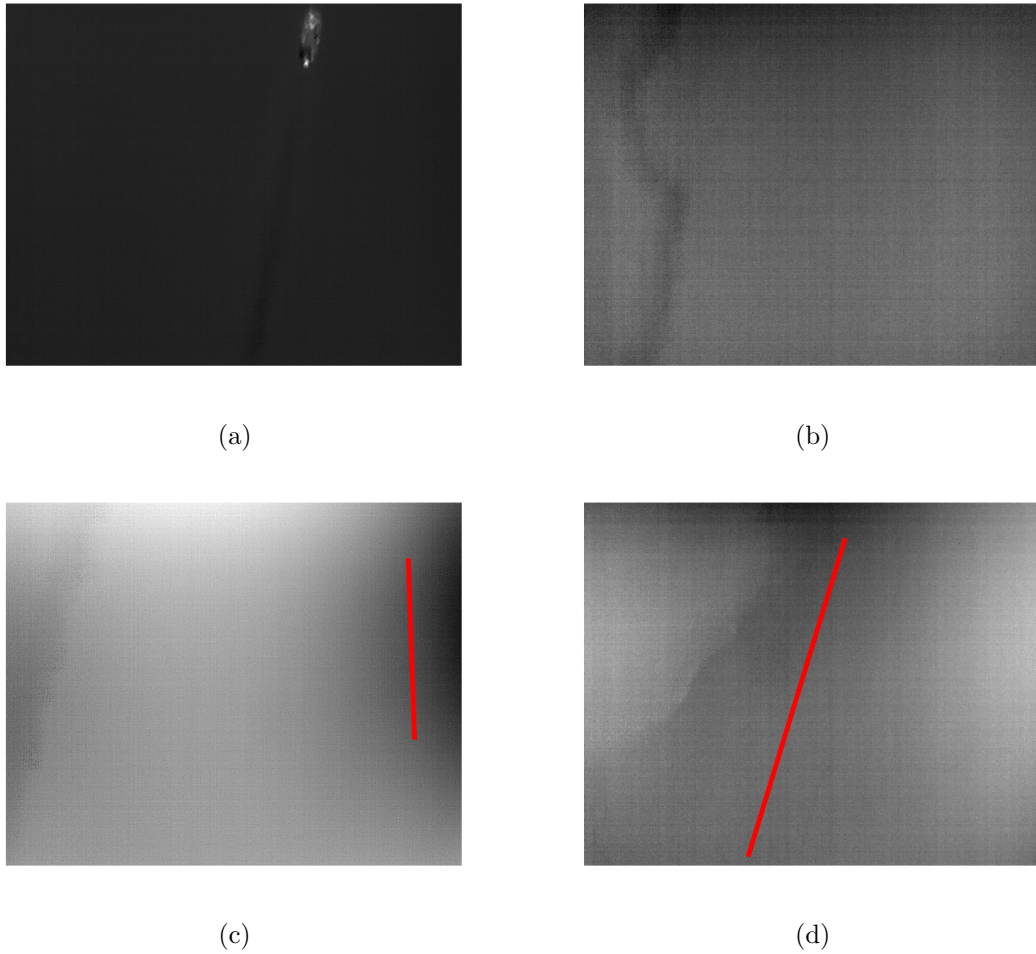
(a)

(b)

(c)

(d)

Figure 5.8: Missed detections when a) the surface bound vessel enters the frame, changing the contrast of the scene due to the increase in temperature range, and b) near the end of the wake persistence as the wake begins the normalize to the surrounding water temperature. False detections due to c) improper background estimate based on thermal heating of the imaging device, and d) wake like patterns in the ocean surface.

Table 5.3: Comparison of the number of frames where thermal wakes were detected, as well as missed and false detections for the real-time processing algorithm.

Number of frames	Wake Type	LWIR Imager	Frame with Detections	False Detections	Missed Detections	% Error
243	Cold	Photon640	38	6	7	5.3%
602	Cold	Photon640	43	3	8	1.8%
186	Warm	Photon640	14	4	7	5.9%
417	Cold	Photon640	22	3	11	3.4%
823	Cold	Photon640	28	3	12	1.8%
1436	Cold	A65	88	6	18	1.7%
1224	Warm	A65	96	9	21	2.5%

of missed detections in that data. For the FLIR Photon640 LWIR imager, the average rate of false detections was 15.1%, compared to 8.1% for the FLIR A65. However, it should be noted that the data collected with the FLIR Photon640 was from a moving air-based platform, whereas the data collected with the FLIR A65 was on a stationary gimbal platform. Similarly, the rate of missed detections is lower for the FLIR A65 compared to the FLIR Photon640. A continuous set of LWIR frames are shown in Appendix C.1 around the cold wake pattern.

Over 97% of the frames in the data presented here were processed correctly, noting less than 3% contained missed or falsely detected frames. As a final step to improve the system precision, a condition was created to require sequential detections in order to trigger a detection, since the thermal wake patterns were noted to occupy multiple consecutive frames. There was only a single case where a false detection occurred in 3 consecutive frames. Moreover, there was no case where no thermal wake was detected in conjunction with missed detection frames, concluding that there would be no missed detections.

No direct comparison to a LWIR algorithm for thermal wake detection of submerged vessels can be made based on current literature. Jiaqiu *et al.* reported an algorithm for wake detection using the Hough transform in grayscale SAR images [51].

The algorithm adds a signal-to-clutter ratio enhancement based on image subdivision, shown to improve the contrast of the wake to the clutter. However, the smaller the contrast is between the wake pattern and the surrounding pixels, the higher the probability is of false alarms, placing a limit on the detection of the wake pattern [51].

5.6   Conclusions

A real-time algorithm for the detection of thermal wake patterns of SPSS was described. A time sequential processing method was implemented to ensure real-time performance, while allowing maximum time for each pre-processing and detection preparation procedure. The robustness of the real-time detection algorithm of thermal wakes was increased by implementation of a windowed triple-vote system continuously using multiple frames. A transform preparation procedure is detailed, leveraging the assumption that the wake pattern will extend across a significant portion of the frame. This allows the algorithm to operate in a noisier environment, with a higher sensitivity, reducing the number of missed detections and low-contrast wake patterns. The real-time detection algorithm was developed using significantly varied data sets, including LWIR images collected from two different LWIR imaging devices, in the Atlantic and Pacific Ocean, from Canada and the United States, from air-based and land-based platforms. The real-time detection algorithm was demonstrated to yield an accuracy rate over 97%, higher than any algorithm reported for small UAS. A complete, mission-ready system is achieved, including both hardware and software packages.

Chapter 6

Conclusions

This work, and the related publications, are the initial reports of thermal wake-based detection of self-propelled semi-submersibles (SPSS), including for small UA platforms. Self-propelled semi-submersible vessels are designed to elude visual and radar detection, to transport illegal or dangerous cargo in an expendable, cost-effective method. This design consequently reduces the cargo capacity, deriving a requirement for more SPSS vessels to transport the equivalent quantity of cargo. Currently reported detection of these targets requires air and ground based assets and support, a relentlessly expensive and time-consuming endeavour. Using small UA platforms, the real-time detection algorithm presented could be incorporated in a autonomous or operator-limited procedure to monitor larger areas of the North American coastline. Moreover, this procedure would significantly decrease the required assets, both human and machine, required, while increasing the detection and interception rate of the SPSS.

The selection of a long wave infrared (LWIR) sensor for the application of thermal wake detection was summarized in Chapter 3, comparing data collected for medium-wave and long-wave infrared imaging devices from a low altitude aircraft platform.

The thermodynamics of infrared thermal imaging was presented, including the relationship between blackbodies and real surfaces. A radiometric chain technique was presented, resulting in a derivation of the infrared radiation of a real scene. Section 3.4.2 provides specific comparisons, and demonstrates the capabilities for thermal wake detection, demonstrating the factors which affect the resulting image quality, relating the physics of the detectors, platforms, and scenes.

Chapter 4 provided images of persistent thermal wake patterns, including cold (Section 4.3.1) and warm (Section 4.3.2) wake patterns, correlated to the recorded environmental conditions for SPSS. The wakes are supported with temperature measurements in the upper stratified layers of the ocean waters. It was demonstrated that temperature measurements in the top 4 m of the ocean water under normal solar heating gave a stratification with a differential of approximately 1^oC. Without the availability of solar heating due to ambient conditions, a warm wake pattern was noted, consistent with previously reported predictions from numerical models [23]. An initial image processing algorithm using a Hough transform to highlight the longest line segments in the images was investigated and presented to determine the validity of real-time detection of the thermal wake patterns. It was shown that this algorithm can distinguish the wake patterns from the surrounding water in the long wave infrared images.

An algorithm for the detection of submerged vessel wake patterns using a LWIR camera was presented in Chapter 5, specifically for a small unmanned aircraft, with limited power, space, and computing power. A time-sequential processing method was presented to reduce the required computing, while allowing a high frame rate, and a robust system to noise and other environmental factors. Moreover, a windowed triple-vote system was developed, which is continually applied to ensure that the detection mode is correctly set by the algorithm, while ignoring unexpected targets in the image.

A simple background estimation method is presented to remove any non-uniformity in the captured images. A transform preparation procedure is detailed, specifically for thermal wake detection, allowing the algorithm to operate in a noisier environment, with a higher sensitivity, reducing the number of missed detections and low-contrast wake patterns. A payload system was prepared for a small UA platform, allowing real-time processing and monitoring. Using data sets for three different platforms, captured with two different LWIR imagers, in two oceans, a real-time algorithm is developed with a greater than 97% reliability rate.

Considering the high detection rate in low contrast, noisy environments with slowly changing backgrounds, SAR imaging for ship wake tracking is an obvious extension. Section 2.2.6 summarizes the current work in the user assisted and automatic detection of ship wake detection in radar images, noting a current detection equivalent or higher to that recorded here. This application would require minimal modification based on the application.

The requirement for a real-time hazard identification system for water bomber aircraft, in particular for obstacle detection such as logs and power lines, is a notable potential adoption for this technology. It is expected that with alteration, the detection of multiple target types would be achieved, in particular if the time sequential processing steps were used to allocate the frames to multiple morphological processing sections depending on the intended target. The algorithm could be further improved by employing a imager with a 60-120 Hz frame rate, or increasing the available processing power.

The concepts presented in this thesis are also directly applicable to marine mammal tracking. Previous reports, as described in Section 2.2.3, determined that while thermal wake patterns were present, thermal imaging of the mammals body or blows were more useful for tracking. However, the real-time detection algorithm could be

adapted to work in the cold and warm wake detection method in parallel, to detect both thermal wake patterns, as well as mammal bodies and blows to increase the detection in a noisy ocean environment. Moreover, land-based tracking of large mammals is another conceivable application of this work. The main addition would be a more robust background estimation algorithm, a topic which has been extensively studied in EO and IR in literature. Moreover, similar alterations could be completed to the algorithms to finesse detection for environmental monitoring of oil slick, temperature measurements, and power line detection. A comparison of MWIR, LWIR, and EO images are shown in Figure 6.1, revealing an increase in contrast between the power lines and the background in the LWIR as compared to the MWIR and EO.

The real-time detection algorithm presented in this work was specifically developed for a small UAs platform, with restricted payload, power, and processing. Despite the demonstrated ability to surpass expectations based on previous literature results for noisy, low contrast environments, a pair of recommendations are provided, based on significance; utilize sensor cooling for the LWIR sensor, and increase the sensor resolution.

Cooling for LWIR sensors is generally not used. In fact, the lack of a cooling requirement is generally a significant benefit for LWIR sensors as compared to MWIR sensors that require cooling to reduce noise. It is important to note, however, that the suggested cooling for LWIR sensors is not equivalent to the refrigerant-type cooling of MWIR sensors, but instead temperature stability from non-uniform changes to reduce noise on the sensor and heating on the optics of the imaging device, which would in turn result in improved performance of the real-time algorithm. However, it should be noted that in this work the comparison of the FLIR Photon640 and FLIR A65 noted a reduction in sensor noise in the FLIR A65, the newer sensor. The trend in sensor technology may not require active cooling of the LWIR sensor with improved

(a)

(b)

(c)

Figure 6.1: A comparison of a) an optical image with b) a medium wave, and c) a long wave infrared image of a highway.

sensor uniformity corrections.

Long wave infrared sensors are currently available in higher resolutions than 640 x 512, but require increased processing to achieve real-time performance. However, at a set the swath of a single pixel is decreases with increasing sensor resolution, equivalent to a higher sampling of the scene which would result in an increased system performance. Moreover, if the field of view is increased proportional to the sensor resolution, then less area must be covered by a surveillance UA to cover the same acreage. This could also enable the ability to use a fixed, downward facing LWIR imaging device for SPSS detection.

In the future, this system could be directly deployed for detection of SPSS vessels encroaching on the North American coastline. Current development of auto pilot integration and communication for swarms of UAs could allow simultaneous monitoring of limitless coast line ranges. The algorithm could also be implemented with a LWIR platform typically used for remote sensing on a UA platform. Moreover, if the platform size is increased or more processing power is available, due to technology advances or payload space, then a more robust background model should be implemented that accounts for much faster changing, less constant background.

Bibliography

[1] S. D. Lord, "A new software tool for computing Earth's atmospheric transmission of near- and far-infrared radiation," NASA Technical Memorandum 103957, Tech. Rep., Dec. 1992.

[2] S. D. Lord, "NASA technical memorandum 103957," Gemini Observatory, Tech. Rep., 1997.

[3] G. M. Hale and M. R. Querry, "Optical constants of water in the 200-nm to 200-m wavelength region," *Appl. Opt.*, vol. 12, pp. 555–563, 1973.

[4] C. Woody, "The coast guard is detecting a new trend among high-seas narco smugglers," *Business Insider*, 2017.

[5] D. Kushner, "Drug-sub culture," *The New York Times*, April 26, 2009.

[6] L. C. J. Frederick, "Drug subs in the caribbean littorals," *U.S. Naval Institute*, 2012.

[7] W. D. Garrett and P. M. Smith, "Physical and chemical factors affecting the thermal infrared imagery of ship wakes," Naval Research Laboratory, Tech. Rep., 1984.

[8] J. Styron, "Infrared cameras improve in-line quality control," Machine Design.com, Tech. Rep., 2009.

[9] J. Svejkovsky and J. Muskat, "Real-time of oil slick thickness patterns with a portable multispectral sensor," US Department of the Interior Minerals Management Service, Tech. Rep., 2006.

[10] J. Strothman, "Automated infrared imaging technology gains inroads in niche temperature-sensitive segments," InTech, Tech. Rep., 2006.

[11] M. P. Kontitsis, N. C. Tsourveloudis, and K. P. Valavanis, "A UAV automated airborne surveillance system," *Conference on Control and Automation*, p. 1, 2003.

[12] M. P. Kontitsis, N. C. Tsourveloudis, and K. Valavanis, "A UAV vision system for airborne surveillance," *International Conference on Robotics and Automation*, p. 77, 2004.

[13] A. Sekman and F. Yao, "Multi-sensor vision data fusion for smart airborne surveillance," Airforce Research Laboratory, Tech. Rep., 2009.

[14] LZ, "Narco submarines, torpedoes, and semi submersibles," June 2010, http://covertshores.blogspot.ca/2010/06/narco-submarines-torpedoes-and-semi.html.

[15] K. S. Bryan, "Advantage narcotraffickers: mitigating the threat of the self-propelled semi submersible platform," Air War College Air University, Tech. Rep., 2009.

[16] M. Harwood, "New law and bilateral agreements help U.S. stop semi-submersible drug smuggling," *Security Management*, 2008.

[17] L. C. Braesch, "First caribbean drug sub bust," *Coast Guard Compass*, Aug. 9, 2011.

[18] L. S. Young, "Second caribbean drug sub bust," *Coast Guard Compass*, Oct. 4, 2011.

[19] L. Young, "Third time's a charm 7 tons of cocaine seized," *Coast Guard Compass*, Oct. 31, 2011.

[20] J. Douglas, "CBP air and marine spot submersible loaded with cocaine worth $1,000,000,000," *Aviation Online Magazine*, April 12, 2012.

[21] P. Wang, P. Wang, Z. Qu, Y. Gao, and Z. Shen, "A novel algorithm for visual and ir image registration based on hough transform," in *2011 International Workshop on Multi-Platform/Multi-Sensor Remote Sensing and Mapping*, Jan 2011, pp. 1–4.

[22] K. McIntosh, "Ship tracking using visible and thermal imagery from master," 2012, http://www.scribd.com/doc/61556611/Ship-Tracking-Using-Visible-and-Thermal-Imagery-from-MASTER.

[23] M. Stewart, "Numerical predictions of thermal ship wakes," Naval Research Laboratory, Tech. Rep., 1987.

[24] J. Zhang, X. Chen, L. Yang, J.-T. Yuan, and X.-H. Zhang, "Study of temperature characteristic of cooling water discharged by underwater vehicle," *Journal of Ship Mechanics*, vol. 13, no. 4, pp. 533 – 539, 2009.

[25] J. Zhang, L. Yang, J.-T. Yuan, X. Chen, H.-K. Liu, and X.-H. Zhang, "Experimental research of underwater vehicle thermal wakes," *Journal of Experiments in Fluid Mechanics*, vol. 22, no. 3, pp. 7 – 13, 2008.

[26] M. Wu, B. Chen, X. Zhang, L. Yang, and B. Yuan, "Experiment of surface thermal features of wake behind a going body underwater in a temperature stratification water tank," *Infrared and Laser Engineering*, vol. 40, no. 8, pp. 1425 – 1431, 2011.

[27] X.-F. Zhang, L. Yang, M.-M. Wu, and Y.-C. Du, "Experimental study of the thermal characteristic of submarine wake in the temperature stratified flow," *Journal of Experiments in Fluid Mechanics*, vol. 25, no. 2, pp. 45 – 48+53, 2011.

[28] A. Benilov, B. Bunin, G. Dardiere, A. Sutin, D. Zeng, and R. Martini, "On detecting surface and sub-surface bodies in the water by virtue of their surface and water column wakes," *Waterside Security Conference International*, pp. 1 – 8, 2010.

[29] S. I. Voropayev, C. Nath, and H. J. S. Fernando, "Thermal surface signature of ship propeller wakes in stratified waters," *Physics of Fluids*, vol. 24, p. 116603, 2012.

[30] L. C. Cuyler, R. Wiulsrod, and N. A. Oritsland, "Thermal infrared radiation from free living whales," *Marine Mammal Science*, vol. 8, p. 120, 1992.

[31] J. Graber, "Land-based infrared imagery for marine mammal detection," Master's thesis, University of Washington, 2011.

[32] W. L. Perryman, M. A. Donahue, J. L. Laake, and T. E. Martin, "Diel variation in migration rates of eastern pacific gray whales measured with thermal imaging sensors," *Marine Mammal Science*, vol. 15, p. 426, 1999.

[33] A. Baldacci, M. Carron, and N. Portunato, "Infrared detection of marine mammals," NATO Undersea Research Center, Tech. Rep., 2005.

[34] J. Churnside, L. Osrovsky, and T. Veenstra, "Thermal footprint of whales," *Oceanography*, vol. 22, pp. 206 – 209, 2009.

[35] C. E. Torgersen, R. N. Faux, B. A. McIntosh, N. J. Poage, and D. J. Norton, "Airborne thermal remote sensing for water temperature assessment in rivers and streams," *Remote Sensing of Environment*, vol. 76, p. 386, 2001.

[36] A. Jensen, B. Neilson, M. McKee, and Y. Chen, "Thermal remote sensing with an autonomous unmanned aerial remote sensing platform for surface stream temperatures," in *2012 IEEE International Geoscience and Remote Sensing Symposium*, July 2012, pp. 5049–5052.

[37] M. Lu, G. Sheng, Y. Liu, X. Jiang, S. Nie, and G. Qu, "Research on auto-tracking algorithm for power line inspection based on unmanned aerial vehicle," in *2012 Asia-Pacific Power and Energy Engineering Conference*, March 2012, pp. 1–5.

[38] T. Suzuki, Y. Amano, J. Takiguchi, T. Hashizume, S. Suzuki, and A. Yamaba, "Development of low-cost and flexible vegetation monitoring system using small unmanned aerial vehicle," in *ICCAS-SICE, 2009*, Aug 2009, pp. 4808–4812.

[39] O. A. Yakimenko, I. I. Kaminer, W. J. Lentz, and P. A. Ghyzel, "Unmanned aircraft navigation for shipboard landing using infrared vision," *IEEE Transactions on Aerospace Electronic Systems*, vol. 38, pp. 1181–1200, Oct. 2002.

[40] A. Martins, A. Dias, J. Almeida, H. Ferreira, C. Almeida, G. Amaral, D. Machado, J. Sousa, P. Pereira, A. Matos, V. Lobo, and E. Silva, "Field experiments for marine casualty detection with autonomous surface vehicles," in *Oceans - San Diego, 2013*, Sept 2013, pp. 1–5.

[41] M. Diani, A. Baldacci, and G. Corsini, "Joint striping noise removal and background clutter cancellation in IR naval surveillance systems," *IEE Proceedings - Vision, Image and Signal Processing*, vol. 148, no. 6, 2001.

[42] S. Kim, Y. Yang, and J. Lee, "Horizontal small target detection with cooperative background estimation and removal filters," in *2011 IEEE International Conference on Acoustics, Speech and Signal Processing*, 2011, pp. 1761–1764.

[43] A. Soloviev, M. Gilman, K. Young, S. Brusch, and S. Lehner, "Sonar measurements in ship wakes simultaneous with TerraSAR-X overpasses," *IEEE Transactions on Geoscience and Remote Sensing*, vol. 48, p. 841, 2010.

[44] M. Torrence, "Seasat," *International Laser Ranging Service*, 2011.

[45] W. H. Munk, F. M. R. S, P. Scully-Power, and F. Zachariasen, "Ships from space," *Proc. R. Soc. Lond. A*, vol. 412, p. 231, 1987.

[46] D. Crisp, *The state of the art in ship detection in synthetic aperture radar imagery*. Intelligence, Surveillance and Reconnaissance Division Information Sciences laboratory, 2004.

[47] A. Reed and J. Milgram, "Ship wakes and their radar images," *Annual Review of Fluid Dynamics*, pp. 469–502, 01 2002.

[48] J. Chen, B. Chen, and J. Yang, "The turbulent wake detection and beam estimation of a ship in SAR images," *International Workshop on Geoscience and Remote Sensing*, p. 230, 2008.

[49] N. R. Stapleton, "Ship wakes in radar imagery," *Int J Remote Sensing*, vol. 18, p. 1381, 1997.

[50] I. Hennings, R. Romeiser, W. Alpers, and A. Viola, "Radar imaging of kelvin arms of ship wakes," *Int J Remote Sensing*, vol. 20, p. 2519, 1999.

[51] A. Jiaqiu, Q. Weidong, D. Yunkai, L. Fan, S. Li, and K. Yafei, "A novel ship wake CFAR detection algorithm based on SCR enhancement and normalized hough transform," *IEEE Geoscience and Remote Sensing Letters*, vol. 8, p. 681, 2011.

[52] H. T. Wang, O. M. Griffin, and G. A. Meadows, "Hull characteristics from SAR images of ship wakes," *Geoscience and Remote Sensing Symposium*, vol. 3, p. 1278, 1994.

[53] Y. Wu and J. Wang, "Detection of ship wakes in SAR images based on radon transform," *Geoscience and Remote Sensing Symposium*, p. 969, 2008.

[54] K. Eldhust, "An automatic ship and ship wake detection system for spaceborne SAR images in coastal regions," *IEEE Transactions on Geoscience and Remote Sensing*, vol. 34, p. 1010, 1996.

[55] G. Du and T. Yeo, "A novel Radon transform-based method for ship wake detection," *Geoscience and Remote Sensing Symposium*, p. 3069, 2004.

[56] J. Yaqui and W. Shiqing, "An algorithm for ship wake detection from SAR images using the radon transform and morphological image processing," *Journal of Systems Engineering and Electronics*, vol. 12, pp. 7–12, 2001.

[57] P. Courmontagne, "An improvement of ship wake detection based on the radon transform," *Signal Processing*, vol. 85, no. 8, pp. 1634 – 1654, 2005.

[58] M. Barni, M. Betti, and A. Mecocci, "A fuzzy approach to oil spill detection an SAR images," in *1995 International Geoscience and Remote Sensing Symposium. Quantitative Remote Sensing for Science and Applications*, vol. 1, 1995, pp. 157–159 vol.1.

[59] P. Alli, P. Ramasubramanian, and V. Sureshkumar, "Oil spills detection in SAR images using nonlinear fuzzy filter," *International Journal of Advanced Science and Technology*, vol. 25, pp. 7–16, 2010.

[60] Y. Suo and H. Guo, "De-noising and enhancement for SAR oil slick based on srad," in *2011 International Conference on Computer Science and Network Technology*, vol. 2, 2011, pp. 1136–1139.

[61] R. Fjortoft, P. Marthon, A. Lopes, F. Sery, D. Ducrot-Gambart, and E. Cuberocastan, "Region-based enhancement and analysis of SAR images," in *Proceedings of 3rd IEEE International Conference on Image Processing*, vol. 3, 1996, pp. 879–882 vol.3.

[62] D. Chaudhuri, A. Samal, A. Agrawal, Sanjay, A. Mishra, V. Gohri, and R. C. Agarwal, "A statistical approach for automatic detection of ocean disturbance

features from SAR images," *IEEE Journal of Selected Topics in Applied Earth Observations and Remote Sensing*, vol. 5, no. 4, pp. 1231–1242, 2012.

[63] F. Pedrotti, L. Pedrotti, and L. Pedrotti, *Introduction to Optics*. Pearson Prentice Hall, 2007.

[64] A. Rogalski, "Infrared detectors an overview," *Infrared Physics and Technology*, vol. 43, p. 187, 2002.

[65] FLIR, "Oil spill detection with infrared imaging," FLIR, Tech. Rep., 2012.

[66] P. Withagen, K. Schutte, A. Vossepoel, and M. Breuers, "Automatic classification of ships from infrared (FLIR) images," in *Signal Processing, Sensor Fusion, and Target Recognition VIII*, ser. SPIE, Kadar, I, Ed., vol. 3720, 1999, pp. 180–187.

[67] J. Wu, S. Mao, X. Wang, and T. Zhang, "Ship target detection and tracking in cluttered infrared imagery," *Optical Engineering*, vol. 50, no. 5, 2011.

[68] J. Peckham, M. Shehata, S. O'Young, and J. Jacobs, "Development of an algorithm to detect sub-surface vessels using infrared imagery," in *IEEE NECEC*, 2013.

[69] M. Planck, "On the law of distribution of energy in the normal spectrum," *Annalen der Physik*, vol. 4, p. 553, 1901.

[70] W. Wien, "Concerning the energy distribution in the emission spectrum of a blackbody," *Annalen der Physik*, vol. 294, no. 8, 1896.

[71] J. Stefan, "About the relationship of heat radiation and temperature," *Sitzungsberichte der Kaiserlichen Akademie der Wissenschaften*, vol. 79, pp. 391–428, 1879.

[72] L. Boltzmann, "Derivation of stefan's law concerning the dependence of the thermal radiation on the temperature of the electro-magnetic theory of light," *Annalen der Physik und Chemie*, vol. 22, pp. 291–294, 1884.

[73] R. Gade and T. B. Moeslund, "Thermal cameras and applications: a survey," *Machine Vision and Applications*, vol. 25, pp. 245 – 262, 2014.

[74] M. Vollmer and K. Möllmann, *Infrared Thermal Imaging: Fundamentals, Research and Applications*. Wiley, 2010.

[75] E. Hecht, *Optics*, 4th ed. Addison Wesley, 2001.

[76] J. Dakin and R. Brown, *Handbook of Optoelectronics (Two-Volume Set)*. Taylor & Francis, 2010.

[77] FLIR, "Seeing through for and rain with a thermal imaging camera," FLIR, Tech. Rep., 2013.

[78] ——, "The ultimate infrared handbook for research and development professionals," FLIR, Tech. Rep., 2014.

[79] MATLAB, *version 7.14.0739 (R2012a)*. Natick, Massachusetts: The MathWorks Inc., 2012.

[80] G. Gubareff, J. Janssen, and R. Torborg, *Thermal Radiation Properties Survey: A Review of the Literature*. Honeywell Research Center, 1960.

[81] S. Burnay, T. Williams, and C. Jones, *Applications of Thermal Imaging*. Taylor & Francis, 1988.

[82] M. A. Suckow, S. H. Weisbroth, and C. L. Franklin, "Chapter 2 - temperature in the oceans," in *Seawater*, 2nd ed. Oxford: Butterworth-Heinemann, 1995, pp. 14 – 28.

[83] J.-A. Wang, Y. Guo, and J.-N. Gu, "Theoretical and trial study of thermal wake in the infrared detection of submarines," *Laser and Infrared*, vol. 32, no. 3, pp. 159 – 159, 2002.

[84] J. Peckham, S. O'Young, and J. Jacobs, "Comparison of medium and long wave infrared imaging for ocean based sensing," *Journal of Ocean Technology*, vol. 10, p. 112, 2015.

[85] P. Hough, "Method and means for recognizing complex patterns," Patent US 1 771 560A, 1962.

[86] J. Radon, "Über die Bestimmung von Funktionen durch ihre Integralwerte längs gewisser Mannigfaltigkeiten," *Akad. Wiss.*, vol. 69, pp. 262–277, 1917.

[87] MATLAB, *version 9.3.0.713579 (R2017b)*. Natick, Massachusetts: The MathWorks Inc., 2017.

[88] E. S. Jeon, J.-S. Choi, J. H. Lee, K. Y. Shin, Y. G. Kim, T. T. Le, and K. R. Park, "Human detection based on the generation of a background image by using a far-infrared light camera," *Sensors*, vol. 15, no. 3, pp. 6763–6788, 2015.

[89] X. Wang, Z. Peng, D. Kong, P. Zhang, and Y. He, "Infrared dim target detection based on total variation regularization and principal component pursuit," *Image and Vision Computing*, vol. 63, pp. 1 – 9, 2017.

[90] R. Gonzalez and R. Woods, *Digital Image Processing*. Pearson/Prentice Hall, 2008.

[91] M. van Ginkel, C. L. Hendriks, and L. van Vliet, "A short introduction to the radon and hough transforms and how they relate to each other," Quantitative Imaging Group, Delft University of Technology, Tech. Rep., 2004.

Appendix A

UAS Payload Images

A.1   UAS Payload

A payload system to mount a FLIR A65 long wave infrared camera and GoPro Hero2 optical camera for autonomous data collection was developed. The camera is mounted on an Arris Zhaoyun 3-Axis Brushless Gimbal, presented in Figure A.1a, with a custom carbon fiber mount for both imagers. Figure A.1b shows the customized gimbal, with the FLIR A65 and GoPro Hero2. An overview of the operating specifications for the FLIR A65 are given in Table 5.1. This customized gimbal was designed to mount to the base of a Mugins 3M H-Tail TBM unmanned aircraft platform in the payload bay using a custom mounting system containing 16 vibration damping balls to reduce the vibration of the gimbal. The gimbal contains a Basecam SimpleBGC controller with an on board inertial measurement unit (IMU), and allows full control over the tuning and program of the gimbal, as well as stabilization. It is noted that a 113 gram counter-weight was added to the outside edge of the gimbal frame (near the GoPro) to balance the gimbal. Figure A.4 shows an image of the gimbal mounted below the TBM aircraft.
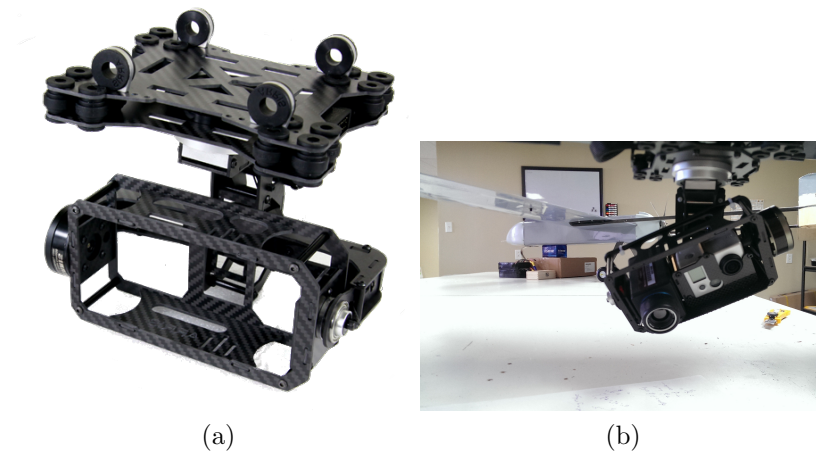
Figure A.1: a) Arris Zhaoyun 3-Axis brushless gimbal, b) Arris Zhaoyun 3-Axis brushless gimbal with custom carbon fiber mounting ring for installation of FLIR A65 and GoPro Hero 2.

Figure A.2: Image of the ground control station used to monitor, record, and control the gimbal.

Figure A.3: Tripod with gimbal mounted and data monitoring system for remote data collection.

Figure A.4: Image of the customized gimbal containing the FLIR A65 LWIR camera and GoPro Hero2 EO imager mounted on the Mugins 3M H-Tail TBM.

Appendix B

Comparison of Hough and Radon Transform

B.1   Transform Comparison

The extraction of image elements such as lines, edges, and curves is often a key step in image processing algorithms. Of particular interest for line detection is the Hough transform [85], previously reported for wake detection of SPSS in Ref [68]. In comparison, the majority of the reports of surface-based ship wake detection in SAR images leverages the Radon transform [86], reporting beneficial results [46]. In the following sections, a brief introduction to the Radon and Hough transform are given. A comparison of the detection of thermal wake patterns is then summarized.

B.1.1   Hough Transform

The Hough transform was originally used to detect straight lines in black and white images, but this feature extraction technique has been extended for arbitrary shapes. Considering a point $(x_i,\ y_i)$ which has an infinite number of lines passing through it,
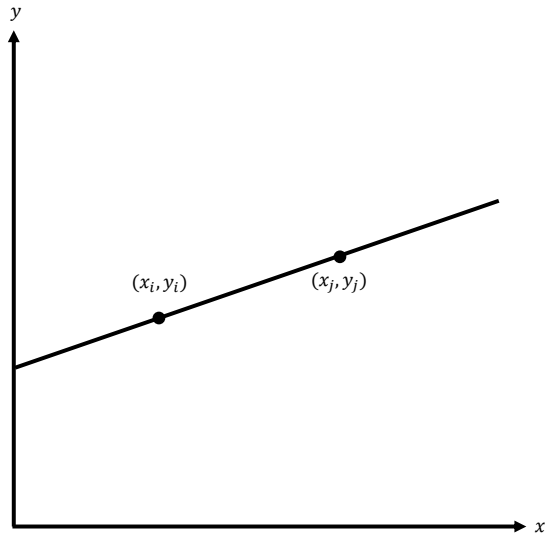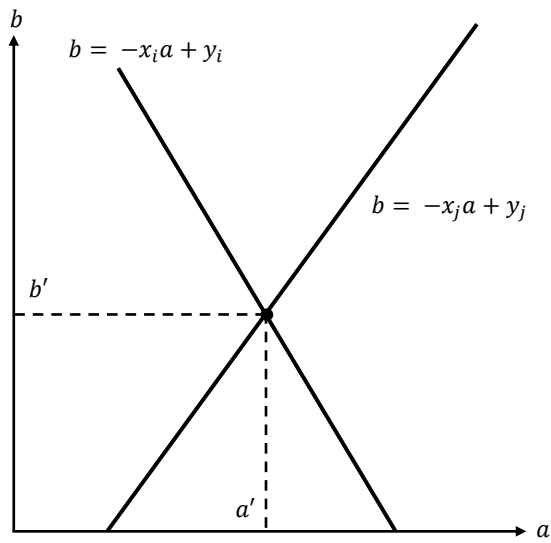
Figure B.1: a) Represents the points $(x_i, \ y_i)$ and $(x_j, \ y_j)$ on a line with equation $y_i \ = \ a'x_i \ + \ b'$ in the xy-plane. b) The parameter space representation of points $(x_i, \ y_i)$ and $(x_j, \ y_j)$, which intersect at point (a', b') .
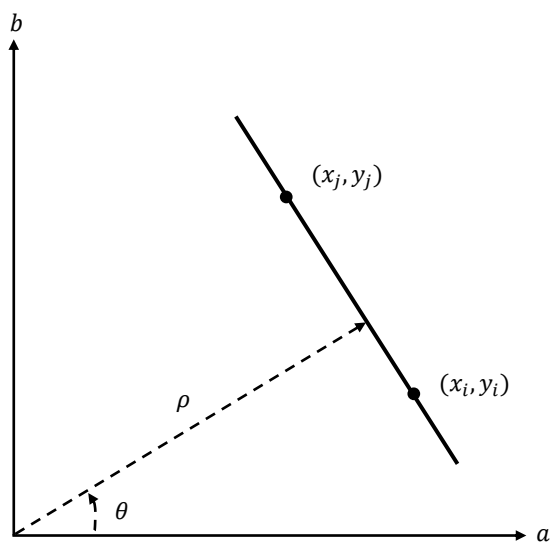
(a)
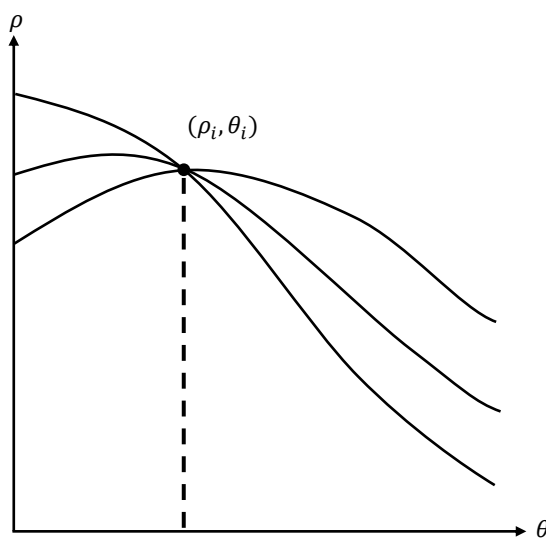
(b)

Figure B.2: a) A geometrical representation of the relationship to ρ and θ in the xy-plane, b) the intersection point (ρ_i, θ_i) in parameter space, corresponding to the line which passes through $(x_i,\ y_i)$ and $(x_j,\ y_j)$ in a.

described in slope-intercept as $y_i = ax_i + b$. Re-written as $b = -x_i\,a + y_i$, where the (a, b) plane, or parameter space, gives the equation for a specific line for a fixed pair of $(x_i,\ y_i)$. For a second point (x_j, y_j), the associated line in parameter space intersects the parameter space representation of $(x_i,\ y_i)$ at a point $(a',\ b')$, where in the xy-plane the equation $y_i = a'x_i + b'$ contains both points $(x_i,\ y_i)$ and $(x_j,\ y_j)$, as well as any other points of which the parameter space representation intersects point $(a',\ b')$ [90]. The relationship is illustrated in Figure B.1. However, the previous description fails as the line becomes vertical or $a \to \infty$. Therefore, similar to what is described in Section B.1.2 the normal representation is used for a line,

$$x\cos\theta + y\sin\theta = \rho \tag{B.1}$$

where ρ is the distance from the origin to the line at an angle θ from the x-axis. A geometrical representation of the relationship to ρ and θ in the xy-plane is shown in Figure B.2a. Figure B.2b shows the intersection point $(\rho',\ \theta')$ in parameter space, corresponding to the line which passes through $(x_i,\ y_i)$ and $(x_j,\ y_j)$ (shown in Figure B.2a). In a computational sense, the parameter space is divided into accumulator cells, where an accumulator square, $A(i, j)$, corresponds to a parameter space coordinate, (ρ_i, θ_j) [90].

B.1.2 Radon Transform

The Radon transform is useful in pattern recognition since the projection of a pattern is done without loss of information. Only non-zero pixels are projected in the Radon matrix, retaining only necessary information. In Cartesian coordinates, a straight line can be described as
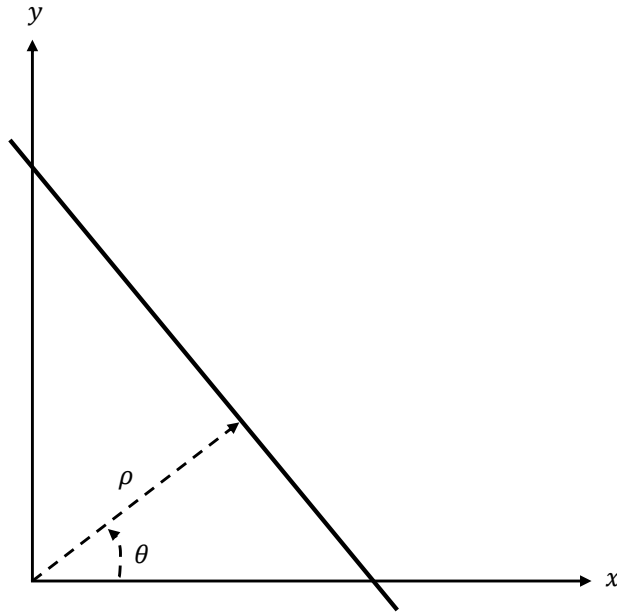
Figure B.3: Normal representation of a straight line in the Radon transform.

$$x \cos \theta + y \sin \theta = \rho \qquad \text{(B.2)}$$

where ρ is the distance from the origin to the line at an angle θ from the x-axis. The Radon transform has the form

$$\Re\{f(x,y)\} = \int_{-\infty}^{\infty} \int_{-\infty}^{\infty} f(x,y)\ \delta(x \cos \theta + y \sin \theta - \rho)dx\ dy \qquad \text{(B.3)}$$

which gives the projection of a function $f(x,y)$ in Euclidean space along an arbitrary line in the xy-plane [90]. The Kronecker delta function, δ, in Equation B.3 converts the two-dimensional integral into a line integral along the axis $x \cos \theta + y \sin \theta = \rho$. For a shape in an image with parameter set a, for each vector in parameter space which does not contain parameters of the curve, $\mathbf{p} \neq a$, the Radon transform evaluates to an infinite number, proportional to the number of intersections between the shapes

$c(a)$ and $c(\mathbf{p})$. When $\mathbf{p} = a$ however, the Radon transform yields a large response, corresponding to a peak in the parameter space.

The Radon transform and Hough transform are equivalent, essentially being a form of template matching. However, the Radon transform is a mapping, where a data point in the destination space is obtained from the data in source space. In contrast, the Hough transform considers how a data point in the source space maps onto the data points in the destination space [91]. Figure B.4 demonstrates this comparison. For the Hough transform, consider the entire function is initialized to zero, such that for each point x in the input image determines its contributions, weighted to each of the points P, represented in Figure B.4a. Figure B.4b demonstrates for each collected point p, the values of $I(x)$ are collected, to which the templates are applied and summed.
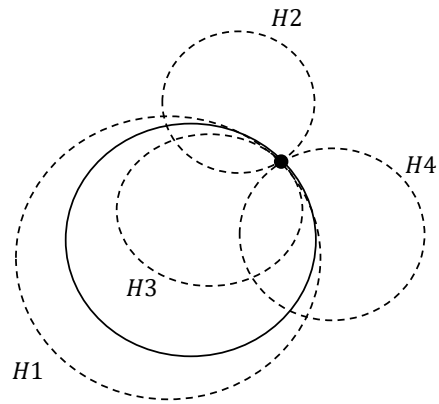
(a)
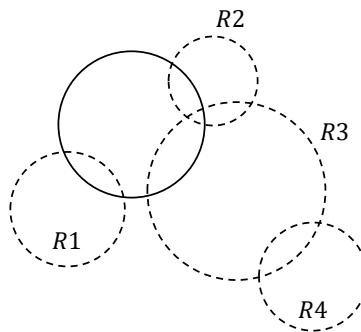
(b)

Figure B.4: a) Explanation of the Hough transform. The point where the four dashed curves intersect. b) An explanation of the Radon transform. Integrating the intensity values along each dashed curve results in small values, unless the curve coincides with a curve in the image whereby the integral results in a large value.

Appendix C

Sequential Frame Detection

C.1   Sequential Processed Frames
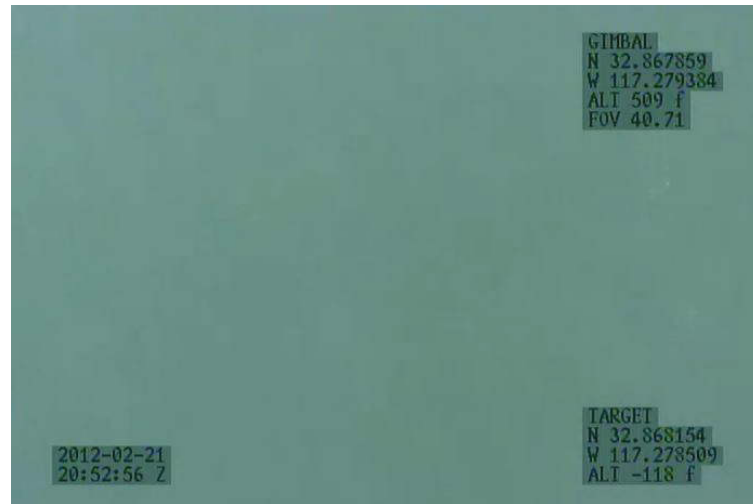
(a)
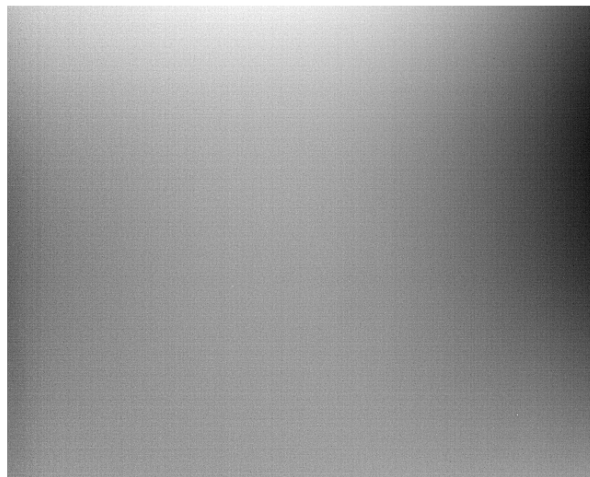
(b)

Figure C.1: Frame 248 a) optical and b) long wave infrared image.
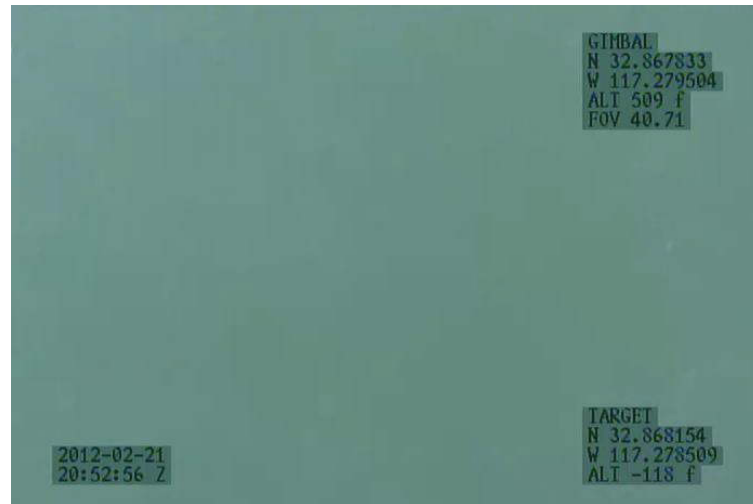
(a)
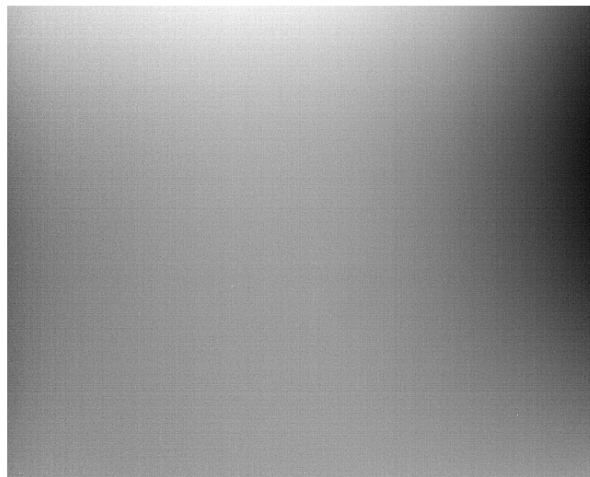
(b)

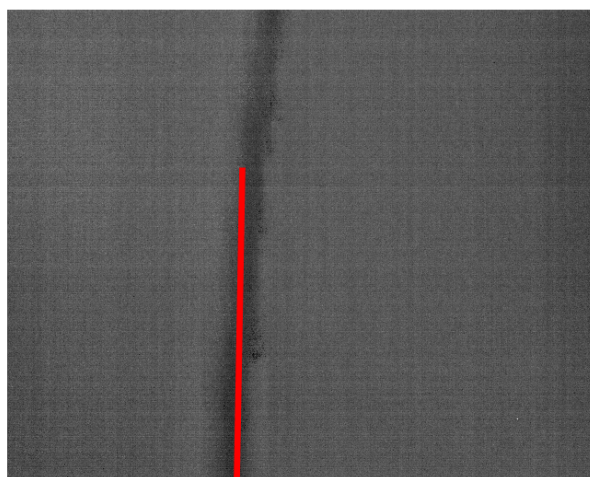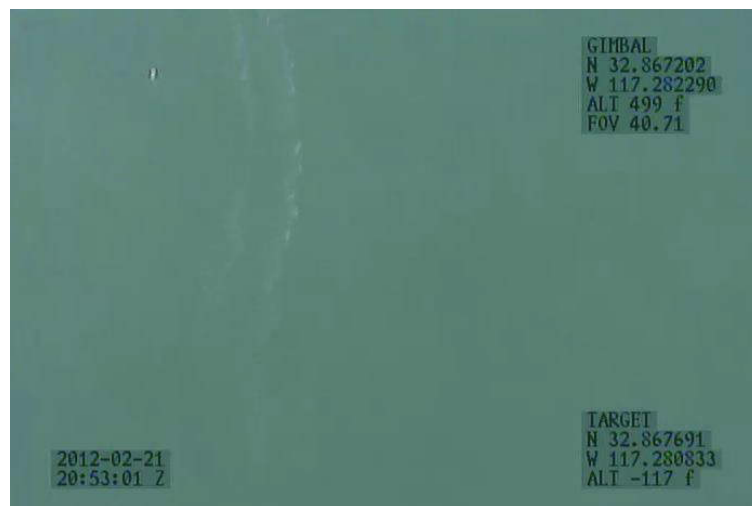Figure C.2: Frame 251 a) optical and b) long wave infrared image.

(a)
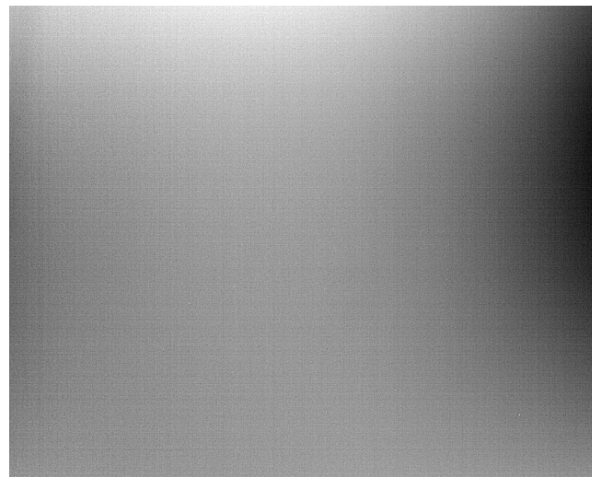
(b)

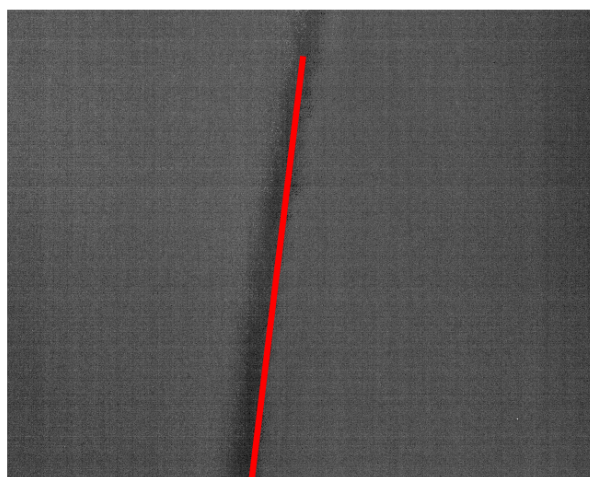Figure C.3: Frame 254 a) optical and b) long wave infrared image.

(a)
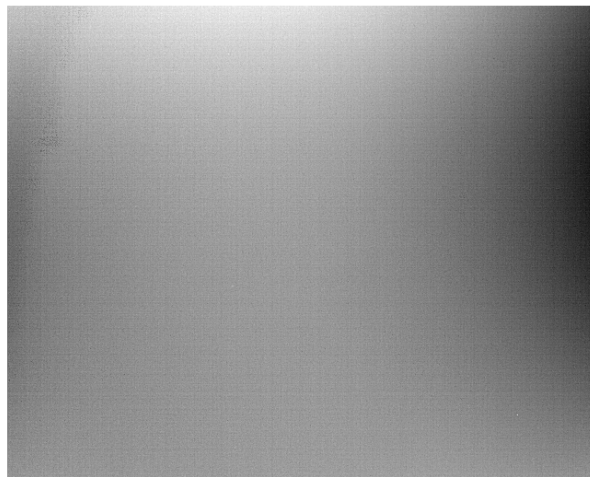
(b)

Figure C.4: Frame 257 a) optical and b) long wave infrared image.
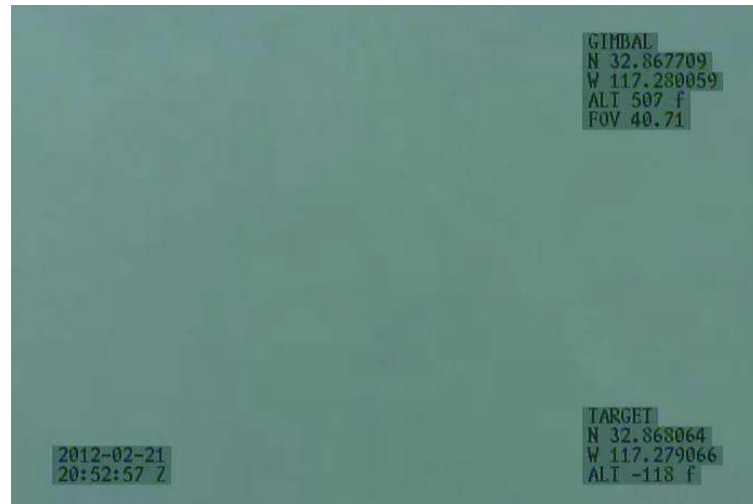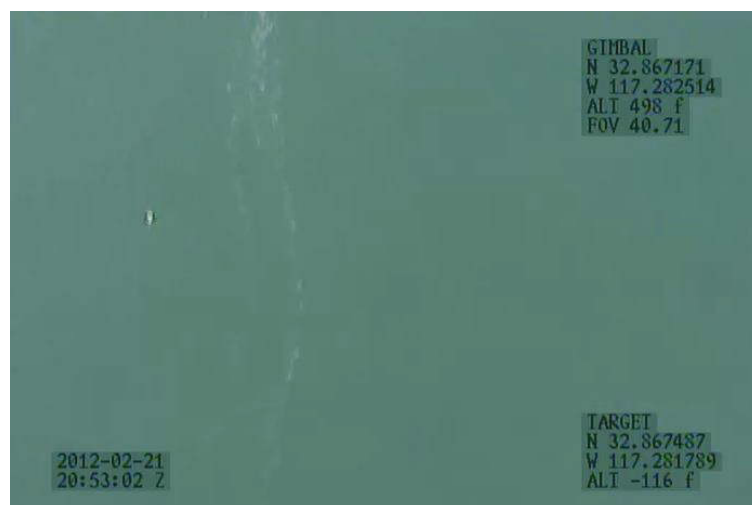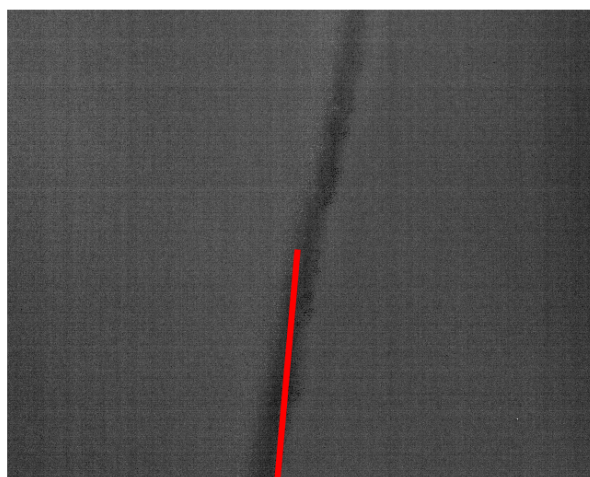
(a)
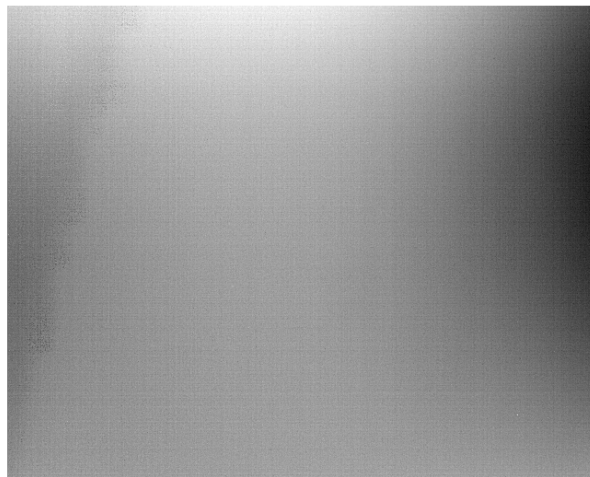
(b)

Figure C.5: Frame 260 a) optical and b) long wave infrared image.

(a)
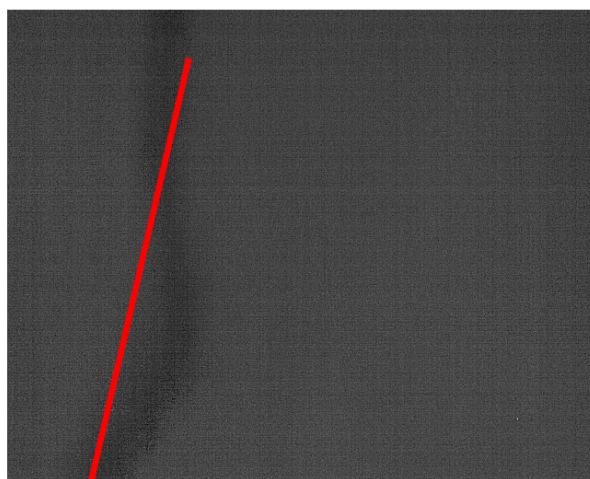
(b)

Figure C.6: Frame 263 a) optical and b) long wave infrared image.
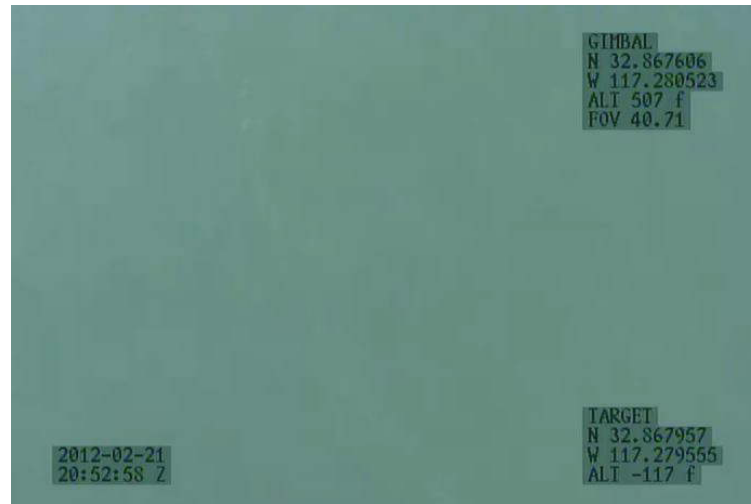
(a)
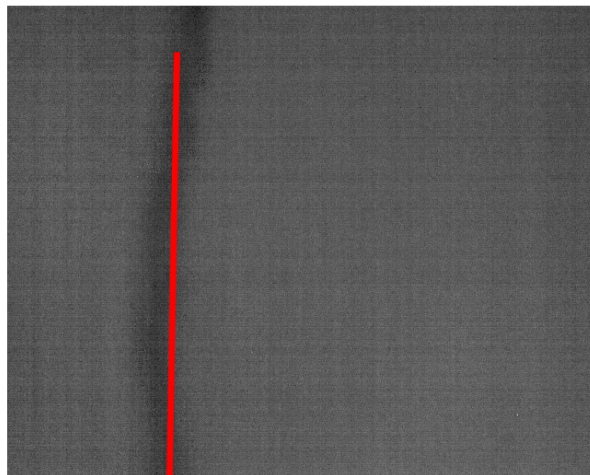
(b)

Figure C.7: Frame 266 a) optical and b) long wave infrared image.

(a)
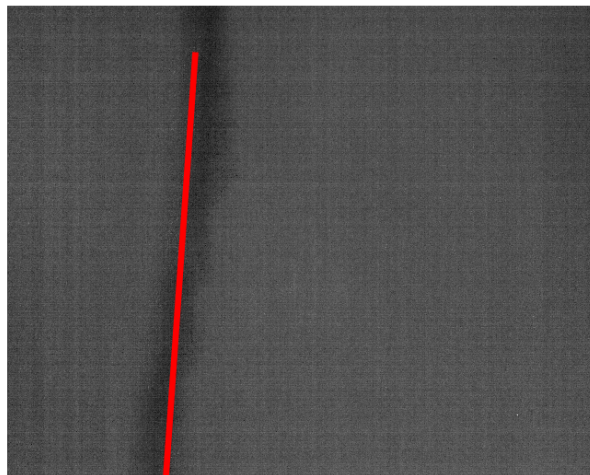
(b)

Figure C.8: Frame 269 a) optical and b) long wave infrared image.

(a)
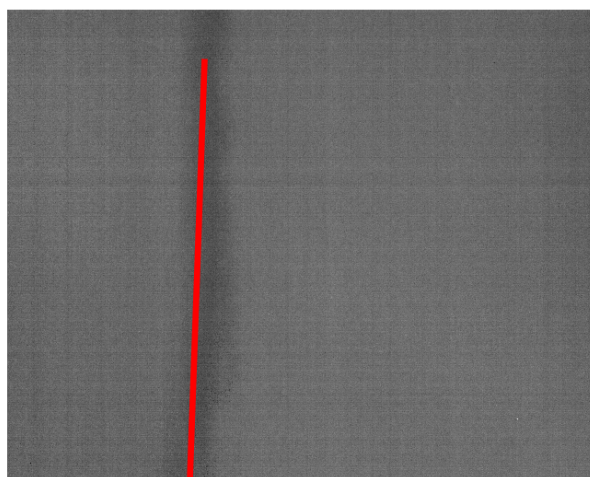
(b)

Figure C.9: Frame 272 a) optical and b) long wave infrared image.
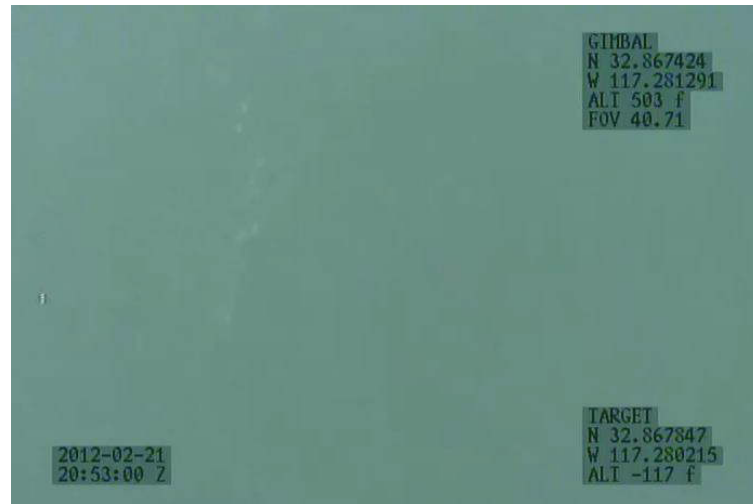
(a)
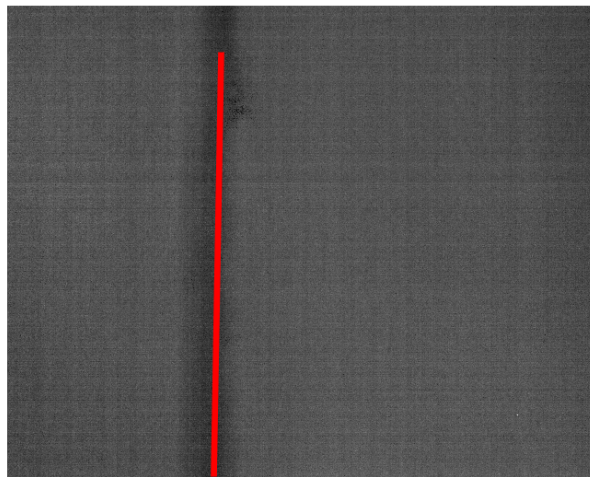
(b)

Figure C.10: Frame 275 a) optical and b) long wave infrared image.

(a)
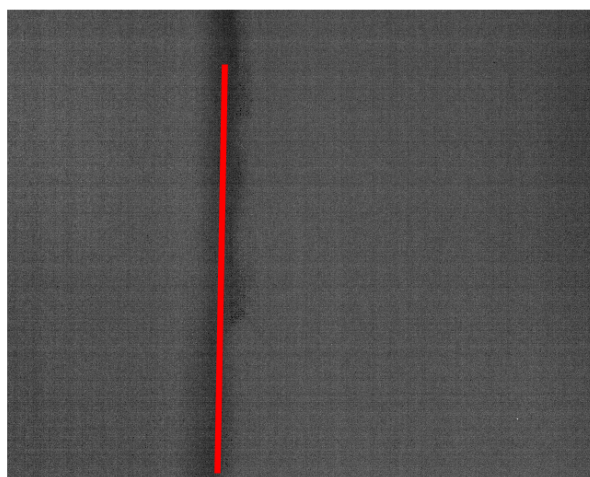
(b)

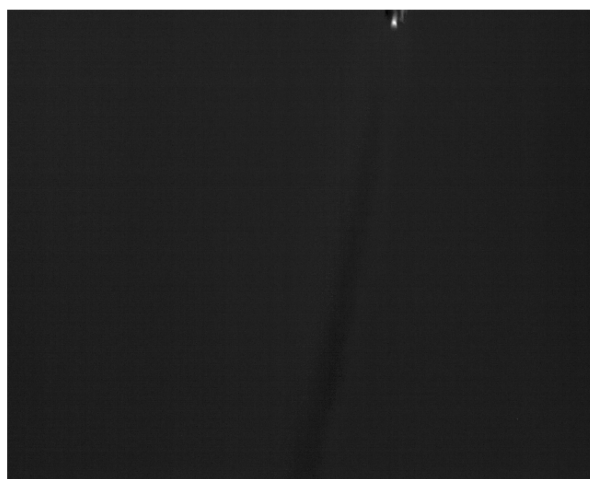Figure C.11: Frame 278 a) optical and b) long wave infrared image.

(a)
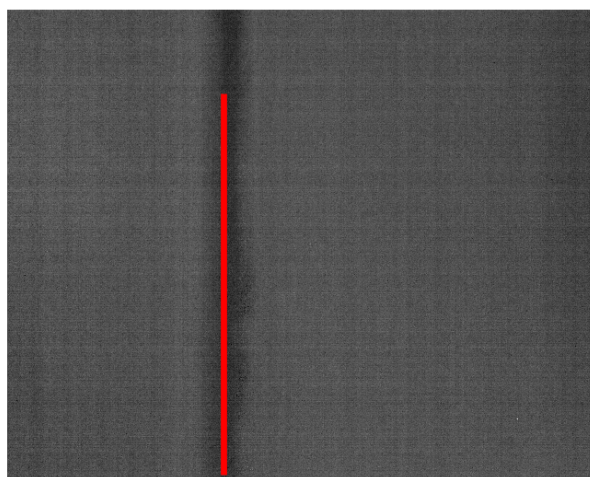
(b)

Figure C.12: Frame 281 a) optical and b) long wave infrared image.
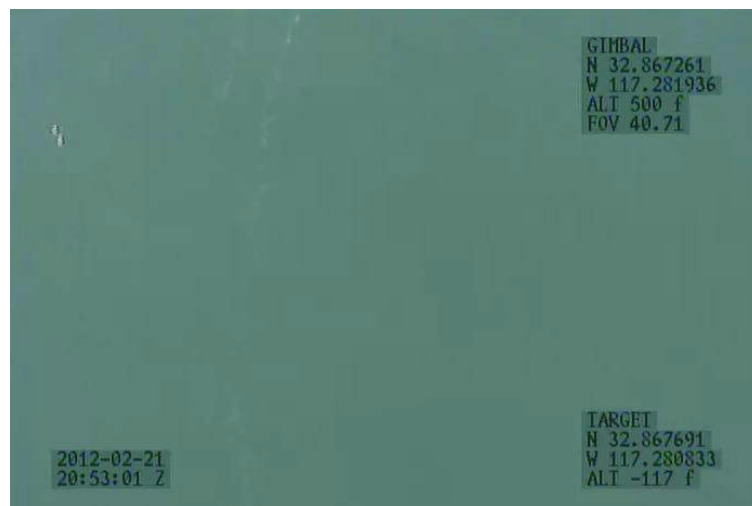
(a)
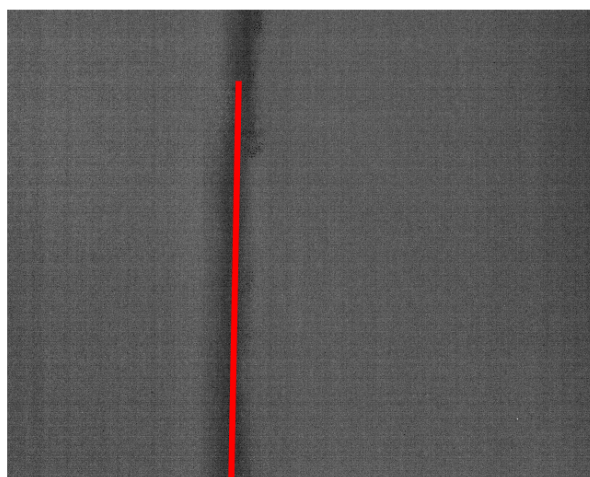
(b)

Figure C.13: Frame 284 a) optical and b) long wave infrared image.

(a)

(b)

Figure C.14: Frame 287 a) optical and b) long wave infrared image.

(a)

(b)

Figure C.15: Frame 290 a) optical and b) long wave infrared image.

(a)

(b)

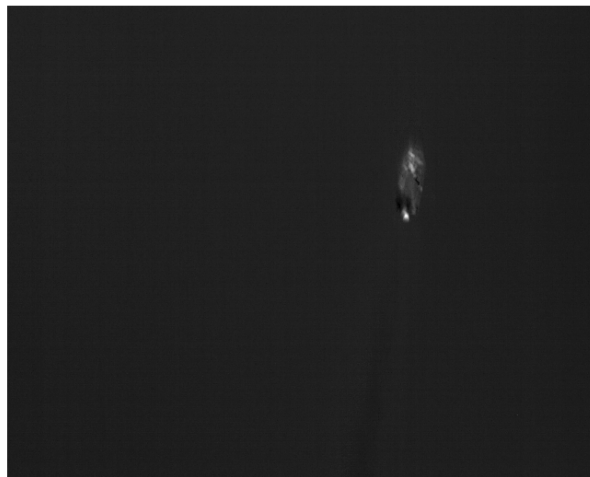Figure C.16: Frame 293 a) optical and b) long wave infrared image.

(a)

(b)

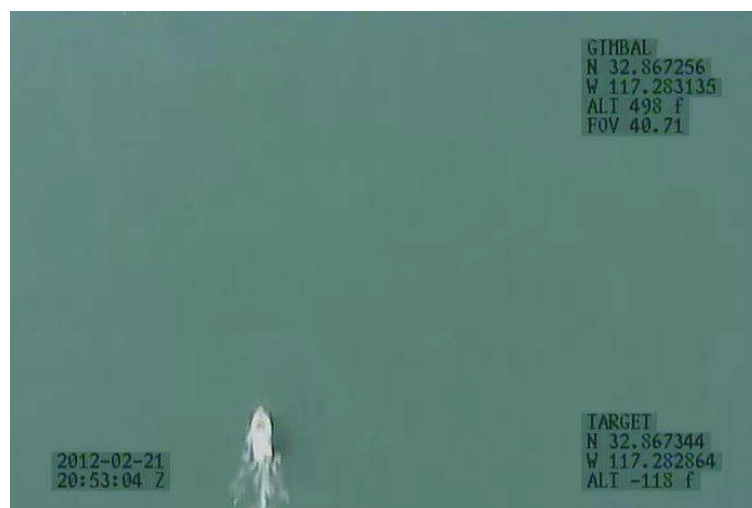Figure C.17: Frame 296 a) optical and b) long wave infrared image.
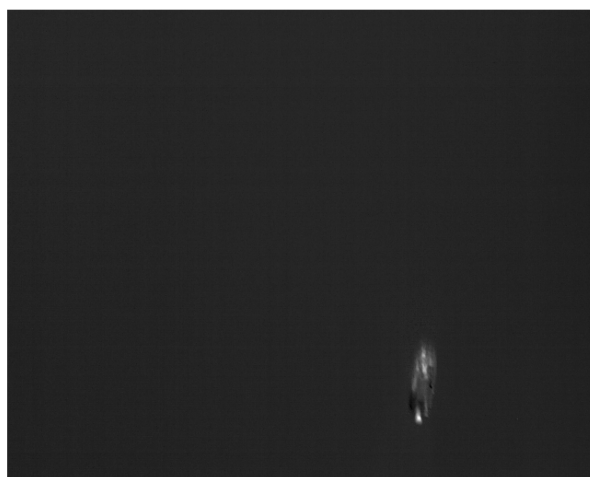
(a)

(b)

Figure C.18: Frame 299 a) optical and b) long wave infrared image.

(a)

(b)

Figure C.19: Frame 302 a) optical and b) long wave infrared image.